UNIVERSITY OF Southampton

Faculty of Engineering, Science and Mathematics
School of Physics and Astronomy

Multiphysics simulations of magnetic nanostructures

by **Matteo Franchin**

Thesis submitted in partial satisfaction
of the requirements for the degree of

DOCTOR OF PHILOSOPHY

Supervisors: Dr. Hans Fangohr, Prof. Peter A.J. de Groot

October 2009

UNIVERSITY OF SOUTHAMPTON

ABSTRACT

FACULTY OF ENGINEERING, SCIENCE AND MATHEMATICS
SCHOOL OF PHYSICS AND ASTRONOMY

Doctor of Philosophy

MULTIPHYSICS SIMULATIONS OF MAGNETIC NANOSTRUCTURES

by Matteo Franchin

In recent years the research on magnetism has seen a new trend emerging, characterised by considerable effort in developing new nanostructures and finding new ways to control and manipulate their magnetisation, such as using spin polarised currents or light pulses. The field of magnetism is thus moving towards the multiphysics direction, since it is increasingly studied in conjunction with other types of physics, such as electric and spin transport, electromagnetic waves generation and absorption, heat generation and diffusion. Understanding these new phenomena is intriguing and may lead to major technological advances. Computer simulations are often invaluable to such research, since they offer a way to predict and understand the physics of magnetic nanostructures and help in the design and optimisation of new devices.

For the preparation of this thesis the *Nmag* multiphysics micromagnetic simulation package has been further developed and improved by the author. The software has also been extended in order to model exchange spring systems. Using *Nmag*, we carried out micromagnetic simulations in order to characterise the magnetisation dynamics in exchange spring systems and derived analytical models to validate and gain further insight into the numerical results. We found that the average magnetisation moves in spiral trajectories near equilibrium and becomes particularly soft (low oscillation frequency and damping, high amplitude) when the applied field is close to a particular value, called the bending field.

We studied spin transport in exchange spring systems and investigated new geometries and setups in order to maximise the interaction between spin polarised current and magnetisation. We found that by engineering a trilayer exchange spring system in the form of a cylindrical nanopillar, it is possible to obtain microwave emission with frequencies of 5-35 GHz for applied current densities between 0.5-2.0 $\times 10^{11}$ A/m^2 and without the need for an externally applied magnetic field. We proposed a one dimensional analytical model and found a formula which relates the emission frequency to the geometrical parameters and the current density.

Contents

List of Figures

Declaration of Authorship

I, Matteo Franchin, declare that the thesis entitled "Multiphysics simulations of magnetic nanostructures" and the work presented in the thesis are both my own, and have been generated by me as the result of my own original research. I confirm that:

- this work was done wholly or mainly while in candidature for a research degree at this University;
- where any part of this thesis has previously been submitted for a degree or any other qualification at this University or any other institution, this has been clearly stated;
- where I have consulted the published work of others, this is always clearly attributed;
- where I have quoted from the work of others, the source is always given. With the exception of such quotations, this thesis is entirely my own work;
- I have acknowledged all main sources of help;
- where the thesis is based on work done by myself jointly with others, I have made clear exactly what was done by others and what I have contributed myself;
- parts of this work have been published in specialised journals:
    - Sec. 5.4 is based on work published as "M. Najafi, B. Kruger, S. Bohlens, M. Franchin, H. Fangohr, A. Vanhaverbeke, R. Allenspach, M. Bolte, U. Merkt, D. Pfannkuche, D. P. D. Moller, and G. Meier. *Proposal for a standard problem for micromagnetic simulations including spin-transfer torque*, J. Appl. Phys. 105, 113914 (2009)"
    - Sec. 6.3 is based on work published as "M. Franchin, J. P. Zimmermann, T. Fischbacher, G. Bordignon, P. A. J. de Groot, and H. Fangohr, *Micromagnetic modelling of the dynamics of exchange springs in multi-layer systems*, IEEE Trans. on Magn. 43, 2887 (2007)]"
    - Ch. 7 is based on work published as "M. Franchin, G. Bordignon, T. Fischbacher, G. Meier, J. P. Zimmermann, P. A. J. de Groot, and H. Fangohr, *Spin-polarized currents in exchange spring systems*, J. Appl. Phys. 103, 07A504 (2008)"

  - Ch. 8 is based on work published as "M. Franchin, T. Fischbacher, G. Bordignon, P. A. J. de Groot, and H. Fangohr, *Current driven dynamics of domain walls constrained in ferromagnetic nanopillars*, Phys. Rev. B 78, 054447 (2008)"

- parts of Sec. 5.4 have been included in the *Nmag* manual which has been published online at `http://nmag.soton.ac.uk`.

Signed: ....

Date: ....

Acknowledgements

I would like to thank my supervisors Dr. Hans Fangohr and Prof. Peter A. J. de Groot, for giving me the opportunity to perform this work and for their support and guidance. Working with them and with the now lecturer Dr. Thomas Fischbacher has been an enjoyable and formative experience. Their enthusiasm and intelligence had a strong influence on my professional development in these years and taught me to be more ambitious in my objectives.

I am grateful to Giuliano Bordignon and Andreas Knittel for being my closest "travel mates" throughout the PhD. This thesis is, in an indirect way, also the result of their work.

I would also like to thank Dr. Guido Meier and Benjamin Krüger for the stimulating discussions and for helping me to make my first steps in the field of spin transport. I am particularly thankful to Massoud Najafi for being always open to work together and discuss the physics and numerical aspects of micromagnetics. It has been a pleasure to work and enjoy the time with him!

I cannot forget the friends of building 25 for their moral support. Dario and Ernesto, who — beside being the inventors of the "Friday pizza meeting" — are invaluable people and friends! And Jörn, Jun, Raúl, Lindsay, Richard, Jürgen, Hani, Matt and my flatmates Luca, Clara and Alejandra for making this city a comfortable place where to live.

I am also grateful to all the financial sources which made this work possible: EPSRC, the School of Physics and Astronomy and the School of Engineering Sciences of the University of Southampton, the IoP and IEEE for support with the travel costs of the several conferences I could attend in these years.

Ringrazio la mia famiglia per l'amore e affetto incondizionato che mi dà e che rende questo mondo un posto caldo e confortevole in cui vivere. E ringrazio te, amore mio, che accompagni ogni mio pensiero, osservi e ti curi d'ogni battito del mio cuore. Voi siete le forze che mi sorreggono e mi permettono di camminare e vivere in questo mondo, senza paura.

Nomenclature

LHS, RHS	Left-Hand-Side, Right-Hand-Side
LLG	shorthand used to refer to the Landau-Lifshitz-Gilbert equation (2.2)
LL	shorthand used to refer to the Landau-Lifshitz equation (2.3)
STT	stands for Spin Transfer Torque, see Ch. 3
DC, AC	Direct Current, Alternating Current
GMR	Giant Magneto-Resistance, see Ch. 3
FE, FD	Finite Element, Finite Difference
FEM	Finite Element Method, a space discretisation method, see Ch. 4
BEM	Boundary Element Method
RK	Runge-Kutta, time-integration schemes, see Sec. 4.2.2
BDF	Backward Differentiation Formula, class of time integration algorithms
α	damping constant in Eq. (2.2) (LLG), for Permalloy $\alpha = 0.01$-0.02
γ	gyromagnetic ratio in Eq. (2.2) (LLG), typically $\gamma = 2.210173 \times 10^5\,\mathrm{m/(As)}$
γ'	gyromagnetic ratio in Eq. (2.3) (LL), the relation $\gamma' = \gamma/(1+\alpha^2)$ holds
$\vec{M}$	the magnetisation, a three dimensional vector field
M_{sat}	the saturation magnetisation, $M_{\mathrm{sat}} = \|\vec{M}\|$
$\hat{M}$	the normalised magnetisation, $\hat{M} = \vec{m}/M_{\mathrm{sat}}$
$\vec{H}$	the effective field, a three dimensional vector field
$\vec{H}_{\mathrm{app}}$	the applied magnetic field, a three dimensional vector field
A	Exchange coupling constant, Eq. (2.11)
C	$C = 2A/(\mu_0 M_{\mathrm{sat}})$
K_1, K_2, K_3	anisotropy constants, see Eqs. (2.9) and (2.10)
μ_0	permeability of free space
μ_{B}	Bohr magneton
e	electron charge (absolute value, it is a positive number)
j_{e}	electric current density
P	spin polarisation, see Eq. (3.12)

τ_{ex}	exchange relaxation time, see Ch. 3
τ_{sf}	spin-flip relaxation time , see Ch. 3
$\xi = \tau_{\mathrm{ex}}/\tau_{\mathrm{sf}}$	degree of non adiabadicity, see Eq. (3.12)
v	$v = P\mu_{\mathrm{B}} j_{\mathrm{e}}/(eM_{\mathrm{sat}}(1+\xi^2))$, parameter used in Eq. (3.12)
$a = 1 + \alpha\xi$	parameter used in Eq. (3.13)
$\overline{a} = \xi - \alpha$	parameter used in Eq. (3.13)

Chapter 1

Introduction

The properties of magnetic materials had an important role in past centuries, allowing the development of the magnetic compass, which led to safe navigation far from land and thus had a tremendous impact on the sea trade as well as on the discoveries of new lands. The role of magnetic materials is probably even more important today, as we are storing most of our knowledge inside magnetic media such as hard disks and magnetic tapes. An hypothetical "magnetic blackout", consisting of all materials losing their magnetic status, would lead to devastating consequences in our modern society, putting the internet and most of the information systems out of order.

Information in hard disk drives is stored by magnetising the grains which cover the surface of the inner disks (see Fig. 1.1) and behave like small magnets, having north and south magnetic poles. The magnetic orientation (south-north pole direction) of these grains is used to encode the information and is preserved when the device is turned off. Since the grains have random positions on the surface of the disks, many grains, arranged in what is called a "bit cell", are required in order to store one single bit of information. Data is written by applying an external magnetic field to change the magnetisation of the grains and is read by probing the field they produce. Both operations are performed by a read-write head which moves very close to the disk surface. As the density of information is the critical parameter for a data storage medium, a staggering technological effort has been made in the last fifty years to reduce the size of the bit cell. The areal density of information (bits per square inch) has indeed increased from 2 kbit/in^2 in 1956 to 3×10^8 kbit/in^2 in 2008 [1, 2].

The size and number of grains used to store one bit has decreased considerably and is now hitting fundamental limits. One of the main problems is data stability. A smaller magnetic grain has less magnetic energy. If the grain is small enough, such energy

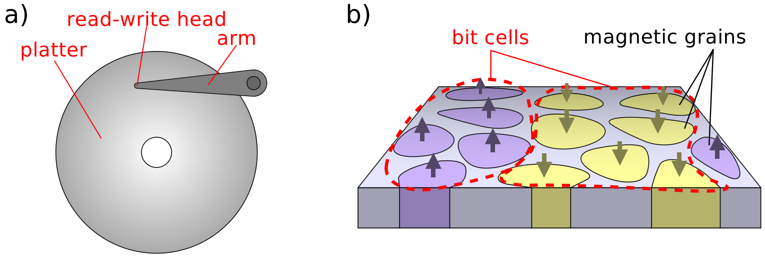

Figure 1.1: a) Sketch of the mechanical structure of an hard disk drive. The platter rapidly rotates around its axis, while the arm moves the read-write head to the position where the data needs to be written or read. b) The composition of the thin polycrystalline magnetic film which covers the platter. The arrow in each grain represent the magnetisation (which is orthogonal to the film plane). Different colors are used to better identify grains with opposite magnetisation.

can be comparable with the thermal energy, meaning that "thermal agitation" can lead to random fluctuations of the magnetisation and thus to random data loss. This problem, often referred as the superparamagnetic limit, poses new challenges for future developments of hard disk technology. Further increases of areal density will be possible only through innovations of a more conceptual nature, such as perpendicular recording (magnetisation perpendicular to the disk surface), patterned media, thermally-assisted recording.

Research is also focusing on radically new applications of magnetism. Spin transfer torque (STT) effects [3], for example, may open the door to the fabrication of nano-sized microwave generators to be used for chip-to-chip or intra-chip wireless communication [4]. These effects may also be exploited in the next generation of MRAM memory chips to obtain a STT driven MRAM, which is believed to be the memory of the future, combining most of the advantages of other types of memory, such as ultra-fast write/read access, low power consumption, non-volatility, high density and potentially low cost of production.

All these exciting new technological advances, including further improvements in hard disks performance, require a clearer understanding of magnetism and how it couples with other phenomena. In a research environment where thermal assisted recording, spin transfer torque switching and microwave emission and absorption are the main concerns, it is extremely important to have flexible and powerful multiphysics simulation tools which can simulate the magnetic dynamics, but can also take into account the other relevant aspects of the physics of the system. The ability to simulate all these effects in nanomagnetic systems is indeed fundamental both to understand the behaviour of the existing nanostructures and to assist in the design of new devices.

With this thesis we contributed to the development of *Nmag*, a new micromagnetic simulation software which offers multiphysics capabilities. We extended and used the software to simulate a class of systems which is of particular relevance to our experimental group in Southampton: exchange spring systems. Exchange spring systems have been studied experimentally in Southampton in recent years and this thesis aims to improve the understanding of their static magnetic properties as well as their characteristic magnetisation dynamics. Motivated by our belief that spin transfer torque effects may be relevant in these systems, we initiated investigations in this field. The objective was to precede the experimental work in Southampton: we needed to understand if and how spin transfer torque effects may be relevant in such systems and to possibly find new technological applications. In order to achieve this objective, we extended our software package *Nmag*, by including spin transfer torque effects. We carried out micromagnetic simulations and analysed the results, getting to analytical models which were useful to both confirm the correctness of the simulations and clarify the physics. The cross-check with analytical calculations is particularly important, considering that, due to the exploratory nature of the thesis, we didn't have experimental data to compare against. The studies we carried out suggest important technological applications of exchange spring systems. We indeed conclude in Ch. 7 and Ch. 8 that, by engineering an exchange spring system in the form of a cylindrical nanopillar, it is theoretically possible to geometrically constrain a domain wall and induce it to stationary precession by the application of a constant direct current (DC). This system may then be used as a nano-sized microwave generator, whose emission frequency can be controlled by tuning the current density flowing through the nanopillar.

Outline of the thesis

Here is a brief outline of this thesis. In chapter 2 we give an introduction to micromagnetics. We write down the equation of motion for the magnetisation dynamics and briefly explain the mathematical terms which are involved. In chapter 3 we discuss spin transport in ferromagnetic conductors. We introduce the giant-magnetoresistance (GMR) effect and then focus on the effects of spin polarised currents on the magnetisation dynamics. We present a detailed derivation of the model which is later used in the thesis to study spin transfer torque effects. In chapter 4 we give an overview of some of the computational methods which we employ in our simulations. The chapter presents the key concepts at the base of the finite element method (FEM), the scheme we use for space discretisation. It also discusses some time-integration algorithms for micromagnetics. In chapter 5 we present *Nmag*, the micromagnetic package developed at the University of Southampton to which we contributed while working on this thesis. We explain the motivations for the creation of the software and show its key features in two example simulations. In chapter 6 we study exchange spring systems. We first analyse the static properties of these systems and then focus on dynamic properties, using both analytical models and computer simulations. We also study the effects on the magnetisation dynamics of an electric current flowing orthogonal to the layers of an exchange spring system. In chapter 7 we continue the study of exchange spring systems with a different geometry and magnetisation setup, showing how this choice enhances the spin transfer torque effects. In chapter 8 we carry out a systematic study of the system introduced in the previous chapter and understand the role of the geometry and of the magnitude of the current density. We also present an analytical model which clarifies the mechanism at the base of the observed effects. In chapter 9 we try to briefly summarise what we have done, stressing the elements of novelty. We try to review this work as a part of a wider research plan and discuss future developments.

Chapter 2

Background

In this chapter we give a quick introduction to micromagnetics, the theory which stands at the base of the computations and results presented in this thesis. The aim of this chapter is to fix the terminology and nomenclature and to list most of the fundamental equations which are used in the next chapters.

2.1 Magnetism in matter

What happens when an external magnetic field $\vec{H}$ is applied to a body? From the classical theory of magnetism we know that a magnetic dipole moment is induced inside the body. This is what happens in the case of diamagnetic or paramagnetic materials and can be described roughly by the formula $\vec{M} = \chi \vec{H}$. χ is the magnetic susceptibility of the considered material and $\vec{M}$ is the "magnetisation" of the body, which is defined as the magnetic dipole moment per unit of volume and is hence zero in the empty space. We will return to its definition in the next section. Here, we are interested in the relationship between the magnetising field $\vec{H}$ and the magnetic field $\vec{B}$ inside the material: $\vec{B} = \mu_0(\vec{H} + \vec{M}) = \mu\vec{H}$, where μ_0 is the permeability of free space and $\mu = \mu_0(1 + \chi)$. There are materials, however, that do not exhibit such a simple linear dependence between the total field $\vec{B}$ inside the body and the applied field $\vec{H}$. Ferromagnetic materials, for example, show to have a memory of the applied field. Their magnetic status $\vec{M}$ depends not only on the current value of $\vec{H}$, but also on the way this field was applied in the past. In this section we briefly outline the physics which is the source of such a rich phenomenology. We do not enter into the details of the physical theory, but rather try to give an intuitive and quick picture of what is happening at the microscopic level.

The most important question to start with is the following: why does a body react to an applied magnetic field? First of all we need to say that electrons are the main source of magnetism inside the body. They give two kinds of contribution. The first one can be understood approximatively with intuitive classical reasonings. The electrons bounded to the atomic nuclei react to an applied magnetic field following the Lenz's Law: the orbitals deform and create a magnetic dipole moment with direction opposite to the applied field ($\chi < 0$), thus reducing $\vec{B}$ inside the body. We stress that this is not an accurate description of the phenomena, which would need to be addressed with a quantum mechanical formulation [5, 6], but it gives nevertheless a rough idea of what is going on. This behaviour is referred to as diamagnetism, a small effect which is always present in matter.

The second kind of contribution is connected with a fundamental property of the electron as an elementary particle: the electron behaves like a point-like magnetic dipole with a well defined intrinsic angular momentum (spin) and intrinsic magnetic moment. The total magnetic moment of the electrons, which receives contribution from the intrinsic and the orbital magnetic moments, tends to align to the applied magnetic field,[1] thus increasing the field $\vec{B}$ inside the body ($\chi > 0$). This effect, however, depends crucially on the way the electrons fill the atomic orbitals. Indeed, the atoms of a non-magnetic material have zero net magnetic moment. This is not the case with paramagnetic and ferromagnetic materials, whose net magnetisation is locally non-zero. Consequently, the atoms inside a given small volume d^3r of these materials behave like magnetic dipoles, $\vec{M}\mathrm{d}^3r$ being the net magnetic dipole moment inside the small volume d^3r.

For paramagnets, $\vec{M}$ is linearly proportional to $\vec{H}$. This means that the alignment of the magnetic dipoles inside d^3r increases linearly with the applied field. This means also that when the applied field is removed, the alignment is lost and $\vec{M}$ becomes zero everywhere. This effect is connected with thermal agitation. In ferromagnets the situation is slightly more complicated, as we will see better in the next sections. Here we say only that in ferromagnets the thermal agitation competes with another effect: the moments of neighbouring atoms interact in such a way that they tend to stay aligned with each other. This interaction is called "exchange coupling" and is a purely quantum mechanical effect, which is the main cause of the "memory" of ferromagnetic materials. At this point it should be easy to understand why the ferromagnetic properties of

---

[1] This is the typical behaviour of a dipole immersed in an external field: the dipole moment aligns with the applied field.

materials depend strongly on the temperature. When a ferromagnet is heated above a particular temperature T_{C}, the Curie temperature, the thermal energy is sufficient to change the alignments of neighbouring magnetic moments and the material starts to exhibit paramagnetic behaviour.

2.2 Introduction to micromagnetics

In the previous section we explained that the magnetism of a ferromagnetic material comes mainly from the magnetic moment of the electrons of its constituent atoms. From the point of view of magnetic properties such a material could be modelled as a huge collection of magnetic dipoles with positions fixed in space. This is actually the starting point of the theory of micromagnetics. To go further one needs to understand how these dipoles interact and what kind of dynamics is connected with such interactions. These two key points in the theory are faced by the Brown's equations and the Landau-Lifshitz-Gilbert equation, respectively. These formulas rely on a common formalism: a continuous vector field $\vec{M}(\vec{r}, t)$ — the magnetisation — is used to represent the magnetic status of the system and is defined requiring $\vec{M}(\vec{r},\, t)\mathrm{d}^3r$ to be the net magnetic dipole moment inside the small volume d^3r. This is an approximation which neglects the discrete nature of the system and is based on an important assumption: the direction of the magnetic moments in the ferromagnet should change smoothly with position. This is true only when the temperature of the body is lower than the Curie temperature, as explained in the previous section. We note that, since the material is supposed to be homogeneous, the norm of the magnetisation is constant in space and time: $\|\vec{M}(\vec{r}, t)\| = M_{\mathrm{sat}}$, M_{sat} is the magnetic dipole moment per crystallographic unit cell and is called saturation magnetisation.

Before introducing the Brown's and Landau-Lifshitz-Gilbert equations we first prepare the ground by making some observations. Let's consider a bunch of atoms inside the volume d^3r of the ferromagnet. The magnetic dipole $\vec{\mu} = \vec{M}\,\mathrm{d}^3r$ of the bunch of atoms experiences an effective field $\vec{H}$ which is given by the superposition of the applied field and the field created by all the other atoms in the body.[2] Its energy is calculated easily in the classical theory of magnetism as $U_{\mathrm{dip}}(\vec{\mu}) = -\mu_0\,\vec{\mu}\cdot\vec{H}$ and is minimised when $\vec{\mu}$ is parallel to $\vec{H}$. Since the total energy of the system is the sum of the energy of each of its constituent dipoles, we expect that at equilibrium all the atoms have magnetic moment parallel to the experienced effective field. This means that $\vec{M}(\vec{r}, t)$ is

---

[2] Here we assume that the net moment $\vec{\mu}$ of the bunch of atoms can be treated as a classical magnetic dipole. The moments inside d^3r are almost parallel and hence can be described as a single moment.

parallel everywhere to $\vec{H}(\vec{r}, t)$ at equilibrium. The equilibrium configuration, however, is reached in a non-straightforward way: the effective field changes when the magnetisation moves towards it! To understand how the moment $\vec{\mu}$ dynamically depends on the effective field, we can use classical mechanics: the angular momentum $\vec{L} = \vec{r} \times \vec{p}$ of the bunch of atoms is related to the torque $\vec{\tau} = \vec{r} \times \vec{F}$ by the relation $\vec{\tau} = \mathrm{d}\vec{L}/\mathrm{d}t$ ($\vec{r}$, $\vec{p}$ and $\vec{F}$ are the position, the linear momentum and the force respectively). The torque can be calculated easily for a magnetic dipole [5] as $\vec{\tau} = \mu_0\, \vec{\mu} \times \vec{H}$. The angular momentum $\vec{L}$ is related to the magnetic dipole moment $\vec{\mu}$ by the relation $\vec{L} = -\vec{\mu}/\gamma_0$, where γ_0 is a constant called gyromagnetic ratio. This relation follows by the antiparallelism of the spin and the magnetic moment of electrons [5] (which can be derived as a consequence of the Dirac equation or more accurately by quantum electrodynamics). Putting together these formulas one obtains:

$$\frac{\mathrm{d}\vec{\mu}}{\mathrm{d}t} = -\gamma_0\mu_0\, \vec{\mu} \times \vec{H}.$$

We define $\gamma = \gamma_0\mu_0$ and express the same equation referred to the magnetisation:

$$\partial_t \vec{M}(\vec{r}, t) = -\gamma\, \vec{M}(\vec{r}, t) \times \vec{H}(\vec{r}, t). \tag{2.1}$$

This equation describes a very simple dynamics: the magnetisation $\vec{M}$ in $\vec{r}$ tries to precess around the effective field evaluated at the same position.

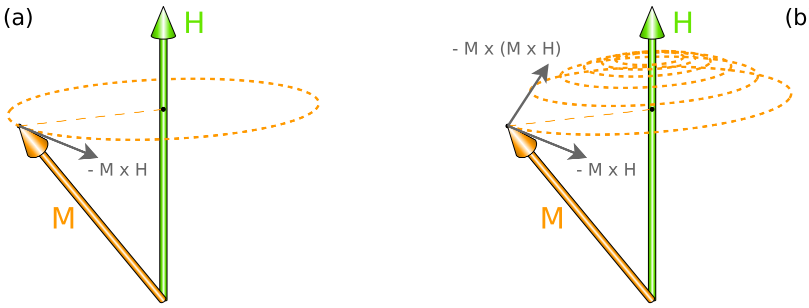

Figure 2.1: (a) The dynamics described by Eq. (2.1) when the effective field $\vec{H}$ is constant in time. The magnetisation $\vec{M}$ precesses around $\vec{H}$ without damping. (b) The dynamics with the inclusion of the damping term, Eq. (2.2).

Obviously $\vec{H}$ depends on $\vec{M}$ and the general dynamics is more complicated than the one shown in figure 2.1.

2.2.1 The Landau-Lifshitz-Gilbert equation

Eq. (2.1) does not take into account any kind of dissipation and predicts a periodic rotational motion for the magnetisation in a uniform constant effective field. The Landau-Lifshitz-Gilbert equation is a variant of such an equation with an additional term to take into account the damping effects,

$$\partial_t \vec{M} = -\gamma \vec{M} \times \vec{H} + \frac{\alpha}{M_{\text{sat}}} \vec{M} \times \partial_t \vec{M}. \tag{2.2}$$

We omitted here the time and spatial dependencies of the vectors: $\vec{M} = \vec{M}(\vec{r}, t)$ and $\vec{H} = \vec{H}(\vec{r}, t)$. α is a dimensionless damping coefficient and causes the magnetisation to get near and nearer to the effective applied field. An equivalent form of this formula is the Landau-Lifshitz equation:

$$\partial_t \vec{M} = -\gamma' \left[\vec{M} \times \vec{H} + \frac{\alpha}{M_{\text{sat}}} \vec{M} \times \left(\vec{M} \times \vec{H} \right) \right], \tag{2.3}$$

where $\gamma' = \gamma/(1+\alpha^2)$. The equivalence can be demonstrated easily by substituting Eq. (2.2) into itself and proceding with a few elementary vector manipulations. Even if the Gilbert form (2.2) is often found in the literature, in this thesis we consider mostly the Landau-Lifshitz form (referred in what follows as LL equation), because it is more suitable to be treated computationally, as the right hand side does not contain $\partial_t \vec{M}$.

We note that these equations lead to a preservation law for the norm of $\vec{M}$:

$$\partial_t M^2 = 2\vec{M} \cdot \partial_t \vec{M} = 0, \tag{2.4}$$

since we know from the right hand side of (2.2, 2.3) that $\partial_t \vec{M}$ is orthogonal to $\vec{M}$. We also note that when $\alpha = 0$ we obtain the undamped Eq. (2.1).

We conclude this section with other two observations. Firstly, we should say that these equations are somewhat phenomenological. The damping factor α summarises the not better specified damping effects and is usually obtained from experimental results. Typical values used for the parameters γ and α are $\gamma = 2.211 \times 10^5\,\text{m/(As)}$ and $\alpha = 0.01$-0.02 (permalloy). Secondly, these equations are not sufficient to fully describe the time-evolution of the magnetisation for any interesting physical system. We still need to specify how the moments interacts and the effective field they produce. This is not a minor detail. Indeed, the effective field depends on the magnetisation in such a complex way that it is usually not possible to find an analytical solution of the Landau-Lifshitz equation.

2.2.2 The energy contributions

As remarked at the end of the previous section, the Landau-Lifshitz equation alone is not sufficient to calculate the time evolution of the magnetisation. What is missing is a characterisation of how the magnetic moments interact with each other and with the applied magnetic field. In this section we introduce the energy terms which are commonly used in micromagnetics. In the next section, we will write down the Brown's equations and give an explicit expression for the effective field as a function of the magnetisation. This is the missing piece required in order to compute the time evolution of the magnetisation.

We write the energy of the system as a sum of several terms:

$$U = U_{\text{exch}} + U_{\text{Zeeman}} + U_{\text{demag}} + U_{\text{anis}}, \tag{2.5}$$

where:

- $U_{\text{Zeeman}} = -\mu_0 \int \vec{M} \cdot \vec{H}_{\text{app}} \, \mathrm{d}^3 r$ is the energy due to the interaction with the external applied field $\vec{H}_{\text{app}}$, which "tries" to align $\vec{M}$ with it;

- $U_{\text{exch}} = A \int (\nabla \vec{m})^2 \mathrm{d}^3 r$ is the exchange energy, the interaction between the wavefunctions of the electrons of neighbouring atoms, which tries to align their magnetic moments. $\vec{m} = \vec{M}/M_{\text{sat}}$ is the unit vector associated with $\vec{M}$ and $(\nabla \vec{m})^2 = (\nabla m_x)^2 + (\nabla m_y)^2 + (\nabla m_z)^2$. A is the exchange coupling constant. This is a genuine quantum mechanical effect which comes from a term in the Hamiltonian with the Heisenberg form $H = -I_{12} \, \vec{S}_1 \cdot \vec{S}_2$, where $\vec{S}_{1,2}$ are the spin of two neighbouring atoms and I_{12} is the exchange integral [6];

- $U_{\text{demag}} = -\frac{\mu_0}{2} \int \vec{M} \cdot \vec{H}_{\text{d}} \, \mathrm{d}^3 r$ is the demagnetising energy, which comes from the long range magnetostatic interaction between the moments of the entire ferromagnetic body. $\vec{H}_{\text{d}}$ is the magnetic field created by all the moments in the body and is obtained solving a Laplace equation, as we will see in a moment;

- U_{anis} is the anisotropy energy, which models the preference for the magnetisation to align along certain well defined directions with respect to the crystal lattice of the material. This term is usually a suitable truncated expansion in powers of the direction cosines of $\vec{M} = M_{\text{sat}} \vec{m}$ relative to the crystallographic axes $\vec{a}_i$ (the direction cosines of $\vec{M}$ are defined as $m_i = \vec{m} \cdot \vec{a}_i$). The coefficients of the expansion can be fitted against the experimental data;

These are the most common contributions to the energy. In some particular situations one may consider adding other more specific terms, as we will see in Ch. 6 for the case of exchange spring systems. Note that micromagnetics is a zero-temperature theory, in the sense that effects such as thermal fluctuations are not taken into account. Temperatures greater than zero should be simulated by selecting values for the parameters in Eq. (2.5) which are appropriate (as much as possible) for the considered temperature.

The last two terms in Eq. (2.5) require some more explanation. The demagnetising energy corresponds to the dipole-dipole interaction in the discrete system. Here, however, we are dealing with a continuous system, so we need to calculate this contribution to the energy in another way. This can be done considering the following two Maxwell's equations:

$$\nabla \cdot \vec{B} = 0, \tag{2.6}$$

$$\nabla \times \vec{H}_{\mathrm{d}} = 0. \tag{2.7}$$

To obtain Eq. (2.7) we assume that there are no free currents travelling in the body and that the electric displacement field $\vec{D}$ does not change in time. Eq. (2.7) tells us that $\vec{H}_{\mathrm{d}}$ can be written as $\vec{H}_{\mathrm{d}} = -\nabla\phi$ for some scalar field ϕ. Since $\vec{B} = \mu_0(\vec{H}_{\mathrm{d}} + \vec{M})$ (where $\vec{M}$ should be considered to be zero outside the ferromagnet), the other equation can be rewritten first as $\nabla \cdot \vec{H}_{\mathrm{d}} = -\nabla \cdot \vec{M}$ and then in terms of the potential ϕ as:

$$\nabla^2\phi = -\rho_{\mathrm{m}}, \tag{2.8}$$

where $\rho_{\mathrm{m}} = -\nabla \cdot \vec{M}$ inside the ferromagnet and $\rho_{\mathrm{m}} = 0$ outside it. The demagnetising field can be obtained solving this Poisson equation. The formal parallelism with electrostatics is perfect: Eq. (2.8) can be obtained from the electrostatic Poisson equation making the substitutions $\rho_{\mathrm{m}} \to \rho_{\mathrm{e}}$ (ρ_{e} is the electric charge) and $1/\epsilon_0 \to 1$. ρ_{m} could be formally referred as a "magnetic charge". We stress, however, that this nomenclature comes only from this formal analogy with electrostatics. To find a solution to (2.8), particular care is needed to treat correctly the surfaces of the ferromagnet, where the norm of the magnetisation jumps suddenly from M_{sat} to zero. This jump gives rise to a well defined surface magnetic charge $\sigma_{\mathrm{m}} = \vec{M} \cdot \vec{n}$, where $\vec{n}$ is the normal to the surface and points outward. This result can be easily deduced using the divergence theorem on a small thin volume crossing the surface (see Fig. 2.2). At this point the solution

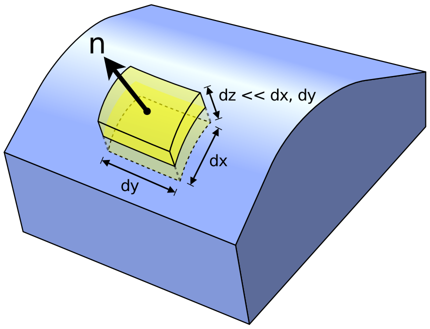

Figure 2.2: The flux of $\vec{M}$ through the surface of the small thin volume $\mathrm{d}^3r = \mathrm{d}x\,\mathrm{d}y\,\mathrm{d}z$ gets a first order contribution $(\vec{M}\cdot(-\vec{n})\,\mathrm{d}x\mathrm{d}y)$ only from the inner surface, since outside the ferromagnet $\vec{M}$ is zero. We assume $\mathrm{d}z \ll \mathrm{d}x, \mathrm{d}y$, so that the lateral surfaces give a negligible contribution to the flux. We know, however, that the flux can be expressed also as $\nabla\cdot\vec{M}\,\mathrm{d}^3r = -\rho_\mathrm{m}\,\mathrm{d}^3r = -\mathrm{d}Q_\mathrm{m}$, where $\mathrm{d}Q_\mathrm{m}$ is the "magnetic charge" contained in the small volume. Therefore $\mathrm{d}Q_\mathrm{m} = \vec{M}\cdot\vec{n}\,\mathrm{d}x\mathrm{d}y = \sigma_\mathrm{m}\,\mathrm{d}S$, where $\mathrm{d}S = \mathrm{d}x\mathrm{d}y$ and $\sigma_\mathrm{m} = \vec{M}\cdot\vec{n}$ is the "surface magnetic charge" density.

should not be particularly surprising:[3]

$$\phi(\vec{r}) = \frac{1}{4\pi}\left(\int \frac{\rho_\mathrm{m}(\vec{r}')\,\mathrm{d}V}{\|\vec{r}-\vec{r}'\|} + \int \frac{\sigma_\mathrm{m}(\vec{r}')\,\mathrm{d}S}{\|\vec{r}-\vec{r}'\|}\right),$$

where the first integral extends over the volume of the ferromagnet, while the second one extends over its surface.

We finally need to provide an expression for the anisotropy energy, the last term in Eq. (2.5). This contribution is quite simple, since it can be taken into account by adding, for every magnetic dipole in the system, an additional energy which depends exclusively on its direction. Consequently the general form of the anisotropy energy is:

$$U_\mathrm{anis} = \int \varepsilon_\mathrm{anis}(\vec{m}(\vec{r}))\mathrm{d}^3r,$$

where $\varepsilon_\mathrm{anis}$ has not a functional dependence on $\vec{m}$, but is simply a function which maps a vector to a scalar. Therefore it can be easily approximated with a suitable expansion. As we said at the beginning of the section, this is done using the direction cosines of $\vec{M}$ with respect to the axes of the crystal lattice $\vec{a}_{1,2,3}$, which are three scalars defined as $m_i = \vec{m}\cdot\vec{a}_i$. In many crystals, however, the anisotropy is uniaxial, meaning that the anisotropy energy depends only on the angle θ_u between the magnetisation and a given fixed axis $\vec{u}$ (therefore it is invariant for rotations of $\vec{M}$ around that axis). Taking

---

[3] Here we use $\mathrm{d}V = \mathrm{d}^3r'$, which breaks the coherence of our notations, but makes the formula look better.

the Fourier expansion of $\varepsilon_{\rm anis}(\theta_{\rm u})$ and considering that $\varepsilon_{\rm anis}(\theta_{\rm u}) = \varepsilon_{\rm anis}(-\theta_{\rm u})$ only the cosine powers remain:

$$\varepsilon_{\rm anis}(\theta_{\rm u}) \approx -K_1 \cos^2\theta_{\rm u} - K_2 \cos^4\theta_{\rm u}. \tag{2.9}$$

The Fourier series is kept up to the fifth power. This is usually enough to model the uniaxial anisotropy in a proper way. The minus signs are conventional and affect only the definition of K_1 and K_2.

The uniaxial anisotropy is typical of crystals with HCP (hexagonal close-packed) lattices (cobalt for example). Other materials (iron for example) show a different dependence on the direction of the magnetisation:

$$\begin{aligned}\varepsilon_{\rm anis}(m_1,\, m_2,\, m_3) \;\approx\;& K_1(m_1^2m_2^2 + m_2^2m_3^2 + m_3^2m_1^2) + K_2(m_1^2m_2^2m_3^2)\\ &+K_3(m_1^4m_2^4 + m_2^4m_3^4 + m_3^4m_1^4).\end{aligned} \tag{2.10}$$

This is the — so called — cubic anisotropy and depends on all the three direction cosines m_1, m_2 and m_3.

2.2.3 The effective field

We have seen that the damping term in the Landau-Lifshitz equation reduces the angle between the magnetisation and the effective field. This dynamics ends when the alignment is reached, namely when the torque $\vec{M}_0 \times \vec{H}$ vanishes. The same process can be seen from another point of view: the system "potential" energy, given by Eq. (2.5), is "eaten" by the damping processes, until the magnetisation is parallel to the effective field and equilibrium is reached. This configuration of $\vec{M}$ minimises hence the energy $U[\vec{M}]$. This means that we have two ways to express the equilibrium condition: the vanishing of the torque and the minimisation of the energy. Since an expression for the energy was given in Eq. (2.5) we can now use variational approaches to minimise U. However, the minimisation must be carried out respecting the constraint of constant norm for the magnetisation, $\vec{m}^2 = 1$. Such a procedure leads to the — so called — Brown's equations [6]:

$$\vec{M}_0 \times \left(\frac{2A}{\mu_0 M_{\rm sat}}\nabla^2\vec{m} + \vec{H}_{\rm app} + \vec{H}_{\rm d} - \frac{1}{\mu_0 M_{\rm sat}}\nabla_{\vec{m}}\,\varepsilon_{\rm anis}\right) = 0.$$

This condition is equivalent to the one of vanishing torque when:

$$\vec{H} = \frac{2A}{\mu_0 M_{\rm sat}}\nabla^2\vec{m} + \vec{H}_{\rm app} + \vec{H}_{\rm d} - \frac{1}{\mu_0 M_{\rm sat}}\nabla_{\vec{m}}\,\varepsilon_{\rm anis}. \tag{2.11}$$

This expression for the effective field, together with the Landau-Lifshitz equation (2.2) is enough to calculate the time evolution of the magnetisation. Each term in Eq. (2.11) corresponds to one term in Eq. 2.5. The first one (called the exchange field, $\vec{H}_{\mathrm{exch}}$) comes from the exchange energy U_{exch} and tries to align neighbouring magnetic moments. The second term (the applied field) comes from the Zeeman energy U_{Zeeman}, the interaction energy with the external applied field. The third one (the demagnetising field) comes from the magnetostatic energy U_{demag} of the ferromagnetic body. The fourth one comes from the anisotropy energy U_{anis}. This last term — which we call $\vec{H}_{\mathrm{anis}}$ — depends on the kind of anisotropy. For uniaxial anisotropy, $\varepsilon_{\mathrm{anis}}(\vec{m}) = f(\vec{m}\cdot\vec{u})$, where $f(x) = -K_1 x^2 - K_2 x^4$, therefore: $\nabla_{\vec{m}}\, \varepsilon_{\mathrm{anis}}(\vec{m}) = \nabla_{\vec{m}}\, f(\vec{m}\cdot\vec{u}) = f'(\vec{m}\cdot\vec{u})\,\vec{u}$, where the derivative of f is $f'(x) = -2K_1 x - 4K_2 x^3$. We conclude that, for the uniaxial case:

$$\vec{H}_{\mathrm{anis}} = \frac{1}{\mu_0 M_{\mathrm{sat}}} \left(2K_1\, \vec{m}\cdot\vec{u} + 4K_2\, (\vec{m}\cdot\vec{u})^3\right)\, \vec{u}.$$

A very similar procedure can be used to calculate the field corresponding to the cubic anisotropy. Indeed, for the cubic anisotropy we have $\nabla_{\vec{m}}\, \varepsilon_{\mathrm{anis}}(m_1,\, m_2,\, m_3) = \sum_{i=1}^{3} (\partial\varepsilon_{\mathrm{anis}}/\partial m_i)\, \nabla_{\vec{m}} m_i$, where $m_i = \vec{m}\cdot\vec{a}_i$. Consequently, $\nabla_{\vec{m}} m_i = \vec{a}_i$ and:

$$\vec{H}_{\mathrm{anis}} = -\frac{1}{\mu_0 M_{\mathrm{sat}}} \sum_{i=1}^{3} \vec{a}_i\, \frac{\partial\varepsilon_{\mathrm{anis}}}{\partial m_i},$$

and,

$$\frac{\partial\varepsilon_{\mathrm{anis}}}{\partial m_1} = 2K_1 m_1 (m_2^2 + m_3^2) + 2K_2 m_1 m_2^2 m_3^2 + 4K_3 m_1^3 (m_2^4 + m_3^4).$$

$\partial\varepsilon_{\mathrm{anis}}/\partial m_2$ and $\partial\varepsilon_{\mathrm{anis}}/\partial m_3$ can be obtained from the same equation by cyclic permutation of the indices.

Chapter 3

Spin-transport in ferromagnetic conductors

Beside being an electric charge carrier, the electron is also a spin carrier. Consequently electric currents can also be — quite in general — spin currents. Then, a question that naturally arises is: does the spin of the conduction electrons interact with the magnetisation in a ferromagnetic conductor? And, can this interaction be exploited for technological applications? These are the central questions in spintronics, a research field which has become increasingly active in the last two decades, first with the discovery of the giant magnetoresistance (GMR) in 1988 [7, 8], later with the prediction of spin-transfer torque effects in 1995 [3, 9], which were confirmed experimentally two years later [10].

In the following chapters of this thesis we present computational studies of the spin transfer effects which occur in exchange spring systems and in nanopillars. The purpose of this chapter is to introduce the reader quickly to the fundamental concepts behind the physics of spin transport and present the model which we employ in our numerical studies.

3.1 The giant magnetoresistance

The GMR was discovered independently in 1988 by the group of Albert Fert [7] and the group of Peter Grünberg [8] and led, in the following years, to major advances in the technology of magnetic sensors and data storage. The impact of such a discovery was recently recognised with the Nobel Prize in Physics 2007 jointly awarded to Albert Fert and Peter Grünberg.

While other types of magnetoresistance (MR) were known before the discovery of Fert and Grünberg (such as the anisotropic magnetoresistance, AMR), the GMR was immediately recognised as a significantly greater effect in terms of resistance variations. In the original paper the group led by Fert [7] reported resistance variations around $50\,\%$, while studying $(\mathrm{Fe/Cr})_n$ multilayers at low temperature ($4.2\,K$), while Grünberg [8] group reported variations around $10\,\%$ in a trilayer Fe/Cr/Fe at room temperature. Fert already referred to the effect as *giant* magnetoresistance: indeed, AMR effects are typically much smaller, of the order of few percent [11].

We now explain briefly what GMR is and give a quick intuitive picture of the underlying physics. We first discuss briefly the resistance properties of a ferromagnetic conductor.

3.1.1 Resistance in a ferromagnetic conductor

In a small volume $\mathcal{V}$ of a ferromagnetic conductor the total amount of magnetic moment is $M_{\mathrm{sat}}\,\mathcal{V}$, meaning that the intrinsic magnetic moment of the electrons inside $\mathcal{V}$ is oriented preferably along the magnetisation direction, rather that in the opposite one. In other words we have a moment/spin imbalance inside $\mathcal{V}$, which is intimately related to the non vanishing saturation magnetisation M_{sat} and is reflected to the characteristic band structure of the material (see Fig. 3.1). This spin imbalance is likely to affect also the itinerant electrons, which we ideally split into two components, one

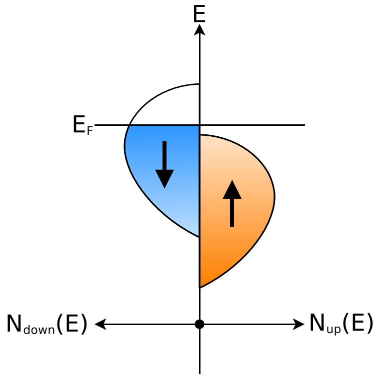

Figure 3.1: A schematic simplified representation of the band structure of a ferromagnetic conductor. The “spin up” band is completely below the Fermi energy E_F, so that only the “spin down” carriers are available for conduction. Such a material is often called “half metal”, being a conductor only with respect to one of the two spin orientations ($100\,\%$ polarisation). Materials such as Fe or Ni have both the bands half filled and have therefore a partial spin polarisation (around $40-50\,\%$ [12]).

having moment oriented along the magnetisation direction, the other having moment oriented along the opposite direction. We may now expect different conductivities for the two electron populations, since they are constituted by a different number of carriers (the conductivity is always proportional to the number of carriers: no carriers, no conduction!). We conclude that in a ferromagnetic conductor there are two current components which experience quite a different resistance.

3.1.2 A GMR device

Consider an electric current flowing through a trilayer nanopillar system like the one shown in Fig. 3.2, made by one thin non-magnetic metallic layer sandwiched between two thicker ferromagnetic conductive layers. The role of the metallic layer is to separate the two ferromagnetic regions, so that they are not exchange coupled. We assume the system to be small enough that the magnetisation is homogeneous in each of the two external layers. When there is no applied magnetic field, the system relaxes to the state shown in Fig. 3.2a, with opposite orientation of the magnetisation in the two layers. This configuration is energetically favoured, because it reduces the demagnetising field in the whole sample. When a magnetic field is applied, however, the system switches to the configuration of Fig. 3.2b, where the magnetisations of the two layers are both aligned with the applied field. The two situations are shown in Fig. 3.2. We now consider a current flowing orthogonal to the layer interfaces and discuss the resistance of the sample in the two configurations. In the antiparallel case of Fig. 3.2a, each

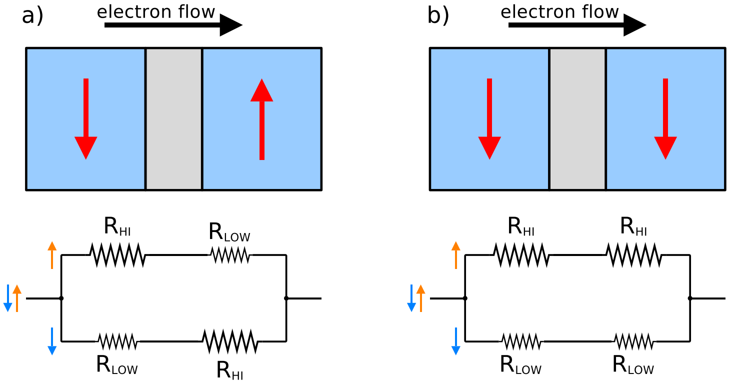

Figure 3.2: Ferromagnet/metal/ferromagnet trilayer system. The system has two possible configurations: a) no applied field. The magnetisations of the two ferromagnetic layers are antiparallel; b) an external magnetic field is applied. The two magnetisations are parallel (along the field). The resistance in the two cases is different.

of the electron populations passes through a region with parallel spin (low resistance, R_{LOW}) and through a region with antiparallel spin (high resistance, R_{HI}). The total resistance of the sample is then, $R_{\mathrm{ANTI}} = (R_{\mathrm{LOW}} + R_{\mathrm{HI}})/2$, as calculated from the equivalent electric circuit in Fig. 3.2a. In the parallel case of Fig. 3.2b, one of the two populations passes only through regions with parallel spin, while the other passes only through regions with antiparallel spin. The resistance in this case is then $R_{\mathrm{PAR}} = 2R_{\mathrm{LOW}}R_{\mathrm{HI}}/(R_{\mathrm{LOW}} + R_{\mathrm{HI}})$. The difference in resistance for the two configurations is:

$$\Delta R = R_{ANTI} - R_{PAR} = \frac{R_{\mathrm{HI}} - R_{\mathrm{LOW}}}{2(R_{\mathrm{HI}} + R_{\mathrm{LOW}})^2}.$$

We notice that such a system can be used as a magnetic sensor: if the magnetisation of one of the two layers is fixed along a know direction (due to a magnetic anisotropy, for example), a resistance measurement is enough to determine the magnetisation direction of the other layer, which is — as explained before — influenced by the external field. We conclude with a final remark concerning the direction of the current with respect to the trilayer system. In this section we have assumed the current flows in the out of plane direction. This is the so-called Current Perpendicular to the Plane (CPP) geometry. The GMR effect, however, is present also in the Current In Plane (CIP) geometry, where the current flows parallel to the plane of the layers. In fact, this is the choice which is often made in actual GMR devices [12], such as the read heads in hard disks. Indeed, while the CPP geometry usually gives rise to a high GMR effect (high *relative* variations of resistance), the actual resistances are rather small and difficult to measure [12, 13].

3.2 The spin transfer torque

The discovery of GMR proved that the resistance of a ferromagnetic conductor can depend considerably on its magnetisation configuration. This means that there is an interaction between the conduction electrons and the magnetisation, which can lead to changes in the electric conductivity. We may argue that — following the third Newton's law — if the magnetisation can affect the flow of an electric current, there should be also an effect in the opposite direction: the flow of an electric current may affect the magnetisation dynamics. Studies of the interaction between a spin polarised current and the magnetisation of a ferromagnetic conductor were carried out in the seventies by the pioneering works of Berger [14], who already predicted the possibility for a current to move a domain wall. Only in 1996, however, the spin transfer torque between the itinerant electrons and the magnetisation was quantitatively taken into account in two independent works by Slonczewski [3] and Berger [9], and the Landau-Lifshitz-Gilbert equation was extended by adding the so-called spin transfer torque, the torque exerted by the electric spin polarised current on the magnetisation. These works predicted, on the one hand, the possibility for steady magnetisation precession driven by a constant electric current and, on the other, the possibility for current driven switching of the magnetisation. Both phenomena are relevant for applications such as microwave generation and magnetic random access memories (MRAM) and greatly stimulated the research on spintronics in the last decade. The research field is today very active. Here we mention two research areas which are particularly relevant for the studies presented in this thesis:

- The research area focusing on multilayered films and nanopillars similar to the one of Fig. 3.2, often called spin-valves. This is the system considered by Slonczewski in the aforementioned paper [3]. The difference with respect to the GMR setup lies in the higher current density regime: if in the GMR effect the applied electric current is weak and is used just to probe the magnetisation of the free ferromagnetic layer, in the case considered by Slonczewski, the current is stronger and is used to actively control the dynamics of the magnetisation in the free layer. The theoretical description of Slonczewski has been experimentally verified, showing that the spin transfer can indeed induce switching [15, 16] and magnetisation precession [10, 17].

- The research area studying systems made by a single homogeneous ferromagnetic material, such as ferromagnetic nanowires or films, where a spin polarised electric current interacts with the magnetisation patterns developed inside the sample, such as domain walls or vortices. This is a quite recent area of research and has received considerable attention both from theoretical and experimental studies. It has been experimentally shown that a current flowing through a ferromagnetic nanowire can induce the movement of the domain walls which are developed inside it (see Fig. 3.3). Such studies [18, 19, 20] have also been explained with theoretical models [21]. These models are often[1] based on the theory by Zhang and Li [23], where the Landau-Lifshitz equation is extended by including additional torques, which capture the interaction between an electric current and a locally inhomogeneous magnetisation.

---

[1] Actually, several models have been proposed. Initially it was assumed that the magnetic moment of the conduction electron adiabatically follows the local magnetic moment [22]. Later a non-adiabatic correction was added [23, 24].

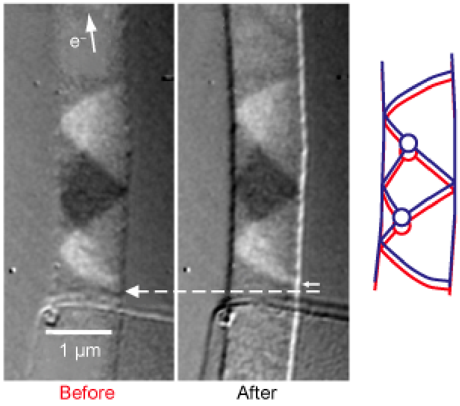

Figure 3.3: Magnetic transmission X-ray microscopy (MTXM) showing a domain wall inside a nanowire. A current pulse ($j \sim 10^{12}\,\mathrm{A/m^2}$) can be used to move it. Repetitive measurements reveal the stochastic nature of the current induced domain wall motion (reproduction from [20]).

The main problem in both the two research areas is that the current density required in order to obtain significant effects is often too high (between 10^{10} and $10^{12}\,\mathrm{A/m^2}$), causing excessive Joule heating and thus the meltdown or deterioration of the sample. There is then a high interest in finding systems where the spin transfer torque effects are maximised and require lower current density. In this thesis we investigate exchange spring systems in the form of multilayer films, a case which lies between the case of spin-valve and the case of homogeneous ferromagnetic nanowire. Indeed, exchange spring systems are multilayer systems which still can develop artificial domain walls with shape and size which can be controlled, first, during manufacturing (by selecting a suitable geometry) and, later, by applying an appropriate magnetic field. This is an extremely important feature, since the size and shape of a domain wall have a critical role in determining its interaction with the applied electric current [18]. Moreover the recent experimental discovery of significant GMR in exchange spring multilayers [25], suggests that spin-transfer-torque may play a role in these systems.

The numerical spin-transfer studies that we present in this thesis are all based on the Zhang-Li model, the same model [23] which has been successfully employed in the theoretical understanding of current-driven domain wall motion in ferromagnetic nanowires. The applicability of this model to systems made by different materials, such as exchange spring systems, needs to be discussed carefully, since the different spin transport properties of the layers may lead to effects which are not taken into account by the model. We will return on this point later in the thesis. In the next section we enter into the details of the derivation of the Zhang-Li model, exploring closely the physics of spin transport in ferromagnets with inhomogeneous magnetisation configuration.

3.3 The Zhang-Li model

The theories which extend the Landau-Lifshitz equation (2.3) by taking into account the effect of the spin transfer from the current to the magnetisation usually start from a common distinction between conduction electrons and localised electrons. Their main objective is to take into account the dynamics and the interaction between the magnetic moments of the two "kinds" of electrons. We may classify these theories into three groups:

- adiabatic theories, which consider the limit of smoothly varying magnetisation, where the magnetic moment of the itinerant electrons follows closely the direction of the local magnetisation. This is the case considered — for example — by the Zhang-Li model;
- the strongly non adiabatic theories (the opposite limit), where a spin polarised current is injected into a region where the magnetisation is oriented differently. This is the case considered — for example — by the Slonczewski model;
- non adiabatic theories (between the two limits). These theories usually are forced to take into account the magnetic moment of the conduction electrons in an explicit manner. As a result, the usual micromagnetic description based on the Landau-Lifshitz equation, has to be extended quite radically by adding a new equation of motion for the magnetisation of the conduction electrons and its coupling with the ordinary, localised magnetisation [26].

The Zhang-Li theory belongs to the first group; it gets to a correction of the Landau-Lifshitz equation where the effect of the spin polarised current is described by a small number of parameters.

3.3.1 Introduction

The magnetisation $\vec{M}$ in a ferromagnet is defined such that $\vec{M}(\vec{r},\, t)\, \mathrm{d}^3 r$ is the magnetic moment contained in the volume $\mathrm{d}^3 r$ centered in $\vec{r}$. In a ferromagnetic conductor, however, beside the magnetic moment coming from the localised electrons, we should also consider the magnetic moment coming from the conduction electrons. We then can

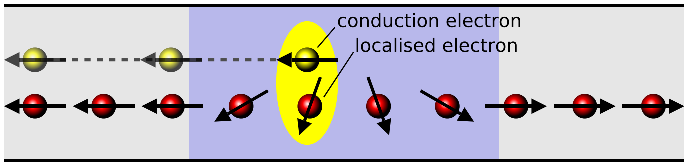

Figure 3.4: Visualisation of the spin transfer process between a conduction electron (yellow) and a localised electron (red). The region where the magnetisation changes in space is coloured with blue. The yellow shadow represents the interaction between the spins.

define two vector fields. The first one, $\vec{M}(\vec{r}, t)$, is the magnetisation and is originated by the localised electrons. The second one, $\vec{m}(\vec{r}, t)$, is the *conduction electron spin density* and is defined in a similar way[2]: $\vec{m}(\vec{r}, t)\, \mathrm{d}^3 r$ is the amount of magnetic moment due to the conduction electrons in the volume $\mathrm{d}^3 r$.

If the effects of $\vec{m}$ are neglected, the dynamics of the magnetisation $\vec{M}$ can be described by the LLG (Landau-Lifshitz-Gilbert) equation. However, when an electric current flows throughout a non homogeneous magnetisation, we may expect a considerable misalignment between $\vec{m}$ and $\vec{M}$. In other words, a conduction electron travelling in a non homogeneous magnetisation can "get close" to a localised electron which has different spin orientation. There may then be a spin transfer between the two electrons, due to the exchange coupling, which acts to align the two spins. A rough visualisation of the process is shown in Fig. 3.4. The interaction between the itinerant electrons and the localised electrons is usually described by an "s-d" Heisenberg Hamiltonian $\mathbf{H}_{\text{sd}} = -J_{\text{ex}} \mathbf{S} \cdot \mathbf{s}$, where J_{ex} is the exchange coupling constant and $\mathbf{S}$, $\mathbf{s}$ are the operators corresponding to the spin of localised and conduction electrons, respectively.

The Zhang-Li model aims to find how this physics affects the magnetisation dynamics and how it can be included in the LLG equation for $\vec{M}$.

3.3.2 The dynamics of the itinerant spins

There are two dynamics which the model identifies: the dynamics of the magnetisation $\vec{M}$ and the dynamics of the itinerant spin density $\vec{m}$. The model assumes that the dynamics of $\vec{m}$ is much faster than that of $\vec{M}$ and can be treated as if it was decoupled from it. This approximation allows one to write down a dynamic equation for $\vec{m}$ where

---

[2] We notice that $\vec{M}$ and $\vec{m}$ have the same units: they both are densities of magnetic moment. The nomenclature "conduction electron spin density", which is used in the original paper, seems to suggest that $\vec{m}$ is actually a spin density, but it isn't!

$\vec{M}$ is treated as a background still vector field:

$$\partial_t \vec{m} + \vec{\nabla} \cdot \vec{j}_{\mathrm{s}} = -\frac{1}{\tau_{\mathrm{ex}} M_{\mathrm{sat}}} \vec{m} \times \vec{M} - \frac{\delta \vec{m}}{\tau_{\mathrm{sf}}}, \tag{3.1}$$

where τ_{ex} is the exchange relaxation time and gives the typical time scale for the exchange interaction between $\vec{M}$ and $\vec{m}$ (τ_{ex} is greater for a weaker coupling). Similarly, τ_{sf} is the spin-flip relaxation time and refers to the spin-flip process, which we discuss later in this section.

In the original paper this equation is derived from a quantum mechanical formulation. Here we omit the derivation and focus more on the meaning of the equation. We show that this equation is a natural adaptation of the LLG equation (2.2) to the dynamics of the itinerant spins.

In Sec. 2.2 we presented a simple classical justification of the LLG equation. We considered the total magnetic moment $\vec{\mu}$ contained inside a small volume $\mathrm{d}r^3$ and related its time derivative to the torque acting on it. We finally concluded that $\vec{\mu}$ can change for two reasons: because of the torque exerted by the effective field (which gives rise to the precession term in the LLG equation) and because of the damping processes (which give rise to the damping term). When considering the dynamics of the itinerant electrons, this derivation must be revised. In particular, there is a third reason why $\vec{\mu}$ may change in time: the conduction electrons are moving and hence there is a flux of magnetic moment through the surface of the volume $\mathrm{d}r^3$. It is then natural to substitute the left hand side of the LLG equation (which is just $\partial_t \vec{m}$) with $\partial_t \vec{m} + \vec{\nabla} \cdot \vec{j}_{\mathrm{s}}$, which is the variation of $\vec{m}$, without the contribution given by the flux of $\vec{m}$. $\vec{j}_{\mathrm{s}}$ is the current associated with $\vec{m}$ and is a tensor field, since $\vec{m}$ is a vector field. We return to its definition later. We notice that, if we ignore all the interactions involving $\vec{m}$ in (3.1), we get the continuity equation for $\vec{m}$: $\partial_t \vec{m} + \vec{\nabla} \cdot \vec{j}_{\mathrm{s}} = 0$.

The right hand side of equation (3.1) can be similarly related to the right hand side of the LLG equation. The first term is indeed the torque exerted by the effective field, where the only interaction taken into account is the coupling with the magnetisation $\vec{M}$. Here we should point out that indeed this is the only interaction which is considered for the itinerant electrons: direct contributions from the external field and from the demagnetising field are neglected. Finally, the last term in (3.1), $-\frac{\delta \vec{m}}{\tau_{\mathrm{sf}}}$, is a phenomenological damping term. $\delta \vec{m}$ is the spin accumulation and is defined as

$$\delta \vec{m} = \vec{m} - \vec{m}_0, \tag{3.2}$$

where $\vec{m}_0(\vec{r}, t)$ is the equilibrium spin density in $\vec{r}$. This term models the scattering of the conduction electrons with impurities in the crystal lattice, with other electrons and

— in general — it models all the phenomena which induce $\vec{m}$ to relax to an equilibrium value $\vec{m}_0$. It is analogous to the familiar damping term $-\frac{\gamma}{M_{\mathrm{sat}}}\vec{M} \times \partial_t\vec{M}$ of the LLG equation, with a difference: the norm of $\vec{m}$ is not necessarily preserved in time.

The exchange interaction between $\vec{M}$ and $\vec{m}$ wants to align the two vector fields. Then, it is reasonable to take $\vec{m}_0 = n_0\,\vec{M}/M_{\mathrm{sat}}$ in (3.2), so that:

$$\vec{m}(\vec{r},\,t) = \vec{m}_0(\vec{r},\,t) + \delta\vec{m}(\vec{r},\,t) = n_0\,\vec{M}(\vec{r},\,t)/M_{\mathrm{sat}} + \delta\vec{m}(\vec{r},\,t). \tag{3.3}$$

Here n_0 is the equilibrium density of the itinerant spin, oriented along the direction of $\vec{M}$. This assumption, together with equation (3.1), implies that, when $\vec{j}_{\mathrm{s}} = 0$, $\delta\vec{m} = 0$ is the equilibrium state towards which the system relaxes. In other words, when the spin current is zero, the spin of the conduction electrons $\vec{m}$ relaxes to follow everywhere the direction of the magnetisation $\vec{M}$.

3.3.3 The spin current density

Equation (3.1) alone is not enough to study the dynamics of $\vec{m}$. In particular, we miss a characterisation of the spin current $\vec{j}_{\mathrm{s}}$ and its relationship with $\vec{m}$ and $\vec{M}$. It may be useful — at this point — to recall how the electric charge density ρ_{e} and the electric current density $\vec{j}_{\mathrm{e}}$ are defined. Using μ as a component index,

$$\begin{aligned} \rho_{\mathrm{e}} &= -e\,\rho, \\ j_{\mathrm{e}}^{\mu} &= \rho_{\mathrm{e}}\,v^{\mu} = -e\,\rho\,v^{\mu}, \end{aligned}$$

where ρ is the number density, v is the drift velocity and $-e$ is the electric charge of the electrons. Similarly, we define:

$$\begin{aligned} m^{\nu} &= P\mu_{\mathrm{B}}\,\rho\,u^{\nu}, \\ j_{\mathrm{s}}^{\mu\nu} &= m^{\nu}\,v^{\mu} = -\frac{P\mu_{\mathrm{B}}}{e}\,j_{\mathrm{e}}^{\mu}\,u^{\nu}, \end{aligned}$$

where μ_{B} is the Bohr magneton (the magnetic moment of each electron), P is the spin polarisation and $\vec{u} = \vec{m}/m$ is the direction of $\vec{m}$. In the previous section we saw that $\vec{u}$ gets parallel to $\vec{M}$, when the spin current $\vec{j}_{\mathrm{s}}$ is zero. When an electric current is applied this is not exactly true. We can then define:

$$j_{\mathrm{s}}^{\mu\nu}(\vec{r},\,t) = -\frac{P\mu_{\mathrm{B}}}{e}\,j_{\mathrm{e}}^{\mu}\,\frac{M^{\nu}(\vec{r},\,t)}{M_{\mathrm{sat}}} + \delta j_{\mathrm{s}}^{\mu\nu}(\vec{r},\,t). \tag{3.4}$$

We note that the divergence $\vec{\nabla}\cdot\vec{j}_{\mathrm{s}}$ in (3.1) is done using the index μ as the running index: $(\vec{\nabla}\cdot\vec{j}_{\mathrm{s}})^{\nu} = \sum_{\mu}\partial_{\mu}j_{\mathrm{s}}^{\mu\nu}$. To complete the picture and get to a closed form for the nonequilibrium spin density $\delta\vec{m}$, we take:

$$\delta\vec{j}_{\mathrm{s}} = -D_0 \nabla \delta\vec{m}, \tag{3.5}$$

where D_0 is a diffusion constant. We then see that our definition of spin current density (3.4) includes two contributions. On the one hand, we have a contribution from the current of electrons induced by the electric field: a current of charge is also a current of spin. On the other hand, we have a spontaneous diffusion of spins from regions with higher spin density to regions with lower density.

3.3.4 The nonequilibrium spin density

We can now substitute Eqs. (3.5), (3.4) and (3.3) into (3.1) and get:

$$\frac{n_0}{M_{\mathrm{sat}}}\,\partial_t\vec{M} + \partial_t\delta\vec{m} - \frac{P\mu_{\mathrm{B}}}{e\,M_{\mathrm{sat}}}\,(\vec{j}_{\mathrm{e}}\cdot\vec{\nabla})\vec{M} - D_0\,\nabla^2\delta\vec{m} = -\frac{1}{\tau_{\mathrm{ex}}M_{\mathrm{sat}}}\delta\vec{m}\times\vec{M} - \frac{\delta\vec{m}}{\tau_{\mathrm{sf}}},$$

We now neglect $\partial_t\delta\vec{m}$, which corresponds to assume linear response of $\delta\vec{m}$ to the electric current j_{e} and to the time derivative of the magnetisation $\partial_t\vec{M}$. We return to this assumption in Sec. 3.3.6. We get:

$$D_0\,\nabla^2\delta\vec{m} - \frac{1}{\tau_{\mathrm{ex}}M_{\mathrm{sat}}}\delta\vec{m}\times\vec{M} - \frac{\delta\vec{m}}{\tau_{\mathrm{sf}}} = \frac{n_0}{M_{\mathrm{sat}}}\,\partial_t\vec{M} - \frac{P\mu_{\mathrm{B}}}{e\,M_{\mathrm{sat}}}\,(\vec{j}_{\mathrm{e}}\cdot\vec{\nabla})\vec{M}. \tag{3.6}$$

This is a closed form equation for the nonequilibrium spin density $\delta\vec{m}$.

We now make an important approximation to simplify Eq. (3.6): we assume that the magnetisation changes slowly in space and that the first term on the left hand side of Eq. (3.6) can be neglected. Then the equation becomes:

$$\delta\vec{m} = -\frac{n_0\tau_{\mathrm{sf}}}{M_{\mathrm{sat}}}\,\partial_t\vec{M} + \frac{P\mu_{\mathrm{B}}\tau_{\mathrm{sf}}}{e\,M_{\mathrm{sat}}}\,(\vec{j}_{\mathrm{e}}\cdot\vec{\nabla})\vec{M} - \frac{\tau_{\mathrm{sf}}}{\tau_{\mathrm{ex}}M_{\mathrm{sat}}}\vec{M}\times\delta\vec{m}. \tag{3.7}$$

Substituting this equation into itself (into its last member on the right hand side) we get:

$$\begin{aligned}\delta\vec{m}\,(1+\xi^2) - \frac{1}{M_{\mathrm{sat}}^2}\,\vec{M}\,(\vec{M}\cdot\delta\vec{m}) \quad &= \quad -\frac{\tau_{\mathrm{ex}}\xi n_0}{M_{\mathrm{sat}}}\,\partial_t\vec{M} + \frac{\tau_{\mathrm{ex}}\xi P\mu_{\mathrm{B}}}{eM_{\mathrm{sat}}}\,(\vec{j}_{\mathrm{e}}\cdot\vec{\nabla})\vec{M} \\ &\quad -\frac{\tau_{\mathrm{ex}}n_0}{M_{\mathrm{sat}}^2}\,\vec{M}\times\partial_t\vec{M} + \frac{\tau_{\mathrm{ex}}P\mu_{\mathrm{B}}}{e\,M_{\mathrm{sat}}^2}\,\vec{M}\times(\vec{j}_{\mathrm{e}}\cdot\vec{\nabla})\vec{M},\end{aligned} \tag{3.8}$$

where we have introduced the quantity $\xi = \tau_{\mathrm{ex}}/\tau_{\mathrm{sf}}$ and we have decomposed the triple vector product $\vec{M}\times(\vec{M}\times\delta\vec{m})$ as $\vec{M}\times(\vec{M}\times\delta\vec{m}) = \vec{M}\,(\vec{M}\cdot\delta\vec{m}) - M_{\mathrm{sat}}^2\,\delta\vec{m}$. The second term on the left hand side of Eq. (3.8) vanishes, since $\vec{M}\cdot\delta\vec{m} = 0$. Indeed, by looking at (3.7), we see that $\delta\vec{m}$ is the sum of three vectors which are all orthogonal to $\vec{M}$ (remember that any partial derivative of $\vec{M}$ is orthogonal to $\vec{M}$, since $\vec{M}$ has constant norm: $\vec{M}\cdot\partial\vec{M} = \partial M_{\mathrm{sat}}^2/2 = 0$). We then have:

$$\delta\vec{m} = \tau_{\mathrm{ex}}\left(-\frac{\xi u}{M_{\mathrm{sat}}}\,\partial_t\vec{M} - \frac{u}{M_{\mathrm{sat}}^2}\,\vec{M}\times\partial_t\vec{M} + \xi v\,(\hat{j}_{\mathrm{e}}\cdot\vec{\nabla})\vec{M} + v\,\vec{M}\times(\hat{j}_{\mathrm{e}}\cdot\vec{\nabla})\vec{M}\right), \quad (3.9)$$

where $\hat{j}_{\mathrm{e}} = \vec{j}_{\mathrm{e}}/j_{\mathrm{e}}$ is the direction of the electric current and

$$u = \frac{n_0}{1+\xi^2}, \qquad v = \frac{P\mu_B}{eM_{\mathrm{sat}}(1+\xi^2)}\,j_{\mathrm{e}}.$$

We can now calculate the torque on $\vec{M}$, due to $\delta\vec{m}$. Indeed, if we take a look at Eq. (3.1), we see that the transfer torque acting on $\vec{m}$, due to the interaction with $\vec{M}$, is $-\frac{1}{\tau_{\mathrm{ex}}M_{\mathrm{sat}}}\vec{m}\times\vec{M}$. Consequently, following the third Newton's law, there will be an opposite torque acting on $\vec{M}$:

$$\vec{T} = \frac{1}{\tau_{\mathrm{ex}}M_{\mathrm{sat}}}\vec{m}\times\vec{M} = -\frac{1}{\tau_{\mathrm{ex}}M_{\mathrm{sat}}}\vec{M}\times\delta\vec{m}, \quad (3.10)$$

where we have substituted $\vec{m} = \vec{m}_0 + \delta\vec{m}$. We can now substitute (3.9) into (3.10) and obtain

$$\begin{aligned}\vec{T} &= \frac{1}{M_{\mathrm{sat}}}\vec{M}\times\left(\frac{\xi u}{M_{\mathrm{sat}}}\,\partial_t\vec{M} + \frac{u}{M_{\mathrm{sat}}^2}\,\vec{M}\times\partial_t\vec{M} - \xi v\,(\hat{j}_{\mathrm{e}}\cdot\vec{\nabla})\vec{M} - v\,\vec{M}\times(\hat{j}_{\mathrm{e}}\cdot\vec{\nabla})\vec{M}\right)\\ &= \frac{\xi u}{M_{\mathrm{sat}}^2}\,\vec{M}\times\partial_t\vec{M} - \frac{u}{M_{\mathrm{sat}}}\,\partial_t\vec{M} - \frac{\xi v}{M_{\mathrm{sat}}}\,\vec{M}\times(\hat{j}_{\mathrm{e}}\cdot\vec{\nabla})\vec{M} - \frac{v}{M_{\mathrm{sat}}}\,\vec{M}\times(\vec{M}\times(\hat{j}_{\mathrm{e}}\cdot\vec{\nabla})\vec{M}).\end{aligned}$$

These four extra terms should be added to the right hand side of the LLG equation to take into account the spin transfer torque between the magnetisation and the itinerant electrons. The first two terms do not depend on the electric current and are therefore present even when $j_{\mathrm{e}} = 0$. These terms are due to the spin accumulation which is caused by the time variations of the magnetisation. The last two terms include a direct contribution from the electric current. The associated spin transfer torques arise whenever the conduction electrons flow through a region where the magnetisation is not homogeneous in space. The first two terms lead to a renormalisation of the gyromagnetic ratio and the damping parameter. In other words their effect is just to slightly change the two parameters γ and α which characterise the dynamics in the LLG equation (2.2). They typically lead to 1% adjustments of the two parameters [23] and can be safely neglected, since the uncertainty on the value for such parameters is often higher than that. The last two terms, on the other hand, contain new physics and should be taken into account.

3.3.5 The corrected Landau-Lifshitz-Gilbert equation

In summary, the LLG equation with the inclusion of the torques induced by the spin transfer between the itinerant electrons and the localised magnetisation is:

$$\begin{aligned}\partial_t \vec{M} &= -\gamma\, \vec{M} \times \vec{H} + \frac{\alpha}{M_{\mathrm{sat}}}\, \vec{M} \times \partial_t \vec{M} \\ &\quad -\frac{v}{M_{\mathrm{sat}}^2}\, \vec{M} \times (\vec{M} \times (\hat{j}_{\mathrm{e}} \cdot \vec{\nabla})\vec{M}) - \frac{\xi v}{M_{\mathrm{sat}}}\, \vec{M} \times (\hat{j}_{\mathrm{e}} \cdot \vec{\nabla})\vec{M}. \qquad (3.11)\end{aligned}$$

We give here a summary of the quantities appearing in the equation: $\vec{M}$ is the magnetisation, $M_{\mathrm{sat}} = \|\vec{M}\|$ is the saturation magnetisation, $\vec{H}$ is the effective magnetic field, γ is the gyromagnetic ratio, α is the damping parameter. The current density is applied along the unit vector $\hat{j}_{\mathrm{e}}$ and enters the model through the parameter $v = \frac{P\mu_B}{eM_{\mathrm{sat}}(1+\xi^2)}\, j_{\mathrm{e}}$, where P is the degree of polarisation of the spin current, μ_B is the Bohr magneton, e the absolute value of the electron charge, $\xi = \tau_{\mathrm{ex}}/\tau_{\mathrm{sf}}$ is the ratio between the exchange relaxation time and the spin-flip relaxation time. In this thesis we will consider the case where the electric current flows in the positive x direction. Then, the equation becomes:

$$\begin{aligned}\partial_t \vec{M} &= -\gamma\, \vec{M} \times \vec{H} + \frac{\alpha}{M_{\mathrm{sat}}}\, \vec{M} \times \partial_t \vec{M} \\ &\quad -\frac{v}{M_{\mathrm{sat}}^2}\, \vec{M} \times (\vec{M} \times \partial_x \vec{M}) - \frac{\xi v}{M_{\mathrm{sat}}}\, \vec{M} \times \partial_x \vec{M}. \qquad (3.12)\end{aligned}$$

In our model M_{sat} is uniform in space and constant in time. We can then obtain an explicit form for equation (3.12):

$$\begin{aligned}\partial_t \hat{M} &= -\gamma'\, \hat{M} \times \vec{H} - \gamma'\alpha\, \hat{M} \times (\hat{M} \times \vec{H}) \\ &\quad -av'\, \hat{M} \times (\hat{M} \times \partial_x \hat{M}) - \overline{a}v'\, \hat{M} \times \partial_x \hat{M}, \qquad (3.13)\end{aligned}$$

where $\hat{M} = \vec{M}/M_{\mathrm{sat}}$ is a unit vector and $\gamma' = \gamma/(1+\alpha^2)$, $v' = v/(1+\alpha^2)$. We use the notation $\partial_t \equiv \frac{\partial}{\partial t}$ and $\partial_x \equiv \frac{\partial}{\partial x}$. The two dimensionless coefficients a and $\overline{a}$ are $a = 1 + \alpha\xi$ and $\overline{a} = \xi - \alpha$.

3.3.6 Discussion

We conclude by making two observations about the assumptions underlying the model. Firstly, the laplacian in (3.6) can be omitted only when $\delta\vec{m}$ varies slowly in space. The order of magnitude of the length scale where $\delta\vec{m}$ is supposed to change linearly (so that $\nabla^2\delta\vec{m} = 0$) can be calculated [23] as $\lambda = \sqrt{D_0\tau_{\mathrm{ex}}}$ (here we assume $\xi \sim 0.01 \ll 1$). For Permalloy, $D_0 = 2\,\mathrm{nm}$. We must then be sure that the magnetisation of the system does change smoothly in this length scale. In particular, the Zhang-Li model is not suitable to characterise multilayer systems, where the magnetisation changes abruptly at the interfaces between the layers.

A second approximation we want to discuss is the one which was made in Eq. (3.7), where the time derivative of $\partial_t \delta\vec{m}$ was neglected. Without this approximation we would have obtained:

$$\frac{\delta\vec{m}}{n_0} = -\,\partial_{t/\tau_{\mathrm{sf}}}\hat{M} + (c\vec{j}_{\mathrm{e}}\cdot\vec{\nabla})\hat{M} - \frac{1}{\xi}\,\hat{M}\times\frac{\delta\vec{m}}{n_0} - \partial_{t/\tau_{\mathrm{sf}}}\frac{\delta\vec{m}}{n_0}, \tag{3.14}$$

where $\hat{M} = \vec{M}/M_{\mathrm{sat}}$, $c = \frac{P\mu_{\mathrm{B}}\tau_{\mathrm{sf}}}{en_0}$ and $\tau_{\mathrm{sf}}\partial_t \equiv \partial_{t/\tau_{\mathrm{sf}}}$. Notice that $\hat{M}$, $\delta\vec{m}/n_0$, $\partial_{t/\tau_{\mathrm{sf}}}$ and $c\vec{j}_{\mathrm{e}}\cdot\vec{\nabla}$ are all dimensionless vectors/operators. Substituting recursively this equation into itself leads to a series of terms containing $\partial^n_{t/\tau_{\mathrm{sf}}}\hat{M}$ and $cj_{\mathrm{e}}\,\partial^m_{t/\tau_{\mathrm{sf}}}\hat{M}$. We can expect both the two contributions to decay rapidly as n and m increase. Indeed, $\partial_{t/\tau_{\mathrm{sf}}}\hat{M}$ is small when the variation in time of $\hat{M}$ happens in timescales much greater than $\tau_{\mathrm{sf}} \sim 1\,\mathrm{ps}$ (from [23]). We can then keep only the terms in (3.14) which are linear in $\partial_{t/\tau_{\mathrm{sf}}}\hat{M}$ and j_{e}. This corresponds to neglect $\partial_t\delta\vec{m}$.

Chapter 4

Method

In this chapter we briefly present the main ideas beyond our computational approach starting with the finite element method (FEM) and then focusing on the integration algorithms we used to solve the dynamical equations of micromagnetics.

4.1 Finite difference and finite element methods

We have seen that in micromagnetics the configuration of the system is represented by the magnetisation, a vector field defined over all the ferromagnetic body. Obviously computers are discrete machines and cannot handle such a continuous representation of vector fields. Consequently a discretisation of the system is required and is usually obtained using two different techniques: finite difference and finite element methods.

In finite difference methods the space is discretised by a decomposition in rectangles or cuboids. The fields are piecewise constant functions which change abruptly only at the interfaces between adjacent cuboids. This is the approach used by OOMMF [27], one widely used simulation package developed at NIST. Finite difference (FD) methods are relatively easy to implement, but, unfortunately, they suffer a number of problems. First of all, bodies with smooth curved surfaces are badly approximated by aggregates of cuboids. For example, the FD discretisation of a sphere has inevitably a "staircase" boundary, which is a particular annoying and unwanted artifact, considering that the demagnetising field tends to align the magnetisation with the surface of the magnetic body. To avoid a poor representation of the boundaries it would then be desirable to increase the mesh resolution only near the surfaces, while keeping it lower at the centers of the bodies. This is not allowed by the finite difference approach. As a results many kinds of nanogeometries are not well modelled and usually require too many cuboids to be simulated in reasonable times. Another problem of the finite difference approach comes from the requirement to fit the magnetic structure inside a cubic grid: if the body is not a cuboid (a sphere for example), then it cannot fill the whole grid, meaning that a considerable part of the mesh corresponds to the empty space. This leads to a considerable waste of memory, which becomes critical if the structure to be simulated is a magnetic shell (imagine a thin spherical magnetic layer covering a non-metallic sphere such as the one shown in Fig. 4.1, for example).

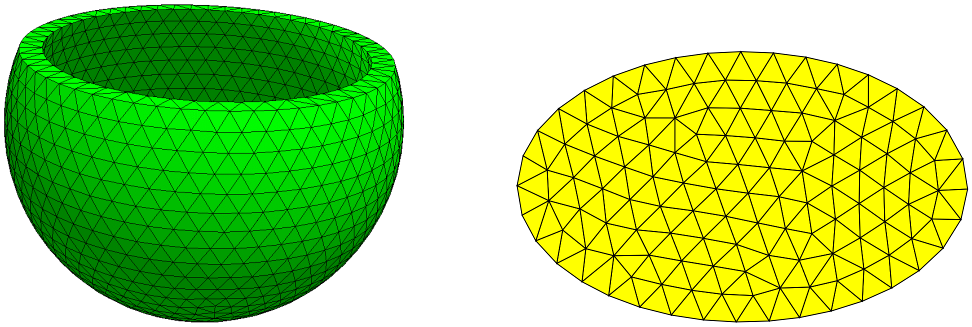

Figure 4.1: Example of two dimensional (right) and three dimensional (left) unstructured mesh.

The finite element method (FEM) offers a solution to this kind of problems: the bodies are decomposed into tessellations of simplices (a simplex is the n-dimensional analogue of a triangle). These aggregates are called unstructured meshes and must satisfy a number of well defined geometrical properties (examples of unstructured meshes are given in Fig. 4.1). In this thesis, we do not enter much into the details of the mathematical theory. We only say that good meshes have simplices with shape as regular as possible: even a few flat simplices are enough to significantly deteriorate the performance of a FEM based simulation [28].

Once the mesh is given, a discretisation scheme to represent the fields can be constructed. This is done by associating to the mesh a set of basis functions. The scalar or vector fields are then expressed as linear combinations of these basis functions. We will briefly explain the underlying idea with an example. Consider a triangle $\mathcal{T}$ with vertices at positions $\vec{P}_1$, $\vec{P}_2$ and $\vec{P}_3$ in a two dimensional mesh. Suppose $a(\vec{r} \in \mathcal{T}) \in \mathbb{R}$ is a scalar field defined over the triangle. Let's call $L_k(\vec{r})$ a linear scalar function which is defined to be equal to one at the k-th vertex and zero at the other vertices (see Fig. 4.2). The function a could be approximated by $\tilde{a}(\vec{r}) = a_1 L_1(\vec{r}) + a_2 L_2(\vec{r}) + a_3 L_3(\vec{r})$, where $a_k = a(\vec{P}_k)$. It is easy to realise that $\tilde{a}$ is the linear scalar function which is equal to a at the vertices of the triangle. It is clear how one could extend these reasonings to

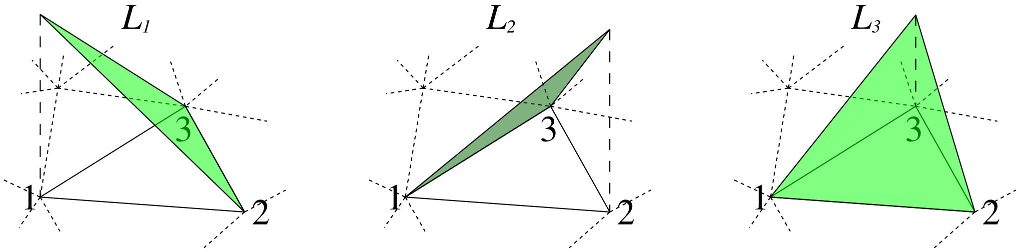

Figure 4.2: A plot of the functions L_1, L_2 and L_3 associated with a simplex (a triangle) of a two-dimensional mesh. It is shown that L_k is linear inside the triangle and takes the value one at the k-th vertex and the value zero at the other two vertices of the triangle.

obtain a piecewise linear function which approximates the the scalar field a over all the two dimensional mesh: it is enough to apply the previous procedure to every triangle of the mesh, extending the L functions to be zero outside the simplex they belong to. Grouping together all the contributions associated with each node[1] of the mesh one obtains:

$$\tilde{a}(\vec{r}) = \sum_{i=1}^{N} a_i \, e_i(\vec{r}),$$

where i runs from 1 to the total number of nodes, N, and e_i is the sum of all the L-functions of the neighbouring simplices which have r_i as a vertex and is often called "tent basis function" (see Fig. 4.3). Taking $a_i = a(\vec{r}_i)$ one obtains the piecewise linear function which is equal to a at every site of the mesh. This may not be the best

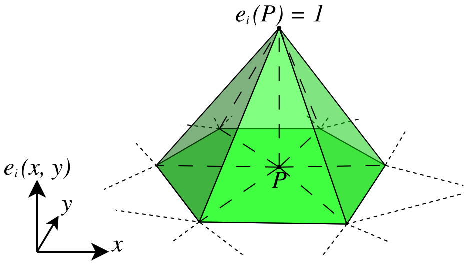

Figure 4.3: A plot of one basis function used to represent a scalar field over a two dimensional mesh with first order FEM . This basis function is given by the superposition of six L functions. One for each triangle around the site $\vec{r}_i$.

---

[1] The nodes or sites of the mesh are the vertices of its simplices.

approximation for a and one could choose other ways to project[2] a given function $a(\vec{r})$ onto the N-dimensional linear space spanned by the N functions e_i. The presentation given here is far from a rigorous formulation of the FEM theory. We gave just an example of first order representation of a scalar field on a two dimensional mesh. Higher order representations exist where the basis functions are quadratic, cubic, n-th order polynomials. There are important steps of the micromagnetic calculations, such as the calculation of the exchange field and the demagnetising field, which need to be adapted expressly to this formulation. In this thesis we do not enter into the details of such calculations, which can be found elsewhere [29, 30, 31, 32, 33].

The flexibility of FEM is evident if compared to finite difference methods. Unfortunately it has other kinds of problems. First of all the implementation is not straightforward and it requires to use additional memory in order to store the mesh and the associated geometrical information. Secondly, obtaining a good mesh is not really a trivial task, unless an external meshing software is used, such as Netgen, Gmsh or Gambit [34, 35, 36]. Requiring to use an external meshing program is certainly a disadvantage if the sample one needs to study has a simple geometry (such as a square film or a cube); it can be an advantage, however, when studying magnetic nanostructures with complex three dimensional shape.

4.2 Algorithms for time integration

In this section we present some algorithms for the integration of the LL equation (2.3). As done previously, we assume the saturation magnetisation, M_{sat}, is constant in time. For simplicity, we also assume that M_{sat} is uniform in space. We define the unit vectors $\vec{h} = \vec{H}/H$ and $\vec{m} = \vec{M}/M_{\text{sat}}$ with $H = \|\vec{H}\|$, $M_{\text{sat}} = \|\vec{M}\|$ and write the LL equation as:

$$\vec{m}' = -\gamma' \left[\vec{m} \times \vec{H} + \alpha\, \vec{m} \times (\vec{m} \times \vec{H}) \right] = f(\vec{m}, \vec{H}[\vec{m}]). \tag{4.1}$$

$\vec{m}'$ is a shorthand for $\partial_t \vec{m}$, the time partial derivative of $\vec{m}$, and $\gamma' = \frac{\gamma}{1+\alpha^2}$. This is the equation we have in mind when describing the numerical methods in the next few sections. We begin by explaining in detail the Euler method, which is the first integration algorithm which we implemented in our micromagnetic simulation package, *Nmag*. It is also the default integration scheme in the micromagnetic simulation package OOMMF [37].

---

[2] This could be done defining a scalar product over the mesh Ω (for example $\langle f,\, g \rangle = \int_\Omega f(\vec{r}) g(\vec{r}) d^2 r$) and projecting a into the basis function e_i to obtain the coefficient a_i. Note that a matrix inversion would then be necessary, since the basis $\{e_i\}_i$ is not orthogonal.

4.2.1 Euler method and step-length adjustment

In what follows we discuss the Euler method to integrate the LLG equation as it is implemented in the micromagnetic simulation package OOMMF [27]. Many of the ideas presented here have, however, a more general validity and can be found in the books on numerical methods [38].

The Euler method is probably the simplest method to numerically integrate the LL equation. Given the initial configuration for the normalised magnetisation $\vec{m}_{0,i}$, we use the following recursive relation:

$$\vec{m}_{n+1,i} = \vec{m}_{n,i} + (t_{n+1} - t_n)\,\vec{m}'_{n,i}. \tag{4.2}$$

$\vec{m}_{n,i}$ is the approximation of the magnetisation computed at time t_n, and $\vec{m}'_{n,i}$ is its derivative with respect to time. The index i refers to the position in space $\vec{r}_i$, which needs to be discretised in some way.[3] Eq. (4.2) is used to obtain the magnetisation $\vec{m}_{n+1}$ at time $t_{n+1} = t_n + \Delta t_n$ from the magnetisation $\vec{m}_n$ at time t_n. The procedure is as follows:

- from $\vec{m}_n$ calculate the effective field $\vec{H}$ (this step is time consuming, since it requires the calculation of the demagnetising field, the exchange field, etc.);
- use the LL equation to calculate $\vec{m}'_n$ from $\vec{m}_n$ and $\vec{H}_n$;
- use the Eq. (4.2) to compute the time evolution and obtain $\vec{m}_{n+1}$;
- iterate until convergence is reached.

The method can be derived easily. We denote with $\vec{m}(\vec{r}, t)$ the exact solution of the LL equation with $\vec{m}(\vec{r}_i, t_0) = \vec{m}_{0,i}$ taken as initial condition. We write its Taylor expansion with respect to time in $t = t_n$:

$$\vec{m}(\vec{r}, t_n + \Delta t) = \vec{m}(\vec{r}, t_n) + \Delta t\,\vec{m}'(\vec{r}, t_n) + \frac{1}{2}(\Delta t)^2\,\vec{m}''(\vec{r}, t_n) + \dots$$

If Δt is small enough, we can get an approximation of the magnetisation at time $t_{n+1} = t_n + \Delta t$, by truncating the expansion at the first order in Δt. We start with $t = t_0$ and obtain $\vec{m}_{1,i}$, then we iterate this procedure over and over again to calculate the magnetisation at the following times, thus obtaining the Euler method.

We could take a constant $\Delta t_n = t_{n+1} - t_n = \Delta t$ and use $t_n = n\,\Delta t$. But what is a good choice for Δt? How can we choose a Δt which is small enough to achieve the

---

[3] For the finite element method, $\vec{m}_{n,i}$ is the coefficient relative to the i-th tent function of the chosen basis.

required accuracy, without wasting time due to a too small Δt? And moreover, is it a good idea to use a Δt which is constant throughout all the simulation? We can answer all these questions if we find a way to calculate the error related with a particular "move" of our Euler integrator.

To do this, we consider again the Taylor expansion of the exact magnetisation. If Δt is very small, then we can write:

$$\vec{m}(\vec{r}, t_n + \Delta t) = \vec{m}(\vec{r}, t_n) + \Delta t\, \vec{m}'(\vec{r}, t_n) + \Delta \vec{m}_n^{\text{err}},$$

where:

$$\Delta \vec{m}_n^{\text{err}} \approx \frac{1}{2}(\Delta t)^2\, \vec{m}''(\vec{r}, t_n) \approx \frac{1}{2}\Delta t\, \left(\vec{m}'(\vec{r}, t_{n+1}) - \vec{m}'(\vec{r}, t_n)\right).$$

Since Δt is small, the terms of higher orders are negligible compared to the one of second order. This gives us a method to check the result of our Euler-based integrator. We define the error for the step n as:

$$\epsilon_{n,i} = \frac{1}{2}\Delta t_n \left\| \vec{m}'_{n+1,i} - \vec{m}'_{n,i} \right\|. \tag{4.3}$$

Since $\vec{m}$ has unit norm, its movement $\Delta m_{n,i} = \|\vec{m}_{n+1,i} - \vec{m}_{n,i}\|$ during the n-th time step is expressed in radians. $\epsilon_{n,i}$ is the error related to such a movement and shares therefore the same unit of measurement.

There are two requirements we can make over the error ϵ. We introduce an "absolute error" ϵ_A and require that for all the steps and all the positions,

$$\epsilon_{n,i} < \epsilon_A. \tag{4.4}$$

This will set the resolution in the calculated trajectory of the magnetisation.

We introduce another check: the error in the movement should be lower than the movement itself. This is really important: it does not make much sense to move by 0.1 radians, when the associated error is 0.09 radians! We need to be sure that $\epsilon_{n,i} \ll \|\Delta \vec{m}_{n,i}\|$, so we introduce another parameter, the "relative error" ϵ_R, and we require that $\epsilon_{n,i} < \epsilon_R \|\Delta \vec{m}_{n,i}\|$. $\Delta \vec{m}_{n,i}$ is the change in $\vec{m}$ relative to the n-th step, which in the Euler case is simply $\vec{m}'_n \Delta t_n$:

$$\epsilon_{n,i} < \epsilon_R \left\| \vec{m}'_{n,i} \right\| \Delta t_n. \tag{4.5}$$

Imposing this relation on all the positions may be too restrictive. Imagine we have a point i_0 where Eq. (4.5) does not hold, but $\vec{m}$ does not change significantly. We may have $\left\| \vec{m}'_{n,i_0} \right\| \Delta t_n < 10^{-6}$ radians for example. Even if the error for this position is high, the move does not produce a relevant modification of the configuration here.

Rejecting the move, however, would be a waste of time, if somewhere else things were going better. For this reason we define $\left\|\vec{m}'_{n,\max}\right\|$ to be the maximum value of $\left\|\vec{m}'_{n,i}\right\|$, for the running index i, and we make the following requirement:

$$\epsilon_{n,i} < \epsilon_R \left\|\vec{m}'_{n,\max}\right\| \Delta t_n,$$

for all positions i and times n. We can collect these two requirements into the following expression:

$$\epsilon_{n,i} < \epsilon_{n,\min} = \min\left\{\epsilon_A, \, \epsilon_R \left\|\vec{m}'_{n,\max}\right\| \Delta t_n\right\}. \tag{4.6}$$

This provides a method that allows us to check whether a particular time integration step was well done or not. Actually we can exploit these relations even better.

Suppose we just did the n-th time step. We used relation (4.6) and unfortunately we discovered that our Δt_n was too large. Now we reject the step and we want to guess a new step size Δt such that the error $\epsilon_{n,i}$ is reduced and is lower than $\epsilon_{n,\min}$ everywhere. We need to find how the error depends on the step length Δt. Its Taylor expansion up to the first order in Δt gives: $\epsilon_{n,i}(\Delta t) \approx \varepsilon_{n,i}\Delta t$, where $\varepsilon_{n,i}$ is the error rate (see also Eq. (4.3)). We can calculate the maximum error rate as:

$$\varepsilon_{n,\max} = \max\left\{\varepsilon_{n,i}\right\}_i = \max\left\{\epsilon_{n,i}\right\}_i / \Delta t_n.$$

In this way we know that $\varepsilon_{n,\max}\,\Delta t$ would be the maximum error across all positions i, if the step size was Δt. The solution now is evidently quite simple: we want $\varepsilon_{n,\max}\Delta t < \epsilon_{n,\min}$, therefore we redo step n using:

$$\Delta t_{n,\text{new}} = \frac{\epsilon_{n,\min}}{\varepsilon_{n,\max}}.$$

This formula can be used not only when a step is rejected, but more widely to obtain a guess for the next step size. A good idea would be to take:

$$\Delta t_{n+1} = R\,\frac{\epsilon_{n,\min}}{\varepsilon_{n,\max}}. \tag{4.7}$$

R is a “safety factor” between 0 and 1 and controls the probability that the next time step will be accepted for the guessed step size: if $R \ll 1$, then this probability will be high, if $R \approx 1$, the probability will be low.

A final observation should be made. The Euler method does not preserve the magnitude of $\vec{m}$. Therefore we should take care of normalising it manually before proceding to the next step.

4.2.2 The Runge-Kutta methods

The Euler algorithm is referred to as a first order method, because it is accurate up to the first order in Δt: with this we mean that the *local* error associated with each time-step is $\mathcal{O}((\Delta t)^2)$. The method was derived in the previous section starting from a Taylor expansion of the unknown exact solution $\vec{m}(t)$. A second order method can be derived in a similar fashion. This time we keep also the second order term in the expansion:

$$\vec{m}(\vec{r}, t_{n+1}) \approx \vec{m}(\vec{r}, t_n) + \Delta t\, \vec{m}'(\vec{r}, t_n) + \frac{1}{2}(\Delta t)^2\, \vec{m}''(\vec{r}, t_n).$$

$\vec{m}'$ can be calculated using the LL equation, but how are we going to calculate the second derivative $\vec{m}''(\vec{r}, t_n)$? We could take, for example, $\vec{m}''(\vec{r}, t_n) = 2(\vec{m}'(\vec{r}, t_n + \Delta t/2) - \vec{m}'(\vec{r}, t_n))/\Delta t$. Substituting this into the former equation:

$$\vec{m}(\vec{r}, t_{n+1}) \approx \vec{m}(\vec{r}, t_n) + \Delta t\, \vec{m}'(\vec{r}, t_n + \Delta t/2).$$

This formula suggests the following approach:

- from $\vec{m}_n$ we calculate the effective field $\vec{H}_n$ and we substitute it in the LL equation to obtain $\vec{m}'_n$;
- we perform an Euler step to the middle of the time interval: $\vec{m}_{\frac{1}{2},n} = \vec{m}_n + \vec{m}'_n\, \Delta t/2$;
- from $\vec{m}_{\frac{1}{2},n}$ we calculate the effective field and use the LL equation to obtain $\vec{m}'_{\frac{1}{2},n}$;
- we perform an Euler step starting again from t_n, but using — this time — the derivative calculated in the middle of the time interval: $\vec{m}_{n+1} = \vec{m}_n + \vec{m}'_{\frac{1}{2},n}\, \Delta t$;
- iterate until convergence is reached.

This is the so called midpoint method. Note that the value of the magnetisation in the middle of the time interval is used only to calculate the derivative $\vec{m}'_{\frac{1}{2},n}$ and then it is simply discarded. The truncation error associated with each time-step is $\mathcal{O}((\Delta t)^3)$, but we have to pay a price for this greater accuracy: for each step the number of evaluations of $\vec{m}'$ is doubled.

Other algorithms with even higher order exist and can be derived systematically using a well defined procedure. These algorithms are referred as Runge-Kutta (RK) methods and are widely used for time integration. The algebraic calculations involved in the derivation of Runge-Kutta methods become rapidly lengthy and tedious as the required order of the method increases. The derivation of the second order Runge-Kutta methods could be instructive, because it shows the main ideas behind the procedure, still being quite easy. We will not face such a calculation, which can be found elsewhere [39]. We only mention that the Euler method turns out to be the unique first order Runge-Kutta method and that many different n-th order methods exist for $n > 1$. The midpoint method actually belongs to the class of second order Runge-Kutta methods.

It is important to note that to a higher order corresponds a higher number of evaluations of f (the RHS of the LL equation) and hence of the effective field, which is the most expensive computation in micromagnetic simulations in terms of time. However, higher order methods usually allow to choose bigger step lengths to obtain the same required accuracy. These two effects balance in a non trivial way, so that it depends on the particular considered problem if a higher order method will perform better or not. It is commonly well accepted that a fourth order Runge-Kutta method gives a good compromise between number of RHS evaluations (just 4) and obtained accuracy. We emphasise, however, that these are only provisional thoughts. We did not implement any Runge-Kutta time integrator in our own micromagnetic simulation package *Nmag*, and consequently we cannot formulate any precise statement about the relation between the number of RHS evaluations and the accuracy of the time integration. Runge-Kutta time integrators, however, have been implemented in other micromagnetic simulation packages such as OOMMF [37] and $\mathrm{M}^3\mathrm{S}$ [40], leading to significant performance improvements with respect to the Euler time integrator [41] (it is worth to notice, however, that such improvements depend much on the required accuracy [42]).

The step-length adjustment for Runge-Kutta algorithms can be implemented with the so called step doubling: time is advanced from t to $t + \Delta t$ in two different ways: firstly, the two-step evolution $\vec{m}(t) \to \vec{m}(t + \Delta t/2) \to \vec{m}(t + \Delta t)$ is performed; then the same evolution is performed using one single step $\vec{m}(t) \to \vec{m}(t + \Delta t)$. The difference between values obtained in these two different ways gives an estimate of the local truncation error and can be used to accept/reject the move and to adjust the time-step length. This technique requires an additional computational cost: every two Runge-Kutta steps (8 function evaluations, for a fourth order RK) we need to do an extra step, which requires 3 more function evaluations (since it shares the starting point). The overhead is thus a factor $11/8 = 1.375$.

A better technique for step length adjustment is provided by the so called “embedded Runge-Kutta formulas” [38]. These algorithms are based on the fact that the same set of function evaluations can be used to obtain two Runge-Kutta methods of different order. The difference between the results given by these two algorithms can then be used to calculate an estimate of the truncation error. The most popular of these methods was invented by Fehlberg and combines six function evaluations to obtain both a fifth order and a fourth order Runge-Kutta method.

4.2.3 Other methods

We gave a very small view on the wide world of numerical integration methods. We have to mention that other very interesting approaches exist. Indeed, in the previous sections we considered only single-step algorithms, so called because, even if they may calculate and store the time derivative of $\vec{m}$ several times per step, they completely get rid of such information when passing to the next steps. The time-stepping of these algorithms could be represented by a simple function mapping $\vec{m}_n$ onto $\vec{m}_{n+1}$. Multi-step methods, on the other hand, use the "recent history" of the system to compute the new configuration. This means that, in order to compute the next step, part of the information which was used in the previous steps is reused. The popular Adams-Bashforth-Moulton algorithms belong to the category of predictor-corrector algorithms, which is an important class of multi-step methods. These methods are rather complex to implement and require a considerable bookeeping.

4.2.4 Semi-analytical methods

When the effective field is constant in time, the LLG equation (2.3) is known to admit a simple analytical solution, which can be found by expressing it in spherical coordinates or by projecting it along the direction of the applied field and on the plane orthogonal to it, as shown in Appx B. One is then tempted to exploit such an analytical equation and use it to improve an already existing numerical integration scheme, such as the Euler method of Sec. 4.2.1. The resulting semi-analytical integration scheme may help — for example — to overcome the problem of respecting the constraint of constant norm for the magnetisation, Eq. (2.4). Indeed, since the analytical solution does fulfil exactly such constraint, it may be used to replace the Euler step, Eq. (4.2). This idea has attracted quite some researchers in the field of computational micromagnetics [43, 44, 45], including us. After implementing the Euler method in *Nmag*, we worked on a semi-analytical method very similar to the one presented in Ref. [45], which we derived independently. We found, however, that in most practical cases, such an algorithm does not lead to significant performance improvements with respect to the simple Euler algorithm of Sec. 4.2.1 and results in analogous time step sizes.

We understood the result in the following way. Whether the semi-analytical approach will work well or not, depends quite crucially on how the effective field changes with the magnetisation: if the effective field is constant in time, then it is reasonable to expect the semi-analytical algorithm to outperform any other algorithms since — in principle — it would need just one step to reach convergence. In general, we expect the semi-analytical approach to work well when the effective field changes slowly with the magnetisation. Unfortunately, the contribution that the exchange field gives to the effective field has the form $\nabla^2\vec{m}$ (see Eq. (2.11)) and thus typically varies as quickly as the magnetisation itself. As a consequence, the corresponding dynamics is often rather different with respect to the one described by the analytical solution, Eq. (B.11). Discouraged by such findings, we did not invest more time to look into semi-analytical approaches to integrate the LLG equation. It is worth to mention, however, that there are researchers who have been working more extensively on the method and on improving it [46].

4.2.5 The backward Euler and the Sundials package

So far we only considered explicit methods while also implicit methods exist. We explain briefly the difference between explicit and implicit methods starting from the formula: $\vec{m}_{n+1,i} = \vec{m}_{n,i} + \vec{m}'_{n,i}\Delta t_n$. This is the Euler algorithm and was explained extensively in Sec. 4.2.1. Actually this should be called explicit (or forward) Euler method, since also an implicit version of the same formula exists: $\vec{m}_{n+1,i} = \vec{m}_{n,i} + \vec{m}'_{n+1,i}\Delta t_n$. With the forward Euler method we can calculate immediately the next configuration $\vec{m}_{n+1,i}$ using the time derivative $\vec{m}'_{n,i}$, which can be obtained directly putting $\vec{m}_{n,i}$ inside the LL equation. With the implicit (or backward) Euler method one needs to use more complex techniques, since the derivative $\vec{m}'_{n+1,i}$ cannot be computed directly: functional iteration or the Newton's method need to be used. This means that a step in the implicit scheme will generally take much more time than a step in the explicit scheme. On the other hand, it is known that *stiff* problems can be hard to solve with explicit methods, due to their prohibitively small time step requirements. Implicit methods, such as the backward Euler, can provide much better performance in such cases (larger time steps).

This is the reason why for the time integration in *Nmag* we have chosen to use an external code, the CVODE library provided by the Sundials package [47]. The CVODE library provides the user with two families of algorithms for time integration: the Adams-Moulton formulas and — for stiff problems — the Backward Differentiation

Formulas (BDFs) [48]. Suess *et al.* [49] presented a detailed study of the performances of the Adams and the BDF methods as implemented in the CVODE library, when applied to two different micromagnetic problems within the scope of the finite element method. They studied a single-material magnetic thin film, following the specification of the fourth μMAG standard problem [50] and they also investigated a granular structure with irregular boundary surface. Their findings suggest that, while different algorithms perform differently depending on the setup of the problem, on the particular mesh and on the required accuracy, a BDF algorithm with maximum integration order set to 2 ($K_1 = 2$, see “mathematical considerations” in Ref. [48]) and with preconditioning (in order to solve the implicit BDF formula) leads to optimal performance, when compared against the Adams method and against BDF method without preconditioning or with integration order greater than 2.

4.2.6 Summary

In this section we gave a quick review of some of the numerical methods which were used in the computational studies presented in this thesis. We briefly introduced some of the ideas at the base of the finite element method and gave a quick overview on some time-integration techniques which are often used for micromagnetics. We focused mainly on the Euler method, which was implemented initially while working on the project for this thesis. At present, however, our simulation software, *Nmag*, uses the CVODE package for carrying out the time integration of the LLG equation [47].

Chapter 5

Nmag, a flexible micromagnetic simulation software

All the numerical results presented in this thesis have been obtained using *Nmag*, the FEM-based micromagnetic simulation package which has been developed by our group in Southampton and has been released as open source [51]. At present, *Nmag* has been used in our own works to study effects such as the anisotropic magnetoresistance in nano-rings [52], the demagnetising field of quasi-periodic nanostructures [53], exchange springs systems [54] spin transfer torque effects [55, 56] and has been recently employed by other independent groups for their own studies [57, 58].

For the preparation of this thesis we have not just used *Nmag*, but we have also devoted considerable time in developing and improving it. In this chapter we explain the reason why we embarked on the development of a new software for micromagnetic simulations, rather than using an already existing system such as OOMMF [37] or Magpar [59]. We discuss the main goals and characteristics of *Nmag* and explain how we contributed to it.

5.1 Introduction

In recent times researchers are showing an increasing interest in the coupling between magnetism and other phenomena, such as spin transport, heat generation and conduction, electromagnetic wave generation and absorption, etc. This trend is generating a considerable demand for flexible simulation tools, which have multiphysics capabilities, meaning that they can take into account different types of physics. While there are a number of commercial and free software packages for micromagnetic modelling

[37, 59, 60], practically all of them are frameworks highly specialised in micromagnetics, which need ad-hoc extensions in order to introduce new fields or modify the equation of motion. These tools typically rely on a rigid scheme for performing micromagnetic simulations, which is depicted in Fig. 5.1-a. When using such tools, the user has to

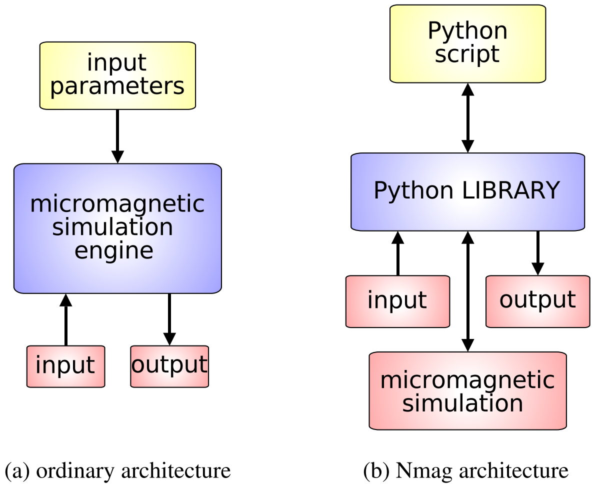

(a) ordinary architecture (b) Nmag architecture

Figure 5.1: Different approaches to micromagnetic simulations. (a) traditional approach, where input parameters (a set of numbers) are provided in one or more files. (b) alternative approach, where the simulation capabilities are collected in a library for a modern and powerful scripting language and the simulation is carried out just by using the library.

provide one or more files, containing a set of input parameters. These input parameters are essentially a bunch of numbers describing the material (saturation magnetisation M_{sat}, exchange coupling constant A, etc.), the initial magnetisation configuration, the range for the applied magnetic field (in the case of hysteresis loop). When launched, the simulation tool reads the parameters and runs the simulation, writing the results in a set of output files. It does all this following a rigid predetermined order of execution and may thus remind how a vending machine works: select the drink, the amount of sugar, press the button, get the coffee. This approach is simple and often effective enough. In many other situations, however, it is desirable to have more flexibility, in particular when studying new magnetic nanostructures and multiphysics scenarios.

With *Nmag* we propose an alternative approach (see Fig. 5.1-b), where micromagnetism is just one applications of a generalised framework and extensions to the software (such as adding a new field or modifying the equation of motion) can be made without recompiling it. The central idea is to embed the simulation capabilities inside a library for a scripting language. To run a simulation, then, the user has to write a small script[1], rather than providing a list of input parameters. This approach has a number of advantages in terms of flexibility:

- it is the user who decides what to do and when: the order of execution is determined by how the user writes the script. He can do a time integration with the method `advance_time`, perform an hysteresis loop with `hysteresis`, save the data with `save_data`. The user decides what to do by calling the appropriate function in the desired order;
- the micromagnetic simulation library can be used together with other libraries. For example, if a micromagnetic simulation is carried out in order to determine the amplitude A of the magnetisation response to a given stimulus s, then an optimisation library may be used in order to find which stimulus s_{max} maximises the amplitude A.
- new capabilities can be added easily from within the scripting language;
- there is also an advantage in terms of clarity. A small script is generally clearer that a file containing just a list of input parameters.

The popular software OOMMF uses an approach which may appear to be very similar to the one we have just described: it requires the user to provide a Tcl script [61] in order to carry out a micromagnetic simulation. At present, however, OOMMF uses Tcl just to collect the input parameters and does not give to the user control over the order of execution. It thus sticks to the traditional approach of Fig. 5.1-a, with some additional advantages, such as offering the possibility of setting an arbitrary initial magnetisation. OOMMF does not allow the user to run more than one simulation per script [62].

5.2 Implementation details

Nmag consists of two parts: a FEM classical field framework, which provides basic functionality to define scalar, vector and tensor fields and to operate on them, and a top layer which uses this framework in order to provide an environment for running micromagnetic simulations.

---

[1] A script is just a program which can be read and executed on the fly, without requiring an intermediate translation into machine code, in contrast to what happens for C or Fortran.

The bottom layer implements finite element method (FEM) discretisation to arbitrary order of the shape functions and is the part of the software which actually does the computationally intensive work. It is written in OCaml [63], a fast functional programming language, and uses a number of well known optimised external libraries to carry out vector manipulation at the lowest level. In particular, MPICH2 [64] is used in order to distribute data and computation over multiple machines, Petsc [65] is used for vector and matrix manipulation, Sundials [47] is used for the time integration of the Landau-Lifshitz equation.

Such capabilities are exploited by the top layer, which implements the micromagnetic simulation environment and is written in Python [66], a modern scripting language which is powerful and still easy to learn and use. It is worth to stress once more that the full micromagnetic calculation is just an extension to the underlying general purpose FEM library, which we call *Nsim*. This means, in particular, that the Landau Lifshitz equation, the computations of the exchange and the demagnetising field are all specified in the top Python layer. This feature is particularly desirable in multiphysics scenarios, since extensions to the micromagnetic model can be made by writing Python code.

Being based on finite element, *Nmag* requires an unstructured mesh of the ferromagnetic sample which is to be simulated, such as the one shown in Fig. 5.3. The mesh specifies how the volume of the body is subdivided into elements of tetrahedral shape. To obtain such a decomposition, external meshing programs can be used[2]: in this thesis we used Netgen [34]. In summary, to run a simulation the user has to provide a mesh and a Python script, such as the one shown in Fig. 5.4. The simulation can be run by putting the script and the mesh file in the same directory and executing `nsim script.py` from the command prompt.

It has been said before that *Nmag* uses MPICH2 to distribute data and computation over multiple machines. Considering the architecture of the program, where the user can influence the order of execution of the simulations, this is not a trivial task. The model we adopted in order to deal with such a task is depicted in Fig. 5.2. We call it the master-slave approach. The nodes involved in the computation are indeed split into two groups: the master node, which does actually execute the Python script, and the slave nodes, which wait for the master node to send instructions and give an on-demand help with the computation. Running the script only on a single machine

---

[2] Actually *Nmag* provides its own mesher, *Nmesh*. For large three dimensional meshes, however, there are free (and commercial) alternative packages which offer considerably better performance.

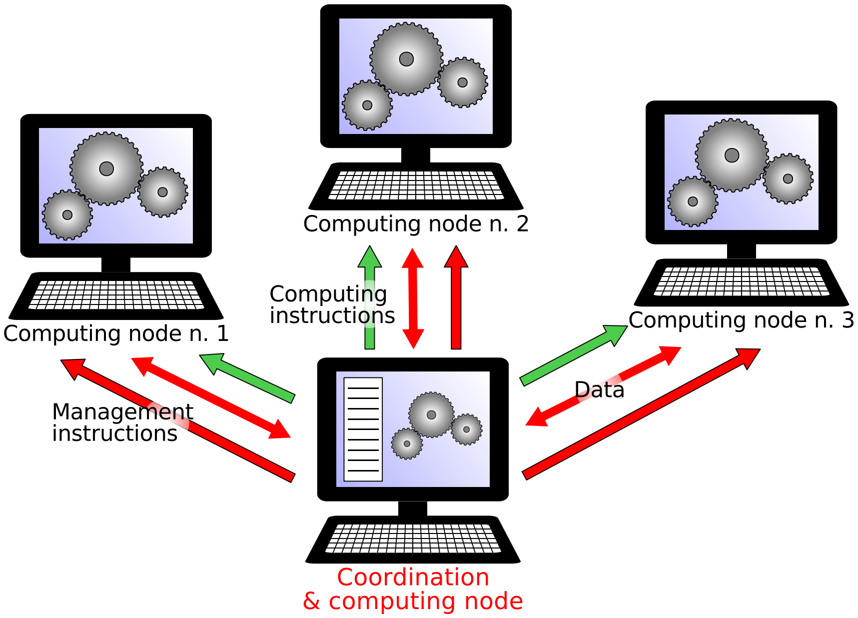

Figure 5.2: The approach to parallelisation employed by *Nmag*: One of the nodes acts as "master", the others act as "slaves". The master node executes the Python script, asking for the help of the slave nodes only when dealing with computationally intensive tasks. This approach guarantees that a script written for running on one machine, can run also on multiple machines without requiring any special modifications.

and using the others as computing nodes has two important advantages with respect to a more traditional approach where all the nodes are running simultaneously the same program and are thus treated at the same level. First, this approach removes conflicts in input/output operations. Such a conflict may arise, for example, when the user creates a file. Indeed, if the script is running on multiple machines, each of those will try to concurrently create the same file. Special precautions would then be needed to avoid the problem and this is something we cannot really expect from the average user. A more technical reason for using the master-slave approach, is connected with the memory management of OCaml. OCaml uses garbage collection to manage memory allocation and, consequently, we may expect some randomness in the way memory is requested and handed back to the system. This becomes a major problem when destroying parallel vectors and resources: destructions of parallel resources need perfect synchronisation between the nodes involved in the computation, while the garbage collectors of different nodes may lead to asynchronous destruction of the distributed parts of vectors and matrices.

An accurate and complete description of *Nmag* goes beyond the scope of this chapter. A paper going more into the technical details of the package is in preparation. A short summary of the main features of *Nmag* and the algorithms used for the different parts of the micromagnetic calculations is provided below:

- Finite Element Method discretisation;
- vector and matrix management through Petsc [65] and MPI [64];
- demagnetising field calculated using the hybrid FEM/BEM approach [30, 29];
- time integration through a backward preconditioned time integrator using Sundials [47].

5.3 Example 1: hysteresis loop with *Nmag*

In this and the next section we provide two example scripts in order to show how *Nmag* is used in practice. We first give an example of hysteresis loop computation. We consider a bar made of Permalloy with size 30 × 30 × 100 nm and apply the field in the (1, 1, 1) direction. The mesh (Fig. 5.3) is obtained using Netgen and is contained inside a file with name `bar.nmesh.h5`, which must be placed in the same directory containing the script. The script is shown in Fig. 5.4. Here we comment it briefly line by line.

- *Lines 2-3:* we specify that we want to use *Nmag*, the library to run micromagnetic simulations. All the functionality provided by this library will be accessible in the following lines of the script by using the prefix “`nmag.`”, such as in `nmag.MagMaterial` or `nmag.Simulation`. In line 3 we indicate that we want to access the objects `SI` and `at` directly, without any prefix. Indeed, the object `SI` will be used frequently in the script to associate physical dimensions to numbers. For example, to provide a length we could write `SI(5, "m")` (for 5 meters), to provide a velocity `SI(7, "m/s")` (7 meters per second).
- *Lines 7-8:* we define a new material corresponding to Permalloy. We give it the name “`Py`” and associate saturation magnetisation $M_{\text{sat}} = 0.86 \times 10^6\,\text{A/m}$ and exchange coupling constant $A = 13 \times 10^{-12}\,\text{J/m}$.
- *Line 10:* we define a new simulation object `s`. Its role will become clearer in the following lines.

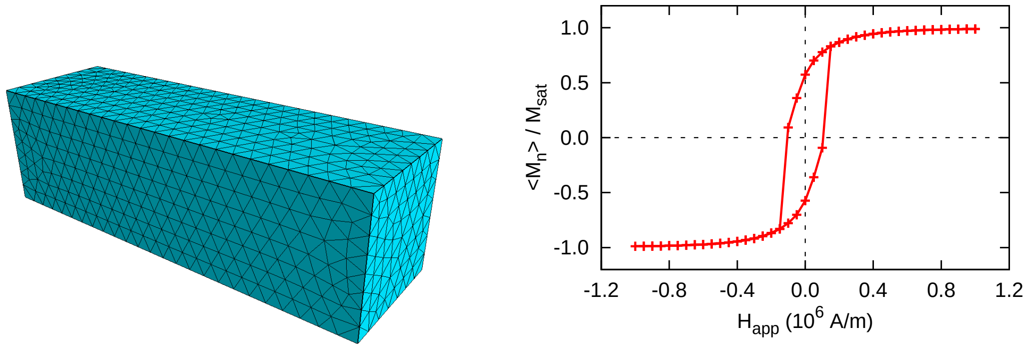

Figure 5.3: *On the left:* Mesh of a bar with size 30 × 30 × 100 nm. *On the right:* hysteresis loop obtained by applying a field in the $\vec{n} = (1, 1, 1)$ direction with intensity going from 10^6 A/m to -10^6 A/m. Note that $M_n = \vec{M} \cdot \vec{n}$ and $\langle M_n \rangle$ is the spatial average of M_n.

```python
# Import the Python library for doing micromagnetic simulations
import nmag
from nmag import SI, at

# Create a new material with appropriate name, saturation magnetisation
# and exchange coupling constant
mat_Py = nmag.MagMaterial(name=’Py’, Ms=SI(0.86e6, ’A/m’),
                          exchange_coupling=SI(13e-12, ’J/m’))

s = nmag.Simulation() # Create a new simulation object

# Load the mesh and associate materials to its regions
s.load_mesh(’bar.nmesh.h5’, [(’region1’, mat_Py)], unit_length=SI(1e-9, ’m’))

s.set_m([1, 1, 1]) # Set the initial magnetisation

# Define a list of applied fields for which we want to run the hysteresis loop
Hs = nmag.vector_set(direction=[1, 1, 1],
                     norm_list=[1.0, 0.95, [], -1.0, -0.95, [], 1.0],
                     units=1e6*SI(’A/m’))

# Run the hysteresis loop. Save averages of fields at convergence of each stage
s.hysteresis(Hs, save=[(’averages’, at(’convergence’))])
```

Figure 5.4: Example showing how to setup an hysteresis loop with *Nmag*. The simulation setup requires just 23 lines of Python code, of which 12 lines are blank or used for comments.

- *Line 13:* the mesh is loaded from the file "`bar.nmesh.h5`" and is associated to the simulation object `s`. A mesh can, in general, have many regions: this depends on the way it was created. One may, for example, split the bar of Fig. 5.3 into two or more regions and associate to each region a different material. In the current example we have just one region and one material. We use `[('region1', mat_Py)]` to specify that we call the first and unique region with the name "`region1`" and that this region is filled with Permalloy. Finally, with `unit_length=SI(1e-9, 'm')` we indicate that the mesh is expressed in units of nanometers, i.e. one in the coordinate system of the mesh means one nanometer.

- *Line 15:* we set the magnetisation along the direction [1, 1, 1]. Note that we could use the same method `set_m` to set the magnetisation from a Python function.

- *Lines 18-20:* we create, in `Hs`, a list of values for the applied field. The hysteresis loop will be carried out by setting the applied field and running a simulation for each of these values (this simulation is also called "stage" of the hysteresis loop). These values are all pointing in the direction `[1, 1, 1]` and have norms going from $1.0u$ to $-1.0u$ in steps of $0.05u$, where u is the unit, 10^6 A/m.

- *Line 23:* we run the hysteresis loop and save the averages of all the fields at convergence of each stage. Here we finally see what the `at` symbol, which was imported in line 3, is used for.

The simulation can be run by entering `nsim script.py` at the command prompt. The data can be extracted then with a dedicated tool, `ncol`. The final hysteresis loop is shown in Fig. 5.3 (right).

5.4 Example 2: proposal for a new standard problem

Introduction

After developing a software package to perform simulations, it is important to assess its reliability by running a number of tests and by executing comparisons against well known solutions. This is the reason why researchers in computational micromagnetism agreed on the formulation of a set of standard problems, whose specifics are now published online [50], together with the solutions submitted by several research groups all over the world. Such an approach helps mutual progress and gives also an opportunity to compare accuracy and performance of different simulations packages and different numerical methods. Unfortunately, the set of standard problems is currently constituted only by four problems and all of them are single-physics problems, meaning that they take into account only standard micromagnetic effects. Considering the recent research trends in micromagnetics, we think it is important to introduce new standard problems, where multiphysics scenarios are studied. For this reason we collaborated with researchers from the University of Hamburg (Germany) and from the IBM Zürich Research Laboratory (Switzerland) to formulate a standard problem including spin transfer torque effects through the Zhang-Li extension to the Landau-Lifshitz-Gilbert equation. The collaboration resulted in a paper [67], which collects numerical result from four different software packages and compares them with the approximated analytical solution. We contributed to this work by helping in the formulation of the standard problem and by running it with *Nmag*.

Problem definition

We consider a thin film with cuboid geometry and size 100 × 100 × 10 nm. We use material parameters similar to Permalloy, with the exception of the damping parameter α: the saturation magnetisation is $M_{\text{sat}} = 8 \times 10^5\,\text{A/m}$, the exchange coupling constant is $A = 13 \times 10^{-12}\,\text{J/m}$ and the gyromagnetic ratio is $\gamma = 2.211 \times 10^5\,\text{m/(As)}$.

The simulation consists of two sub-simulations. In the first part we are not interested in the dynamics of the system: we just relax the system, such that a precise initial magnetisation is obtained. Indeed, we want to get to the equilibrium state where the magnetisation develops a vortex in the center of the film. In the second part, we apply a current density and study how the vortex dynamically reacts to it.

The first sub-simulation uses the following expression to set up the initial magnetisation:

$$\vec{M}(\vec{r}) = M_{\text{sat}} \frac{\vec{u}(\vec{r})}{\|\vec{u}(\vec{r})\|}, \qquad \vec{u}(\vec{r}) = (-(y - y_0),\, x - x_0,\, R)\,,$$

where $\vec{r} = (x,\, y,\, z)$ is the position in space and $\vec{r}_0 = (x_0,\, y_0,\, z_0) = (50\,\text{nm},\, 50\,\text{nm},\, 5\,\text{nm})$ is the center of the film. $R = 40\,\text{nm}$ is a constant used to make sure that the norm of $\vec{u}$ is always positive. Its sign determines the final chirality of the vortex. This initial magnetisation is relaxed using a damping constant $\alpha = 1$ to reach convergence quickly. The relaxation proceeds until the following convergence criterion is satisfied:

$$\max_{\vec{r} \in \mathcal{V}} \left\| \frac{1}{M_{\text{sat}}} \frac{\mathrm{d}\vec{M}(\vec{r})}{\mathrm{d}t} \right\| \leq 0.01\,\text{rad/ns}, \tag{5.1}$$

where $\mathcal{V}$ is the region of space occupied by the cuboid. The magnetisation is then saved to file.

In the second sub-simulation, the equilibrium magnetisation obtained in the first sub-simulation is loaded from file and is used as the initial configuration. A fully polarised ($P = 1$) current with density $j = 10^{12}\,\mathrm{A/m^2}$ is instantaneously applied in the positive x direction. The current density is homogeneous in space and constant in time. The damping constant is set to $\alpha = 0.1$ and the degree of non adiabadicity is set to $\xi = 0.05$. These parameters are not realistic for Permalloy, but produce enhanced non-adiabatic effects, helping to identify possible errors in the implementation of the fourth term in the right hand side of Eq. (3.13). Indeed, using the realistic values $\alpha = 0.01$ and $\xi = 0.01$ would lead to negligible non adiabatic effects, thus weakening the falsification properties of the standard problem [67]. The behaviour of the spatially averaged magnetisation reflects the dynamics of the vortex and is hence studied as a function of time.

The script

The code is discussed below, line by line.

- *Lines 2-4*: we import the micromagnetic library *Nmag*, together with other Python libraries. We import explicitly `SI`, `at`, `every` and `degrees_per_ns`. We will see later how these symbols are used in the script.
- *Lines 7-18*: we create the material and the simulation object, we load the mesh, associate the material with it and return the simulation object. This is very similar to what discussed in Sec. 5.3 with two differences. First, we are doing all these operations inside a function. Indeed, the standard problem requires us to run two simulations of the same system. We then put the material definition and the simulation setup inside a function so that we can re-use this code twice. Second, we are providing four more parameters to `MagMaterial`: the gyromagnetic ratio γ and the damping parameter α for the Landau-Lifshitz equation (when they are not provided, the values $\alpha = 0.5$ and $\gamma = 0.2211 \times 10^6\mathrm{m/As}$ are used instead), the spin polarisation P and the parameter ξ for Permalloy (see Eq. (3.12)).
- *Lines 22-33*: we run the preliminary sub-problem to find the initial magnetisation for the second sub-problem. We create the simulation object and load the mesh by calling the function `my_simulation` that we defined previously in the script. We set the magnetisation (line 29) using the function `initial_m` defined in lines 24-26. We then run a simulation and relax the system to find the equilibrium magnetisation. The simulation stops when the convergence criterion in Eq. (5.1)

```python
# We model a bar 100 nm x 100 nm x 10 nm where a vortex sits in the center.
import os, nmag
from nmag import SI, every, at
from nsim.si_units.si import degrees_per_ns

# This is an helper function to create the simulation object and load the mesh
def my_simulation(name, damping, P=0.0, xi=0.0):
  mat_Py = nmag.MagMaterial(name="Py",
                            Ms=SI(0.86e6,"A/m"),
                            exchange_coupling=SI(13.0e-12, "J/m"),
                            llg_gamma_G=SI(0.2211e6, "m/A s"),
                            llg_polarisation=P,
                            llg_xi=xi,
                            llg_damping=damping)

  sim = nmag.Simulation(name)
  sim.load_mesh("pyfilm.nmesh.h5", [("Py", mat_Py)], unit_length=SI(1e-9,"m"))
  return sim

# If the initial magnetisation has not been calculated and saved into
# the file "vortex_m.h5", then do it now, by running a preliminary simulation!
relaxed_m_file = "vortex_m.h5"
if not os.path.exists(relaxed_m_file):
  def initial_m(p): # define an initial magnetisation which is likely to relax
    x, y, z = p     # into the vortex state
    return [-(y-50.0e-9), (x-50.0e-9), 40.0e-9]

  prelim = my_simulation(name="preliminary", damping=1.0)
  prelim.set_m(initial_m)
  prelim.set_params(stopping_dm_dt=1.8*degrees_per_ns)
  prelim.relax(save=[('fields', at('step', 0) | at('stage_end'))])
  prelim.save_restart_file(relaxed_m_file)
  del prelim        # delete the preliminary simulation

# Now we deal with the second simulation: the one with the current!
sim = my_simulation(name="simulation", damping=0.1, P=1.0, xi=0.05)
sim.load_m_from_h5file(relaxed_m_file)
sim.set_current_density([1e12, 0, 0], unit=SI("A/m^2"))
sim.set_params(stopping_dm_dt=0.0) # WE decide when the simulation should stop!
sim.relax(save=[('fields', at('stage_end') | every('time', SI(1.0e-9, "s"))),
                ('averages', every('time', SI(0.05e-9, "s")) | at('stage_end'))],
          do  =[('exit', at("time", SI(10e-9, "s")))])
```

Figure 5.5: The script used to run the spin transfer torque standard problem with nmag. The script is discussed line by line in the text.

is met (0.01 radians per nanosecond = 1.8 degrees per nanosecond). We save all the fields before and after the relaxation, so that we can obtain the pictures in Fig. 5.6 and in Fig. 5.7. After the relaxation we save the magnetisation configuration to file, so that it can be re-loaded and used in the second part of the script. Notice that all these commands are executed only if the file `vortex_m.h5` does not exist (see line 22-23). If such a file exists, then we assume that the first sub-problem has already been executed and proceed straight to the second sub-problem.

- *Lines 35-42*: We use again the function `my_simulation` to setup a second simulation. We then load the magnetisation from the file `vortex_m.h5`, set a current density with intensity 10^{12} A/m along the x axis and set the parameter `stopping_dm_dt` to 0 degrees per nanosecond. With this choice the convergence criterion will never be met. We finally run the simulation, saving all the fields every 1 nanosecond and at the end of the simulation. The field averages are saved every 50 picoseconds and at the end of the simulation. The simulation is forced to last for a total of 10 nanoseconds. Note how the time constructs (`at(...)`, `every(...)`) can be combined together: the operator `|` (or) is used to specify that "something" should be saved/done when at least one of the two given conditions is met. The operator `&` (and) specifies that "something" should be saved/done when both the two conditions are met (it is not used in this example). The thing to save/do is specified via a string, such as `fields`, `averages`, `exit`. However, the user can also provide an arbitrary function to be executed when the time specification is matched, resulting in a considerable flexibility.

The components of the average magnetisation are plotted as functions of time for the second sub-problem. The decaying sinusoidal behaviour of the three curves reflects the spiralling motion of the vortex [67], which is induced by the sudden application of the current.

5.5 Contributed extensions

Nmag has been designed and implemented by a team of people, including Hans Fangohr, Thomas Fischbacher, Matteo Franchin, Giuliano Bordignon, Andreas Knittel, Jaceck Generowicz, Michael Walter and James Kenny. Here we briefly list the work which was done on *Nmag* while working on the project for this thesis.

- we implemented the local exchange coupling to model ferrimagnetic materials

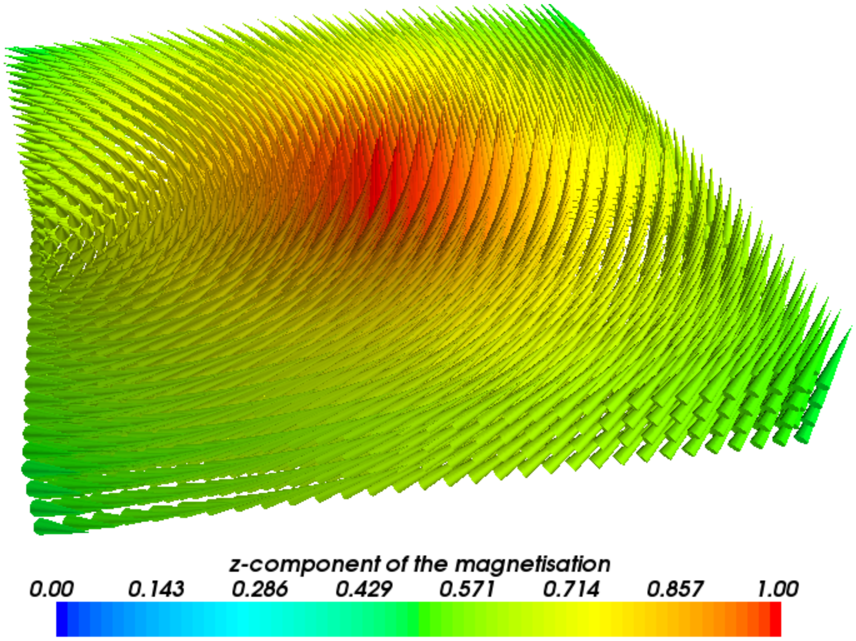

Figure 5.6: The magnetisation used as initial configuration for the first sub-simulation in the spin torque standard problem.

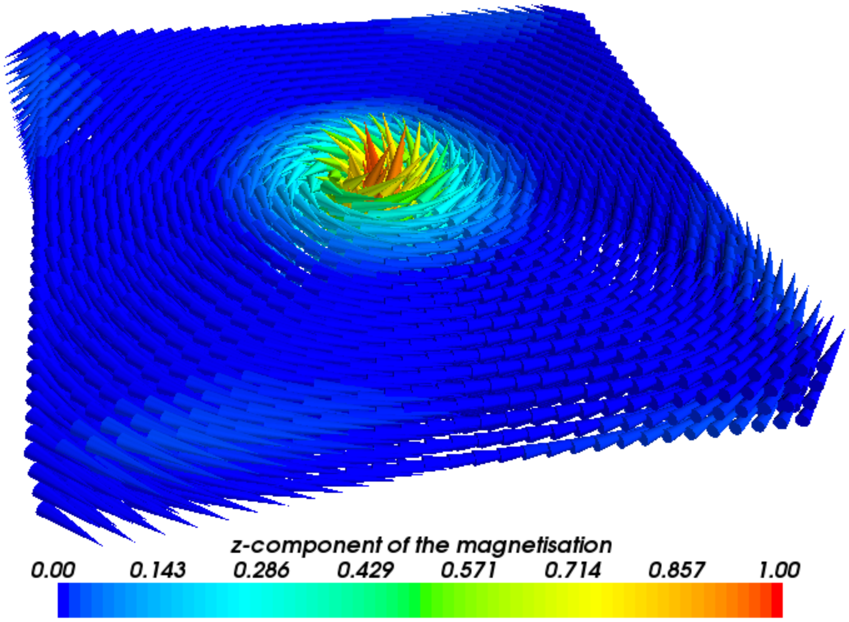

Figure 5.7: The magnetisation at the end of the preliminary sub-problem. This is the initial magnetisation used by the second sub-simulation. Notice that the magnetisation is everywhere in plane, except near the center of the film, where the vortex sits.

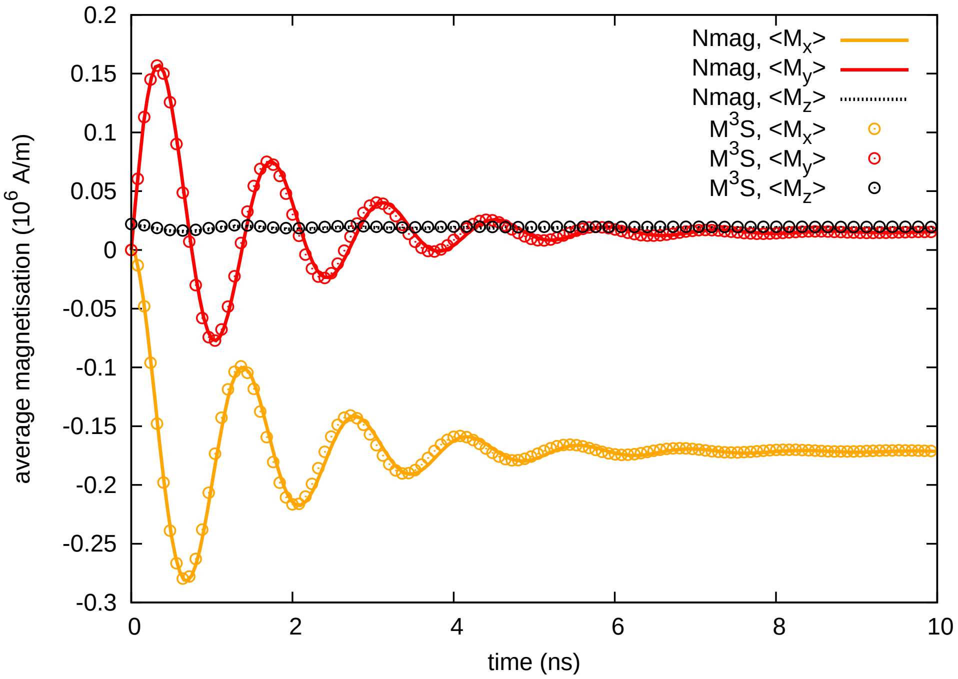

Figure 5.8: The plot shows the dynamic response of the average magnetisation to the applied current density for the second sub-part of the standard problem. The solid lines show the results obtained with the script discussed line-by-line in the text (*Nmag*). The unstructured mesh which was used consists of 4536 points, 19215 simplices and has edge lengths between 1.66 and 4.71 nm. The circles show the results obtained with M^3S (a FD package [67]) and cell size $2 \times 2 \times 2$ nm.

and $DyFe_2$-YFe_2 multilayers. This work was necessary for studying the exchange spring systems of Ch. 6;

- we implemented the Zhang-Li extension to the Landau-Lifshitz-Gilbert equation in order to model spin transfer torque effects in the systems. This feature was necessary for the studies conducted in Ch. 6, 7 and 8;
- we contributed to the development of the Python interface of *Nmag*, focusing in particular on the `hysteresis` and `relax` commands and the logic behind the `at` and `every` constructs.
- we contributed to *Nmag*, by performing tests, fixing bugs and improving the performance of the package;
- we improved the build system so that researchers in other groups can quickly install *Nmag* on their computers. We also provided support to them.

- we wrote the documentation for *Nmag*, contributing to the manual which can be found online [68].

5.6 Summary

We have introduced the *Nmag* micromagnetic simulation package, explaining the motivations behind the creation of this new software and describing briefly its main features. We gave two examples of usage, including the corresponding source scripts and explaining them line-by-line. The first example shows how to set up an hysteresis loop, while the second shows how to produce the result for the recently published micromagnetic standard problem including the spin transfer torque.

Chapter 6

Exchange springs in multilayer systems

6.1 Magnetic exchange spring systems

Exchange spring systems are nanocomposites of ferromagnetic materials with high magnetic anisotropy (hard materials) and low magnetic anisotropy (soft materials), exchange coupled across the interfaces between the two phases. Realisations of such systems include the clustered structure (Fig. 6.1-a), where soft inclusions are randomly dispersed inside the hard phase, and the multilayer structure (Fig. 6.1-b), made of alternating hard and soft layers. In this thesis we discuss only multilayer structures (thin films or nanopillars), which have simpler geometry and are easier to study. In all their forms, exchange spring systems are characterised by the interplay between the magnetic properties of the hard and the soft phases. Quite in general, hard materials are characterised by a strong preference for the magnetisation to align along some preferred directions relative to the crystal lattice. On the other hand, in soft materials the magnetisation easily aligns with the external applied field. When hard and soft materials are put together in an exchange spring system, a peculiar physics emerges: the magnetisation of the soft material tries to follow the applied field, except near the hard-soft interfaces, where the hard-soft exchange coupling bounds its direction to the direction of the hard magnetisation. As a consequence, the magnetisation of the soft material responds to the applied field in a position-dependent way: it keeps a fixed direction at the interfaces, and twists towards the applied field in the bulk. The soft magnetisation here bends in a way which is proportional to the applied field. This resembles a mechanical torsion spring, thus comes the name “exchange spring”. Many

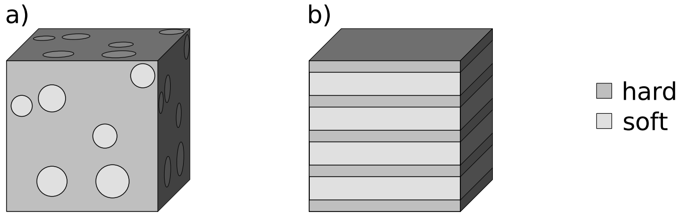

Figure 6.1: Exchange spring system in the form of a nanocomposite (a), where soft clusters are embedded into the hard phase, and in the form of a multilayer film (b), made of alternating soft and hard layers.

of the properties of such systems can be tuned by selecting suitable geometries and compositions. For example, the size of the soft regions is usually quite important, since a larger soft region usually corresponds to enhanced torsion of the soft magnetisation, as most of the soft material is far from the interfaces. On the other hand, if the soft material has a high exchange coupling constant, then it is harder to twist its magnetisation. The properties we have briefly presented so far make exchange spring systems promising candidates for many technological applications. Studies in the literature have suggested that they could be used to obtain high densities in storage media, while keeping acceptable writability and thermal stability [69]. They could also be used as high-performance permanent magnets [70] or to develop GMR (Giant Magneto Resistance) sensors [71].

We now discuss in more details how an exchange spring system reacts to an external applied field, giving a visualisation of the process in a simple case. We consider the system depicted in Fig. 6.2-a: a trilayer thin film made of one soft layer sandwiched between two hard layers. Suppose the initial configuration is the one shown in the part (a) of the figure: both the hard and soft magnetisations are pointing to the right. We apply an external field $\vec{H}_{\mathrm{app}}$ which is initially zero and then increases pointing to the left. The system initially does not change its configuration and continues to stick to the state shown in Fig. 6.2-a, even for non-zero values of the applied field, $\vec{H}_{\mathrm{app}}$. This behaviour can be explained in the following way: the magnetisation of the soft layer would like to align with the applied field, because a non-alignment has a cost in terms of energy. At the same time, however, the alignment breaking is contrasted by the soft-soft and the soft-hard exchange couplings, which prefer to keep the magnetisation of the soft layer parallel to the fixed magnetisation of the hard layer.[1] It turns out that the

---

[1] Remember that the strong anisotropy constrains the magnetisation to be fixed in the hard layers,

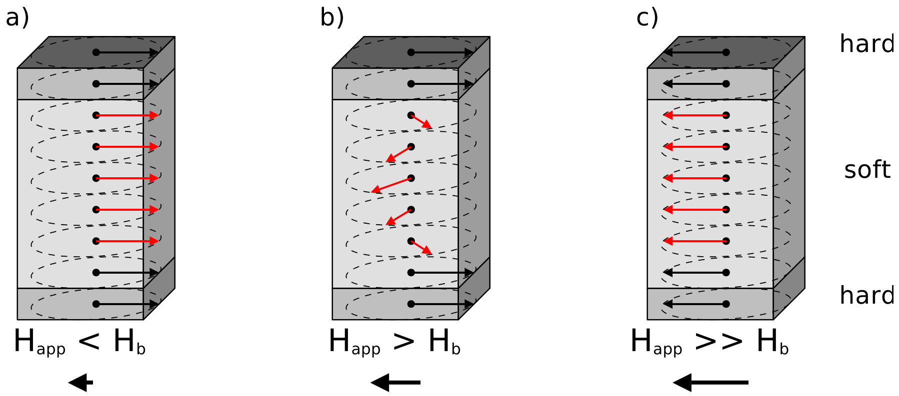

Figure 6.2: A simple example of exchange spring system: one layer of soft magnetic material sandwiched between two layers of hard material. The figure shows how the magnetisation reacts to different intensities of the applied field $\vec{H}_{\mathrm{app}}$.

balance of these effects favours the completely aligned state (a), unless the applied field exceeds a well determined threshold field H_{b}, the bending field. When this happens, the situation changes as shown in Fig. 6.2-b. The magnetisation of the soft material starts to bend near the center of the layer in a way which is somewhat proportional to the applied field, while at the boundaries it stays aligned with the magnetisation of the hard material, due to the strong exchange coupling. Finally, for fields large enough, also the magnetisation of the hard layers switches to follow $\vec{H}_{\mathrm{app}}$ and the resulting state of the system is the one shown in Fig. 6.2-c, a mirrored image of Fig. 6.2-a, with the magnetisations of all the layers pointing to the left. This intuitive description of the behaviour of a typical exchange spring system has been better justified with simple theoretical models [72]. We present an analytical study in the next section.

6.2 Analytical study of the static equilibrium configurations

In this section we present an analytical investigation which validates the rough intuitive picture given in the previous section. We study the trilayer thin film with a one dimensional model, thus neglecting the inhomogeneities of the magnetisation in the plane of the film. We assume that the magnetic anisotropy of the hard material is so strong, that the hard moments are — to a good approximation — rigidly pinned

---

at least for sufficiently small fields.

along an easy axis direction. We also assume that the exchange coupling between hard and soft moments is infinitely strong. These assumptions reduce the complexity of the system, since the hard layers can be taken into account just by imposing a constraint on the direction of the soft magnetisation at the soft layer boundaries. On the other hand, they make the model unsuitable to describe the switching of the hard layers (the transition from Fig. 6.2-b to Fig. 6.2-c).

We choose the reference frame as shown in Fig. 6.3, with the x axis along the out of plane direction. The soft layer occupies the region $0 \leq x \leq L$. Its magnetisation $\vec{M} = M_{\text{sat}}\,\vec{m}$ is defined only in this region and must satisfy the rigid pinning constraints:

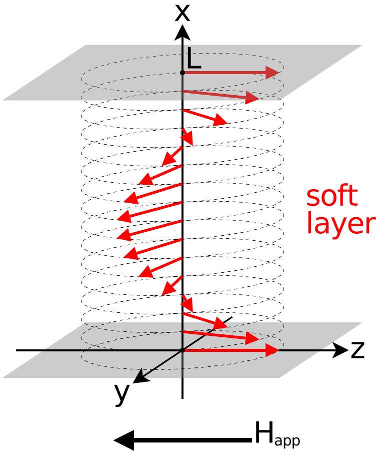

Figure 6.3: Simple one dimensional model of an exchange spring system. The red arrows represent the soft magnetisation and the two planes represent the hard-soft interfaces. The moments which lie in there are rigidly pinned along the positive z direction, while the external field is applied in the opposite direction.

$$\vec{m}(x = 0,\, L) = \hat{u},$$

where $\hat{u}$ is the direction of the hard moments in both the two external hard layers. The applied magnetic field is assumed to be antiparallel to $\hat{u}$. For simplicity, we chose $\hat{u} = \hat{z}$ (see Fig. 6.3), but we stress that this choice is not determinant for the derivation presented in this section.

We now write the energy, taking into account only the exchange coupling and the interaction with the applied field and neglecting the demagnetising field,

$$U[\vec{m}] = \int_0^L \mathrm{d}x \left\{ A\,(\partial_x \vec{m})^2 + \mu_0 M_{\text{sat}} H_{\text{app}}\, \vec{m}\cdot\hat{z} \right\}.$$

The same energy can be expressed in spherical coordinates, with $\hat{u}$ chosen as the polar axis. Spherical coordinates have an important advantage with respect to cartesian coordinates: they allow to easily take the constraint $\vec{m}^2 = 1$ into account. The energy of the system is then,

$$U[\theta, \phi] = \int_0^L \mathrm{d}x \left\{ A\,(\partial_x \theta)^2 + A\,\sin^2\theta\,(\partial_x \phi)^2 + \mu_0 M_{\mathrm{sat}} H_{\mathrm{app}} \cos\theta \right\}, \tag{6.1}$$

and depends only on two variables: the azimuthal angle $\phi(x)$ and the polar angle $\theta(x)$. The first two terms under the integral are the representation of $(\partial_x \vec{m})^2$ in spherical coordinates. The second term is the only one where ϕ appears, it is non negative and becomes zero (and hence mimimum) when $\partial_x \phi(x) = 0$. We then can assume $\partial_x \phi(x) = 0$, when searching for energy minima, since there is no other choice of $\partial_x \phi(x)$ which can lower the energy,

$$U[\theta, \phi] = \int_0^L \mathrm{d}x \left\{ A\,(\partial_x \theta)^2 + \mu_0 M_{\mathrm{sat}} H_{\mathrm{app}} \cos\theta \right\}. \tag{6.2}$$

6.2.1 Calculation of the bending field

We now prove that the state where the magnetisation is uniformly anti-parallel to the applied field H_{app}, minimises the energy when H_{app} is lower than a critical value, the bending field H_{b}. In order to do that, we show that the difference of energy between a given state $\Delta\theta(x) \neq 0$ and the uniformly aligned state $\theta(x) = 0$ is always positive, when $H_{\mathrm{app}} \leq H_{\mathrm{b}}$. Such an energy difference can be written as:

$$\Delta U = U[\Delta\theta] - U[0] = \int_0^L \mathrm{d}x \left\{ A\,(\partial_x \Delta\theta)^2 + \mu_0 M_{\mathrm{sat}} H_{\mathrm{app}} (\cos\Delta\theta - 1) \right\},$$

where $\Delta\theta(x)$ is chosen arbitrarily, but satisfies the rigid pinning requirement at the soft layer borders: $\Delta\theta(0) = \Delta\theta(L) = 0$. We now notice that $(\cos\Delta\theta - 1) = -2\sin^2\frac{\Delta\theta}{2}$. Moreover the inequality $\sin x < x$, which is valid for $x > 0$, implies that $\sin^2 x < x^2$, for every real number $x \neq 0$. Consequently $(\cos\Delta\theta - 1) > -\frac{(\Delta\theta)^2}{2}$:

$$\Delta U > \frac{\mu_0 M_{\mathrm{sat}}}{2} \int_0^L \mathrm{d}x \left\{ C\,(\partial_x \Delta\theta)^2 - H_{\mathrm{app}} (\Delta\theta)^2 \right\}. \tag{6.3}$$

Here we have introduced the quantity $C = 2A/\mu_0 M_{\mathrm{sat}}$. We notice that, when $\Delta\theta \to 0$, the right hand side becomes a good approximation for the left hand side, since $\sin\Delta\theta \to \Delta\theta$. We now use the Fourier representation of $\Delta\theta$,

$$\Delta\theta = \sum_{n=1}^{\infty} c_n \sin\left(\frac{\pi n}{L}\,x\right). \tag{6.4}$$

The cosine components are omitted, because they are not compatible with the requirement $\Delta\theta(0) = \Delta\theta(L) = 0$. Substituting (6.4) in (6.3) and using the orthogonality property:

$$\int_0^L \mathrm{d}x \, \sin\left(n \, \frac{\pi}{L} x\right) \sin\left(m \, \frac{\pi}{L} x\right) = \frac{L}{2} \, \delta_{n,m},$$

ΔU becomes:

$$\Delta U > \frac{\mu_0 M_{\mathrm{sat}} L}{4} \sum_{n=1}^{\infty} c_n^2 \, \left(n^2 \, H_{\mathrm{b}} - H_{\mathrm{app}}\right), \tag{6.5}$$

where,

$$H_{\mathrm{b}} = C \left(\frac{\pi}{L}\right)^2 = \frac{2A}{\mu_0 M_{\mathrm{sat}}} \left(\frac{\pi}{L}\right)^2. \tag{6.6}$$

When $H_{\mathrm{app}} \leq H_{\mathrm{b}}$, the quantity $(n^2 \, H_{\mathrm{b}} - H_{\mathrm{app}})$ is non negative for $n = 1$ and positive for $n \geq 2$. Consequently $\Delta U = U[\Delta\theta] - U[0]$ is positive. We conclude that $U[\Delta\theta] > U[0]$ for every $\Delta\theta \neq 0$. In other words, the configuration $\theta(x) = 0$ is a global energy minimum, when $H_{\mathrm{app}} \leq H_{\mathrm{b}}$. On the other hand, for $H_{\mathrm{app}} > H_{\mathrm{b}}$ and $c_i = c \, \delta_{i,1}$ the right hand side of Eq. (6.5) is negative, for every choice of the real constant $c \neq 0$. We conclude that, above the bending field, the uniformly aligned configuration $\theta(x) = 0$ is not a local (nor global) energy minimum.

6.2.2 Equilibrium magnetisation above the bending field

In the previous section we proved that the configuration $\theta(x) = 0$, which minimises the energy when $H_{\mathrm{app}} \leq H_{\mathrm{b}}$, is not a stable equilibrium configuration for $H_{\mathrm{app}} > H_{\mathrm{b}}$. We now show that, in such a regime, the equilibrium magnetisation twists towards the applied field. The derivation we present is similar to the one proposed by *Goto et al.* [73] for a bilayer exchange spring system. The equilibrium magnetisation is calculated by minimising the energy functional $U[\theta]$. Such a minimisation is done using a conventional variational approach: for a given $\theta(x)$, the variation $\delta U = U[\theta + \delta\theta] - U[\theta]$, is calculated with $\delta\theta(0) = \delta\theta(L) = 0$. If the configuration minimises the energy, then $\delta U = 0$, for every variation $\delta\theta$:

$$0 = \delta U = \int_0^L \mathrm{d}x \left\{2A \, \partial_x\theta \, \partial_x\delta\theta - \mu_0 H_{\mathrm{app}} M_{\mathrm{sat}} \sin\theta \, \delta\theta\right\}.$$

Integration by parts on the first integrand leads to

$$0 = \delta U = \int_0^L \mathrm{d}x \left\{-2A \, \partial_x^2\theta - \mu_0 H_{\mathrm{app}} M_{\mathrm{sat}} \sin\theta\right\} \, \delta\theta.$$

Which should hold for any variation $\delta\theta$ and therefore:

$$\partial_x^2\theta = -\frac{H_{\mathrm{app}}}{C} \sin\theta. \tag{6.7}$$

This is the pendulum equation. It has one trivial solution, $\theta(x) = 0$, which is — as previously remarked — an unstable equilibrium configuration, in the regime $H_{\mathrm{app}} > H_{\mathrm{b}}$.

We then have to search for other non trivial solutions to this equation. Fortunately, the pendulum equation is well known and its solution is derived and discussed in published works [74]. In the case we are considering, it can be written as:

$$\theta(x) = 2\,\arcsin[k\,\mathrm{sn}(\lambda x,\, k)], \tag{6.8}$$

where,

$$\lambda = \sqrt{\frac{H_{\mathrm{app}}}{C}} = \frac{\pi}{L}\sqrt{\frac{H_{\mathrm{app}}}{H_{\mathrm{b}}}},$$

and sn denotes the elliptic sine function. k can be obtained from the following relation:

$$\frac{\pi}{2}\sqrt{\frac{H_{\mathrm{app}}}{H_{\mathrm{b}}}} = K(k) = \int_0^{\pi/2} \frac{\mathrm{d}\phi}{\sqrt{1-k^2\sin^2\phi}}, \tag{6.9}$$

where $K(k)$ is called the complete elliptic integral of the first kind. We also have $k = \sin\frac{\theta_{\mathrm{max}}}{2}$, where θ_{max} is the maximum bending angle, which is reached at the center of the soft layer $\theta_{\mathrm{max}} = \theta(L/2)$.

The analytical derivation presented in this section is checked against the results of micromagnetic simulations carried out using *Nmag*. We study a system with soft layer made of permalloy ($M_{\mathrm{sat}} = 0.86 \times 10^6\,\mathrm{A/m}$, $A = 13 \times 10^{-12}\,\mathrm{J/m}$) and width $L = 20\,\mathrm{nm}$. For such a system the bending field is calculated from Eq. (6.6) as $H_{\mathrm{b}} = 0.594 \times 10^6\,\mathrm{A/m}$. We run a one-dimensional micromagnetic simulation increasing the applied field from 0 to $4 \times 10^6\,\mathrm{A/m}$. The increment ΔH is chosen to be smaller

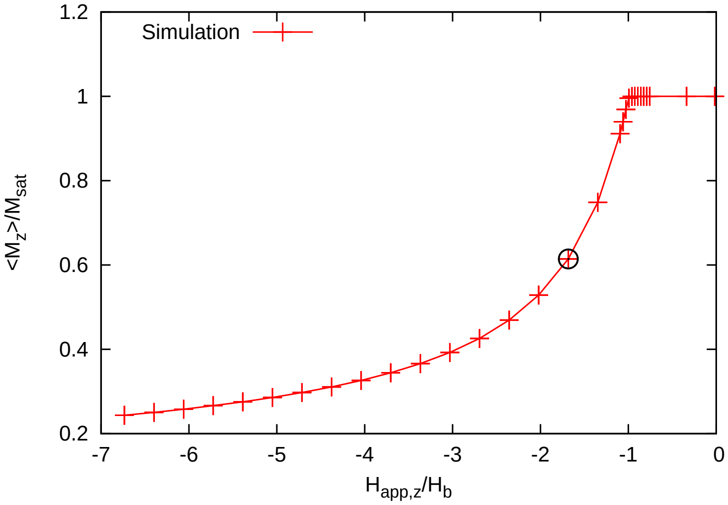

Figure 6.4: The z component of the magnetisation, averaged over the soft layer, as a function of the applied field, which is expressed in units of $H_{\mathrm{b}} = 0.594 \times 10^6\,\mathrm{A/m}$ (as calculated from Eq. (6.6)). The circle shows the configuration chosen for Fig. 6.5.

near the bending field, in order to resolve better the high slope which is characteristic of that region (see Fig. 6.4). The configuration obtained for $H_{\mathrm{app}} = 10^6\,\mathrm{A/m} = 1.68\,H_{\mathrm{b}}$ is shown in Fig. 6.5, together with the analytical solution. To calculate the analytical solution we first find k by solving Eq. (6.9). We then calculate $\theta(x)$, following Eq. 6.8. This is done by a small C program which uses the open source GSL library [75] for the calculation of $K(k)$, $\mathrm{sn}(\lambda x,\, k)$ and for the implementation of the bisection method. The agreement between the numerical result and the analytical solution is excellent.

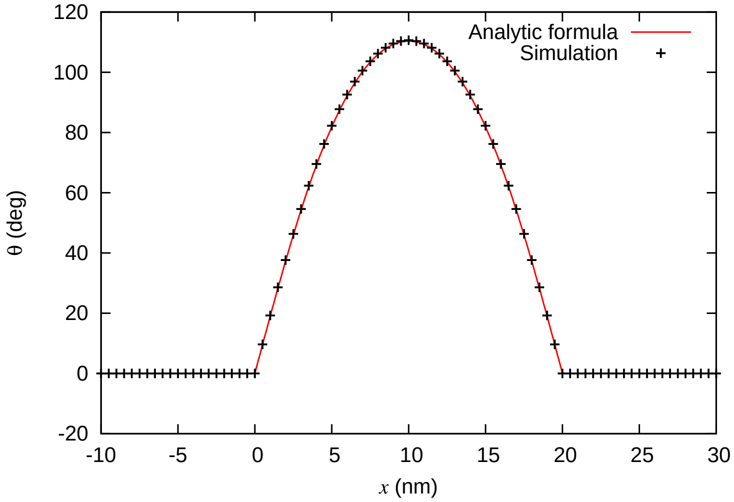

Figure 6.5: The configuration of the magnetisation (polar angle θ as a function of the position x) for a trilayer exchange spring system as obtained analytically from equations (6.8, 6.9) (solid line) and from a one-dimensional micromagnetic simulation performed using *Nmag*(crosses).

As a final remark, we notice that ϕ appears in the energy (6.1) only through $\partial_x \phi$. As a consequence, the energy is invariant for transformations $\phi \to \phi + \Delta\phi$. This means that, if we rotate each magnetic moment around the pinning direction $\hat{u}$ ($\hat{z}$ in the case considered here) by the same angle $\Delta\phi$, the energy of the system does not change. We then conclude that, when $H_{\mathrm{app}} > H_{\mathrm{b}}$, there are infinite states which equally minimise the energy. In multilayer films, this symmetry is broken by the demagnetising field, which favours in-plane directions for the magnetisation.

6.3 Computational study of the dynamics near the bending field

In the first part of the chapter we focused on the equilibrium configurations and on the static properties of multilayer exchange spring systems. Now we move our attention to the dynamic properties. In particular, we study the magnetisation dynamics for values of the applied field close to the bending field. One reason why we are so interested in this regime for the applied field can be understood by looking at Fig. 6.4. Here we see that the slope of the magnetisation is particularly high near the bending field, meaning that a small increase in the applied field can cause a great reaction of the magnetisation. In other words, near the bending field the system exhibits an amplified sensitivity to external perturbations. This feature is desirable when studying spin transfer torque phenomena, since it may help to reduce the current density required in order to obtain significant effects. Studying the dynamics of exchange spring systems near the bending field may then be relevant for technological applications. Moreover Brillouin light scattering experiments have shown interesting properties near the bending field, where the measured magnon frequency reaches a minimum value [76].

In this section we present computer investigations of a thin film made of one central magnetically soft YFe_2 layer sandwiched between two thinner magnetically hard $DyFe_2$ layers. We make such a peculiar material choice, because $DyFe_2$-YFe_2 multilayer samples have been the subject of experimental investigation in our group. We study the dynamical reaction of the system to small variations of the applied field and analyse numerically its oscillatory nature. Part of the results we present in the following sections have been published in the journal "IEEE Transactions on Magnetics" [54].

6.3.1 $DyFe_2$-YFe_2 multilayers

Three different kinds of atoms are present in $DyFe_2$-YFe_2 multilayers: one rare earth metal, Dy, and two transition metals, Fe and Y. The yttrium has negligible magnetic moment: only the iron moments contribute to the magnetisation of the soft YFe_2 layers. Conversely, in the hard layers, both the atomic species of the $DyFe_2$ compound give a relevant contribution to the magnetisation. At the temperature we consider here, $T = 100\,K$, $DyFe_2$ is a ferrimagnet, because the magnetic moment of iron is lower and antiparallel to the moment of dysprosium. The magnetisation dynamics in the trilayer system is determined mainly by the following interactions:

- in the $DyFe_2$ layers, a strong magnetocrystalline cubic anisotropy tries to keep the Dy moments along one easy axis direction;
- in the $DyFe_2$ layers, a strong antiferromagnetic Fe-Dy exchange coupling tries to keep the iron moments antiparallel to the Dy moments;
- in all the three layers, an even stronger [77] Fe-Fe exchange coupling opposes to

any spatial variation of the Fe magnetisation;

- the magnetostatic field tries to keep the magnetisation in the plane of the film.

The Dy-Dy exchange coupling is rather weak, due to the localisation of the magnetic orbitals (4f) of Dysprosium, and we ignore it. The typical configuration of the magnetisations of Fe and Dy, when there is no applied field, is shown in Fig. 6.6.

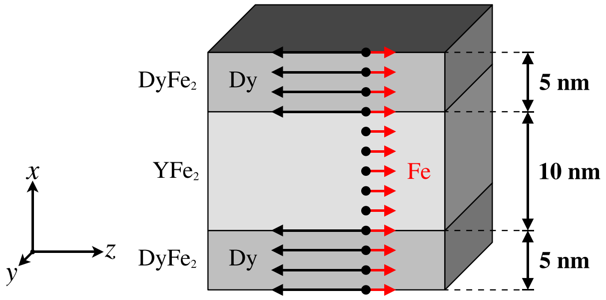

Figure 6.6: The Dy and Fe components of the magnetisation in a $DyFe_2$-YFe_2 multilayer exchange spring system. Dy moments (black arrows) are pinned along an easy axis direction, while Fe moments (red arrows) are forced to align along the opposite direction, due to the strong Dy-Fe antiferromagnetic exchange coupling.

We emphasise that the Fe-Fe exchange coupling occurs also across the boundary surfaces between the layers and thus affects the iron moments throughout all the sample. Indeed, the iron moments may be thought as belonging to a unique homogeneous crystal lattice which extends over all the three layers. Such a picture is justified by the similarity between the crystal lattices of $DyFe_2$ and YFe_2. In particular the two materials have the same lattice structure and almost the same size of primary cell (at temperature $T = 4.2\,\mathrm{K}$, the lattice constant is 0.7363 nm for YFe_2 and 0.7325 nm for $DyFe_2$ [78]). The main difference between the two materials is that Dy atoms in $DyFe_2$, are replaced with Y atoms in YFe_2. The computational model which we present in the next section exploits this peculiar characteristic of $DyFe_2$-YFe_2 multilayer systems.

Finally, it should be noted that $DyFe_2$-YFe_2 multilayers are usually grown by molecular beam epitaxy over a substrate. In such samples the different thermal dilatation of the layers with respect to the substrate is the source of a strain in the layers. The strain produces a magnetic anisotropy whose strength increases with temperature. However, for temperatures around and below ≈ 100 K, this effect is weak [79] and we neglect it. More details about the chemistry, the lattice structure and the magnetic properties of these systems can be found in the provided references [72, 80, 77, 81].

6.3.2 Computational model

We represent the configuration of the magnetic moments in the system with two continuous magnetisation fields $\vec{M}_{\rm Dy}(x)$ and $\vec{M}_{\rm Fe}(x)$, defined over the one-dimensional space: $\vec{M}_{\rm Dy}$ is the moment density of Dy atoms in $\rm DyFe_2$ and $\vec{M}_{\rm Fe}$ is the moment density of Fe atoms in $\rm DyFe_2$ and $\rm YFe_2$. Their norms are $M_{\rm Dy} = \|\vec{M}_{\rm Dy}\|$ and $M_{\rm Fe} = \|\vec{M}_{\rm Fe}\|$, which at the temperature of 100 K are $M_{\rm Dy} = 1.73\times 10^6$ A/m and — for both $\rm DyFe_2$ and $\rm YFe_2$— $M_{\rm Fe} = 0.55\times 10^6$ A/m. As remarked in the previous section, the assumption of continuity of $M_{\rm Fe}$ is supported by the fact that the iron sublattices in $\rm DyFe_2$ and in $\rm YFe_2$ have the same structure and similar lattice constants, making the density of iron moments almost identical in the two materials. This feature allows to use the same equation of motion for $\vec{M}_{\rm Fe}$ in all the three layers. The Brown's theory of micromagnetics is used to derive the effective fields acting on $\vec{M}_{\rm Dy}$ and $\vec{M}_{\rm Fe}$:

$$\begin{aligned}\vec{H}_{\rm Dy} &= \vec{H}_{\rm app} + \vec{H}_{\rm d} + \vec{H}_{\rm anis} + (J/\mu_0)\vec{M}_{\rm Fe},\\ \vec{H}_{\rm Fe} &= \vec{H}_{\rm app} + \vec{H}_{\rm d} + \vec{H}_{\rm exch} + (J/\mu_0)\vec{M}_{\rm Dy}.\end{aligned}$$

The applied field acts on both dysprosium and iron. $\vec{H}_{\rm Dy}$ also receives a cubic anisotropy contribution, whose three axes are shown in Fig. 6.7. The three coefficients used in the anisotropy expansion [82] are $K_1 = 33.9 \times 10^6\,{\rm J/m^3}$, $K_2 = -16.2 \times 10^6\,{\rm J/m^3}$ and $K_3 = 16.4 \times 10^6\,{\rm J/m^3}$. The iron experiences an exchange field $\vec{H}_{\rm exch} = \frac{2A}{\mu_0 M_{\rm Fe}}\nabla^2\vec{m}_{\rm Fe}$, where $A = 1.46 \times 10^{-11}\,{\rm J/m}$ is the exchange coupling constant, μ_0 is the free space permeability and $\vec{m}_{\rm Fe} = \vec{M}_{\rm Fe}/M_{\rm Fe}$. The dipolar field is taken into account in the limits of the one dimensional model and is calculated as $\vec{H}_{\rm d} = -M_x\hat{x}$, where M_x is the out-of-plane component of the total magnetisation field and $\hat{x}$ is the unit vector which points towards the positive x direction. This contribution evidently tries to reduce the surface magnetic charges, pulling the magnetisation into the plane of the film. The

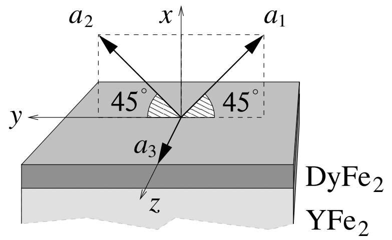

Figure 6.7: Orientation of the anisotropy axes of the $\rm DyFe_2$ layers with respect to the plane of the film. In the chosen reference frame the axis are $\vec{a}_1 = (1, -1, 0)/\sqrt{2}$, $\vec{a}_2 = (1, 1, 0)/\sqrt{2}$ and $\vec{a}_3 = \vec{a}_1 \times \vec{a}_2 = (0, 0, 1)$.

Dy-Fe coupling is modeled by an extra energy term $U = J \int \vec{M}_{\mathrm{Dy}} \cdot \vec{M}_{\mathrm{Fe}} \, \mathrm{d}z$, where $J = 2 \times 10^{-4}\,\mathrm{N/A^2}$ is the coupling constant [77] and the integral is done over the hard layers, where both magnetisations are defined. The Landau-Lifshitz-Gilbert equation is then used to calculate the dynamics of the two magnetisations.

The unidimensional model is a severe approximation for a description of the switching processes, where domain walls can form and play an important role, but for our investigation near the bending field the model should be quite accurate.

6.3.3 Results

For the simulations we use *Nmag*, the micromagnetic simulation package developed by our group [68], choosing the first order FEM to discretise the space. The mesh is a unidimensional lattice with constant spacing Δx: the whole meshed region (which is 20 nm wide) is subdivided into 162 cells of identical size, corresponding to 163 nodes with spacing $\Delta x = 20/162 \approx 0.123\,\mathrm{nm}$. This peculiar discretisation choice guarantees that each hard-soft boundary lies exactly at the middle of a discretisation cell (and thus "belongs" equally to both the soft and the hard layers), giving a more accurate representation of the geometry of the system and of the soft layer width, which is important in determining the bending field (see Eq. 6.6). We first calculate the hysteresis loop of the sample covering a wide range for the applied field $\vec{H}_{\mathrm{app}}$: from $-60\,\mathrm{T}$ to $60\,\mathrm{T}$ (see Fig. 6.8). $\vec{H}_{\mathrm{app}}$ is directed along the z axis. To avoid the system to be trapped in an unstable equilibrium configuration, we follow the standard practice of adding a small constant deviation to the applied field:

$$\vec{H}_{\mathrm{dev}} = (1,\, 1,\, 0) \times 0.005\,\mathrm{T}. \tag{6.10}$$

The high switching field (around $55\,\mathrm{T}$) represents a clear manifestation of Brown's paradox and the inadequacy of the one dimensional model to describe the switching of the hard layers. In this study, however, we are not concerned with this, since we are exploring a low-field region near the bending field, where the unidimensional model should be rather accurate. The bending field has been located around $H_{\mathrm{b}} \approx 3.95\,\mathrm{T}$ (for details about how this value has been obtained take a look at the caption of Fig. 6.8). A calculation from formula (6.6) yields $H_{\mathrm{b}} = 5.25\,\mathrm{T}$. We will see in the next sections, that such a difference is due to the non-infinite strength of the pinning in the hard layers.

After these preliminary calculations we start the main simulation. We prepare the system in the configuration where $\vec{M}_{\mathrm{Fe}}$ lies in the plane of the film and points along the

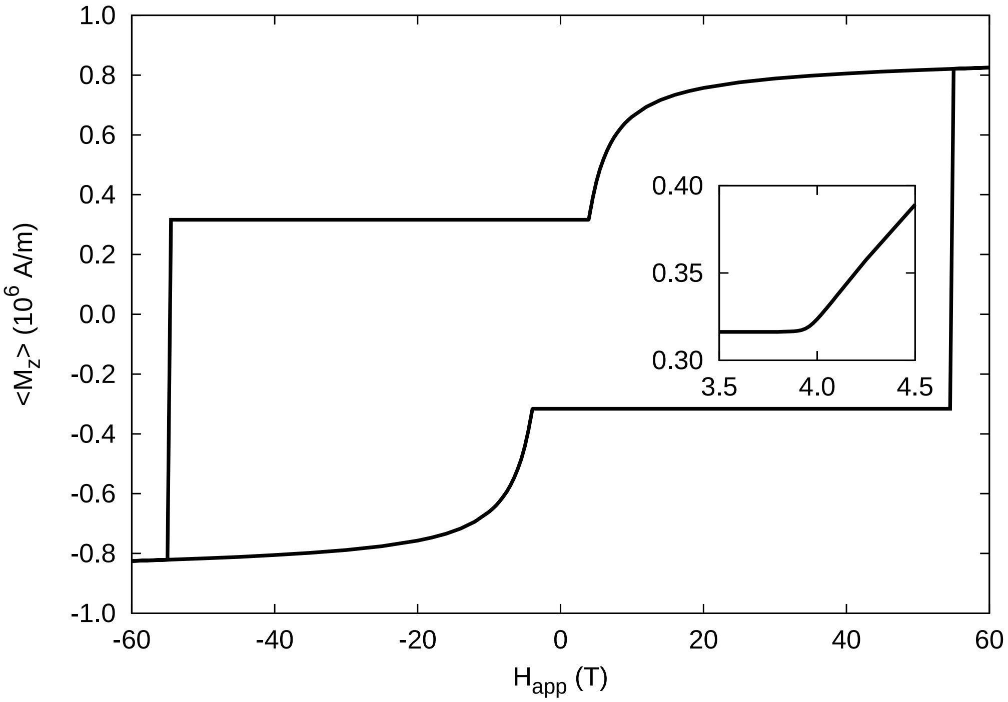

Figure 6.8: The hysteresis loop, for the total average magnetisation (includes the contribution for both Fe and Dy). The field is applied in the in-plane z direction. Notice the similarity between the bottom-left part of the hysteresis loop and Fig. 6.4. The inset shows a detail of the same curve in the vicinity of the bending field, $H_{\mathrm{b}} \approx 3.95\,\mathrm{T}$. This value has been obtained by fitting the data in the interval [4 T, 4.5 T] against the equation of a straight line and finding the intersection of such line with the continuation of the flat part of the hysteresis curve.

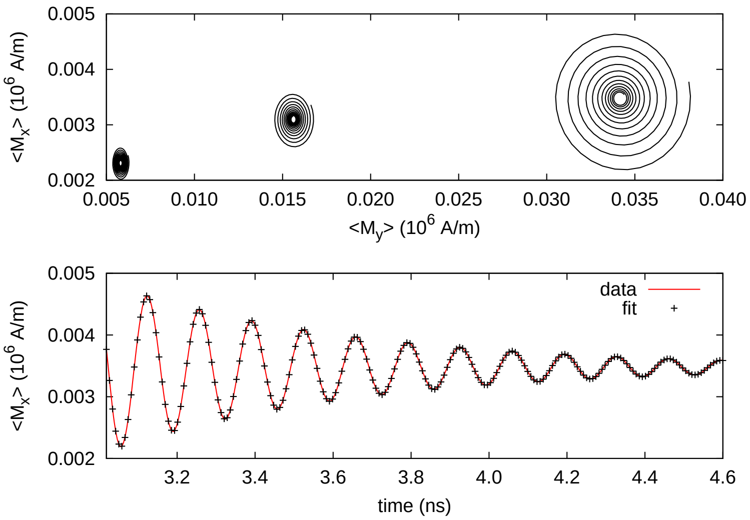

Figure 6.9: *Top:* The trajectories of $\langle \vec{M}_{\mathrm{Fe}} \rangle$ for $H_n = 3.50,\ 3.80,\ 3.90\,\mathrm{T}$. They show how equilibrium is restored when the field is changed from $H_{\mathrm{app}} = H_n + \Delta H$ to $H_{\mathrm{app}} = H_n$. Only the trajectories with $\alpha = 0.02$ are shown. Notice the different scales used for the two axes. *Bottom:* The x component of $\langle \vec{M}_{\mathrm{Fe}} \rangle$ is also plotted as a function of time for $\vec{H}_{\mathrm{app}} = 3.90\,\mathrm{T}$ together with the fitted curve.

positive z axis, while $\vec{M}_{\mathrm{Dy}}$ points along the opposite direction (see Fig. 6.6). This is an equilibrium configuration when the applied field $\vec{H}_{\mathrm{app}}$ is zero, which is the situation we choose to start with in our simulation. To study a certain applied field $\vec{H}_{\mathrm{app}} = -H_{\mathrm{app}}\,\hat{z}$ we use a two stage method. We first set the applied field to $H_{\mathrm{app}} = H_n + \Delta H$, where ΔH is a small perturbation, and run a simulation with a high damping parameter, $\alpha = 0.5$, to quickly determine the equilibrium magnetisation configuration. Then, starting from this very same configuration, we set $H_{\mathrm{app}} = H_n$, thus removing the perturbation in the applied field, and run the second simulation, using — this time — a realistic value for the damping parameter, $\alpha = 0.02$. The trajectory of the mean magnetisation $\langle \vec{M} \rangle$, through which the new equilibrium is restored, is then studied carefully. This procedure is repeated for many values of H_n. In particular $\vec{H}_{\mathrm{app}} = -H_{\mathrm{app}}\,\hat{z}$ points along the negative z direction with intensity H_{app} in the range from 0 to 12 T. We use more values of $\vec{H}_{\mathrm{app}}$ near the bending field, to better resolve the behaviour of the system in that region. For all the considered applied fields we use the same value of $\Delta H = 0.01\,\mathrm{T}$. It should be noted that we do not know precisely the value of the damping constant for YFe_2 and DyFe_2. Here we use the same value, $\alpha = 0.02$, for both the compounds.

A piece of the $\langle \vec{M}_{\mathrm{Fe}} \rangle$ trajectory, projected in the yx plane, is shown in Fig. 6.9 (top). The shape of these curves are all similar one to the other: they are spirals compressed along the out-of-plane x-direction. The graph shows only a few trajectories for $H_{\mathrm{app}} < H_{\mathrm{b}}$. For higher fields the spirals become much wider. In Fig. 6.9 (bottom) the x-component of the mean magnetisation is plotted as a function of time for the case $H_{\mathrm{app}} = 3.90\,\mathrm{T}$, just below the bending field. We fit these results to the equations of motion for a damped harmonic oscillator:

$$\begin{aligned} M_x(t) &= M_{x,0} + \Delta M_x\, e^{-\lambda_x t} \cos(\omega_x(t - t_0) + \varphi_x), \\ M_y(t) &= M_{y,0} + \Delta M_y\, e^{-\lambda_y t} \cos(\omega_y(t - t_0) + \varphi_y). \end{aligned} \tag{6.11}$$

We analyse the trajectories individually, to extract the frequencies, the decay times and the amplitudes of the oscillations produced as a reaction to the small perturbation ΔH. Fig. 6.10 collects the results of the fits. The corresponding curves match closely the data. An example is shown in Fig. 6.9. The graphs in Fig. 6.10 show clearly that near the bending field the dynamical reaction of the system is amplified: the same perturbation ΔH produces wider oscillations with smaller frequency and which last longer (higher decay time λ^{-1}). The plot of the frequencies shows a minimum near H_{b} and a qualitative behaviour which is consistent with previous experimental and theoretical results [76]. The amplitudes, whose magnitude depends on the value chosen for ΔH, show an interesting feature: the shapes of the spiral trajectories (Fig. 6.9) change with the applied field, being elongated in the in-plane y direction for $H_{\mathrm{app}} \ll H_{\mathrm{b}}$ and in the out-of-plane x direction for $H_{\mathrm{app}} \gg H_{\mathrm{b}}$. We conclude[2] that below the bending field the out of plane direction is "harder" than the in plane direction (meaning that moving along that direction has a greater energy cost), while, above the bending field, it becomes "softer".

6.4 Analytical study of the dynamics near the bending field

We now present analytical studies of the system which was investigated with computer simulations in the previous section, with the aim to understand and support the obtained results. We begin with introducing a first simple calculation, which is later extended gradually by more general and complex models. Such a presentation reflects the way the theory was actually derived.

---

[2] If $\alpha = 0$, the magnetisation moves on a constant-energy trajectory (which is likely to be an ellipse, in this case). If $0 < \alpha \ll 1$, this is not exactly true (the ellipse becomes a spiral), but still the magnetisation moves preferentially towards "soft" directions.

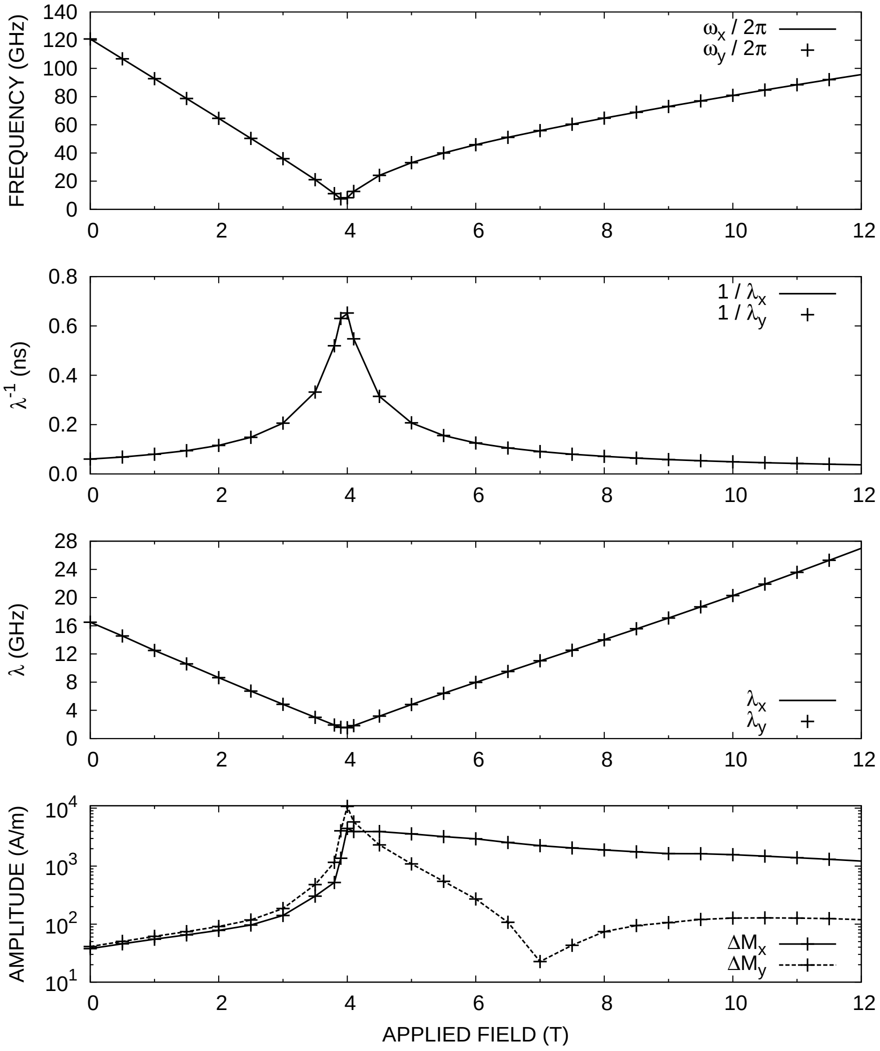

Figure 6.10: The parameters obtained from the fits. In the three top graphs solid lines are used for the values obtained fitting the x component $\langle M_x \rangle$, while the crosses are used for $\langle M_y \rangle$.

In particular we present a linearisation of the Landau-Lifshitz equation, which also includes the effects of an electric current flowing in the out of plane direction. The derivation leads to an expression for the trajectory of the magnetisation of the soft layer, which is valid only for values of the applied field below the bending field. We also get to a new formula for the bending field, which takes into account the penetration of the exchange spring inside the hard layers (finite pinning in the hard layers).

6.4.1 The infinite pinning model

As a first step, we assume infinitely strong pinning of the Dy magnetisation in the hard layers and infinitely strong antiferromagnetic coupling between Fe and Dy moments. This means that, inside the hard layers, both the magnetisations of iron and dysprosium do not change in time. In particular, if the Fe moments are rigidly aligned along the positive z direction (z is an easy axis), then the Dy moments are aligned in the opposite direction, as shown in Fig. 6.6. We can then neglect what happens inside the hard layers and focus on the soft layer. Since only the magnetisation of iron plays a role in the dynamics, we denote it simply by $\vec{M} \equiv \vec{M}_{\mathrm{Fe}}$. The configuration of the system is then fully described by just one vector field $\vec{M}(x, t)$ defined for $x \in [0, L]$, with

$$\vec{M}(x,t)/M_{\mathrm{sat}} = \hat{z}, \qquad x = 0,\, L. \tag{6.12}$$

The model is then very similar to the one which, in section 6.2, was used to study the static equilibrium configurations of a simple trilayer exchange spring. The dynamics of $\vec{M}$ is governed by the Landau-Lifshitz equation (2.3). If we neglect the damping processes we can rewrite it as:

$$\partial_t \hat{M} = -\gamma' \, \hat{M} \times \vec{H}, \tag{6.13}$$

where $\hat{M} = \vec{M}/M_{\mathrm{sat}}$ and $\vec{H} = C\,\partial_x^2 \hat{M} + \vec{H}_{\mathrm{app}}$. Here we neglect the demagnetising field and the corresponding shape anisotropy. We now show that one solution to (6.13) has the simple form:

$$\vec{M} = \left(M_\perp \cos\omega t \, \sin\left(\pi \frac{x}{L}\right), M_\perp \sin\omega t \, \sin\left(\pi \frac{x}{L}\right), M_\parallel \right). \tag{6.14}$$

This can be done by replacing (6.14) into (6.13). To do this, we first calculate the exchange field $\vec{H}_{\mathrm{exch}} = C\,\partial_x^2 \hat{M}$:

$$\begin{aligned} \vec{H}_{\mathrm{exch}} &= -\frac{C}{M_{\mathrm{sat}}} \left(\frac{\pi}{L}\right)^2 \sin\left(\pi \frac{x}{L}\right) (M_\perp \cos\omega t, M_\perp \sin\omega t, 0) \\ &= -C \left(\frac{\pi}{L}\right)^2 \left(\hat{M} - \hat{z}\,\frac{M_\parallel}{M_{\mathrm{sat}}}\right). \end{aligned}$$

Then we replace it into Eq. (6.13):

$$\partial_t \hat{M} = -\gamma' \, \hat{M} \times \left[\vec{H}_{\mathrm{app}} - C \left(\frac{\pi}{L}\right)^2 \left(\hat{M} - \hat{z}\, \frac{M_\parallel}{M_{\mathrm{sat}}}\right)\right].$$

Considering that $\hat{M} \times \hat{M} = 0$ and that $\vec{H}_{\mathrm{app}} = -H_{\mathrm{app}}\, \hat{z}$, this equation becomes:

$$\partial_t \hat{M} = -\gamma' \, \hat{M} \times \hat{z} \left[C \frac{M_\parallel}{M_{\mathrm{sat}}} \left(\frac{\pi}{L}\right)^2 - H_{\mathrm{app}}\right].$$

$\partial_t \hat{M}$ can be calculated by taking the time derivative of Eq. (6.14), which gives $\partial_t \hat{M} = -\omega \, \gamma' \, \hat{M} \times \hat{z}$. Substituting this in the previous equation, we get to the condition:

$$\omega = \gamma' \left| H_{\mathrm{app}} - C \frac{M_\parallel}{M_{\mathrm{sat}}} \left(\frac{\pi}{L}\right)^2 \right|.$$

We recognise the bending field $H_{\mathrm{b}} = C \left(\frac{\pi}{L}\right)^2$ and rewrite this equation as

$$\omega = \gamma' \left| H_{\mathrm{app}} - \frac{M_\parallel}{M_{\mathrm{sat}}} H_{\mathrm{b}} \right|.$$

Below or near the bending, field $M_\parallel \approx M_{\mathrm{sat}}$ and

$$\omega \approx \gamma' \, \left| H_{\mathrm{app}} - H_{\mathrm{b}} \right|. \tag{6.15}$$

This equation gives us the value that ω should have in order for Eq. (6.14) to be a solution of Eq. (6.13). We notice that there are other solutions to Eq. (6.13). In particular, if we replace $\sin(x\,\pi/L)$ with $\sin(x\,n\pi/L)$ for $n = 1, 2, \ldots$, we get to solutions corresponding to higher values of ω and higher energy (since to greater values of n corresponds a stronger spatial variation of the magnetisation and hence a higher exchange energy). Eq. (6.15) says that the frequency should decrease linearly with H_{app} and vanish exactly for $H_{\mathrm{app}} = H_{\mathrm{b}}$, which is qualitatively the behaviour observed in Fig. 6.10. From a quantitative point of view, fitting the data of this same figure with Eq. (6.15), for $H_{\mathrm{app}} < 3.9\,\mathrm{T}$, yields:

$$\gamma'|_{\mathrm{fit}} = (2.280 \pm 0.015) \times 10^5\,\mathrm{m/(As)}, \qquad H_{\mathrm{b}}|_{\mathrm{fit}} = (4.212 \pm 0.017)\,\mathrm{T}.$$

The result of the fit is shown in Fig. 6.11. $\gamma'|_{\mathrm{fit}}$ agrees reasonably well with the value used in the simulations, $\gamma' = 2.210 \times 10^5\,\mathrm{m/(As)}$. Concerning the bending field H_{b}, the fit leads to a value, $H_{\mathrm{b}}|_{\mathrm{fit}} = 4.212\,\mathrm{T}$, which is sensibly smaller than the one calculated from formula (6.6), $H_{\mathrm{b}} = 5.25\,\mathrm{T}$, suggesting that the rigid pinning assumption may be quite a rough approximation. There are two other remarks to make. First, the frequency $\omega(H_{\mathrm{app}})$ does not seem to vanish at the bending field, as can be deduced

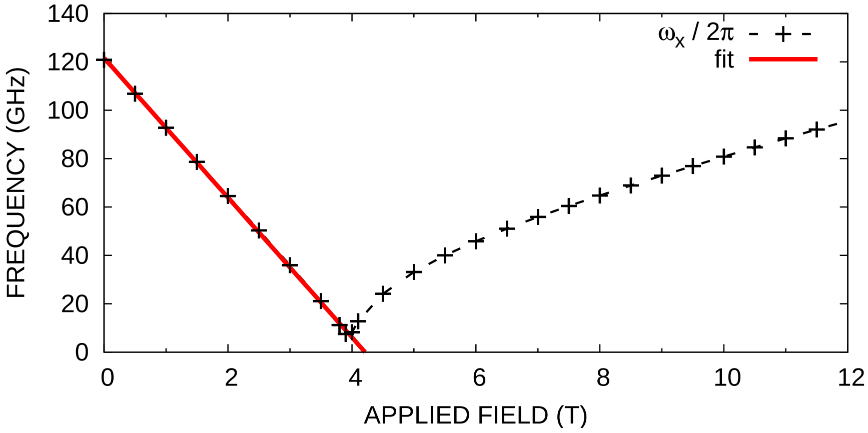

Figure 6.11: The data in the graph on the top of Fig. 6.10 is fitted against Eq. (6.15) below the bending field. Notice that the line intersects the horizontal axis in $H_\mathrm{b}|_\mathrm{fit}$, which is visibly greater than the value for which the frequency is minimum: the fit overestimates the bending field.

by looking at where the red line from the fit intersects the horizontal axis in Fig. 6.11. Such a disagreement is likely to be due to neglecting the demagnetising effects in the analytical model. Indeed, the reason why the frequency vanishes at the bending field is because the applied field perfectly compensates the "alignment" action of the exchange coupling. Such compensation allows the magnetisation to freely move out of the alignment direction, i.e. the z axis. In the numerical model, however, there is an additional binding effect which cannot be compensated just by applying a field along the z direction: this is the demagnetising field, which acts by pulling the magnetisation in the plane of the film. When the magnetisation tries to rotate out of the alignment direction, it experiences such a shape anisotropy and is hence pulled back into the plane of the film. As a consequence, the magnetisation precesses with positive frequency even at the bending field. A second thing to notice is the disagreement between $H_\mathrm{b}|_\mathrm{fit}$ and the value $H_\mathrm{b} = 3.95\,\mathrm{T}$ which was deduced in the caption of Fig. 6.8: apparently, the fit of Fig. 6.11 overestimates the bending field. This deviation is likely to be another consequence of neglecting the demagnetising effects in the analytical model. Indeed, from Fig. 6.11, we see that the non vanishing value of $\omega(H_\mathrm{app} = H_\mathrm{b})$ causes the fitted line to intersect the horizontal axis above the value of H_app for which ω is minimum.

6.4.2 The pinning field model

The infinite pinning model discussed in the previous section neglects the characteristics of the hard layers. In particular, the exchange spring is confined inside the soft layer, by imposing infinite pinning and hence the rigidity of the magnetisation in the hard layers. In this section, we present a more general model, where the strength of the pinning in the hard layers is finite. The model we employ is again a single field model: we neglect the dysprosium magnetisation and assume that the iron magnetisation is defined and has homogeneous properties throughout all the three layers. This means that we treat the trilayer system as if it were a monolayer system, made only of soft material. The only difference between the central soft layer and the two external hard layers lies in the applied field H_{app}. Indeed, we assume that $\vec{H}_{\mathrm{app}}(x) = -H_{\mathrm{app}}(x)\,\hat{z}$, with

$$H_{\mathrm{app}}(x) = \begin{cases} H_0 & \text{for } |x| < L/2 \\ H_0 - H_{\mathrm{P}} & \text{for } |x| \geq L/2 \end{cases} ,$$

and the reference frame is chosen as in Fig. 6.6. Inside the soft layer the iron magnetisation experiences only the external field $\vec{H}_{\mathrm{app}} = -H_0\,\hat{z}$, while inside the hard layers a fictitious pinning field H_{P} is introduced to keep the iron magnetisation aligned along the positive z direction, $\vec{H}_{\mathrm{app}} = (H_{\mathrm{P}} - H_0)\,\hat{z}$ with $H_{\mathrm{P}} > H_0 > 0$. Modeling the pinning in such a way may seem artificial, but in the next sections we show that this approach is actually general enough to capture most of the physics of the DyFe$_2$-YFe$_2$ trilayer system for applied fields below the bending field. We can now write down the equation of motion (2.3) for the Fe magnetisation, the Landau-Lifshitz equation:

$$-\frac{1}{\gamma'}\partial_t \hat{M} = \hat{M} \times \vec{H} + \alpha\,\hat{M} \times (\hat{M} \times \vec{H}). \tag{6.16}$$

We notice that there is an "ambiguity" in the choice of $\vec{H}[\hat{M}]$, which stems from the property $\hat{M} \times \hat{M} = 0$. In particular, $\vec{H}[\hat{M}]$ can be replaced with $\vec{H}[\hat{M}] + \lambda\,\hat{M}$, obtaining an equivalent equation, for any real number λ. Here we choose $\lambda = -\hat{M} \cdot \vec{H}$ and define $\vec{h}[\hat{M}] = \vec{H}[\hat{M}] - \hat{M}\,(\hat{M} \cdot \vec{H}[\hat{M}])$. This choice guarantees that $\vec{h}$ is orthogonal to $\hat{M}$, which lets us rewrite (6.16) as

$$-\frac{1}{\gamma'}\partial_t \hat{M} = \hat{M} \times \vec{h} - \alpha\,\vec{h}, \tag{6.17}$$

where we used the well known identity $\vec{A} \times (\vec{B} \times \vec{C}) = \vec{B}\,(\vec{A} \cdot \vec{C}) - \vec{C}\,(\vec{A} \cdot \vec{B})$. This equation is still rather difficult to solve analytically. Fortunately, below the bending field, the equilibrium configuration is very simple: $\hat{M}$ is just aligned uniformly along the positive z axis. A linearisation may then be employed in order to study the magnetisation dynamics near equilibrium. This is a procedure which is often used in magnetic resonance (MR) studies to find the resonance frequency for the interaction of an electromagnetic wave with the magnetisation of a ferromagnetic material [83, 84].

Linearising the Landau-Lifshitz equation is a rather simple task. First, we assume that the magnetisation configuration $\hat{M}$ slightly deviates from the equilibrium configuration $\hat{M}_0$:

$$\hat{M} = \hat{M}_0 + \vec{R}, \quad \|\vec{R}\| \ll 1.$$

This expression can then be substituted in Eq. (6.17):

$$-\frac{1}{\gamma'}\partial_t \vec{R} = \hat{M}_0 \times \vec{h} + \vec{R} \times \vec{h} - \alpha\, \vec{h}. \tag{6.18}$$

We notice that $\mathcal{O}(\|\vec{h}\|) = \mathcal{O}(\|\vec{R}\|)$. We can prove it easily expanding $\vec{h}[\vec{R}]$ in Taylor series and observing that $\vec{h}[\vec{R} = 0] = 0$. This must necessarily happen, because $\vec{h}[\vec{R} = 0]$ is the component of $\vec{H}[\hat{M}_0]$ orthogonal to $\hat{M}_0$, which must be zero for $\hat{M}_0$ to be an equilibrium configuration (the torque $\hat{M}_0 \times \vec{H}[\hat{M}_0]$ is zero at equilibrium). We then conclude that the second term in the right hand side of (6.18) has order $\mathcal{O}(\vec{R}^2)$ and can be neglected. With this approximation one obtains

$$\partial_t \vec{R} = -\gamma'\, \hat{M}_0 \times \vec{h} + \gamma'\, \alpha\, \vec{h}. \tag{6.19}$$

This equation can now be applied to our specific case, for which $\hat{M}_0 = \hat{z}$:

$$\begin{cases} \partial_t r_{\mathrm{x}} = \gamma'(\alpha\, h_{\mathrm{x}} + h_{\mathrm{y}}) \\ \partial_t r_{\mathrm{y}} = \gamma'(\alpha\, h_{\mathrm{y}} - h_{\mathrm{x}}) \\ \partial_t r_{\mathrm{z}} = h_{\mathrm{z}} = 0 \end{cases}, \tag{6.20}$$

where $\vec{R} = (r_{\mathrm{x}},\, r_{\mathrm{y}},\, r_{\mathrm{z}})$ and $\vec{h} = (h_{\mathrm{x}},\, h_{\mathrm{y}},\, h_{\mathrm{z}})$. $h_{\mathrm{z}} = 0$, because $\vec{h}$ is orthogonal to $\hat{M}_0 = \hat{z}$ at the first order in $\vec{R}$. This formula can be written again in vectorial notation:

$$\partial_t \vec{R} = \gamma'(\alpha + \mathbf{J})\vec{h}, \tag{6.21}$$

where the scalar α should be interpreted as $\alpha\, \mathbf{I}$ and $\mathbf{I}$ is the identity matrix while $\mathbf{J}$ is the following square matrix:

$$\mathbf{J} = \begin{pmatrix} 0 & 1 \\ -1 & 0 \end{pmatrix}. \tag{6.22}$$

Here and in the next formulas we omit the third component of vectors and the third row/column of matrices. Indeed, the problem we are considering is effectively a two dimensional problem. We now consider the effective field $\vec{h}$, which receives contributions from the applied field and from the exchange field. We have to remember that $\vec{h} = \vec{H} - (\vec{H} \cdot \hat{M})\, \hat{M}$, where $\vec{H} = C\, \partial_x^2 \hat{M} + \vec{H}_{\mathrm{app}} = C\, \partial_x^2 \vec{R} - H_{\mathrm{app}}\, \hat{z}$. Applying this formula and neglecting terms of order $\vec{R}^2$, we find $\vec{h} = C\, \partial_x^2 \vec{R} + H_{\mathrm{app}}\, \vec{R}$, which substituted inside (6.21), gives:

$$\partial_t \vec{R} = \gamma'(\alpha + \mathbf{J})(C\, \partial_x^2 + H_{\mathrm{app}})\vec{R}. \tag{6.23}$$

6.4.3 The solutions

Equation (6.23) can be diagonalised, transforming $\vec{R} = \mathbf{D}\,\vec{D}$, where:

$$\mathbf{D} = \frac{1}{\sqrt{2}} \begin{pmatrix} 1 & -i \\ -i & 1 \end{pmatrix}, \quad \mathbf{D}^{-1} = \frac{1}{\sqrt{2}} \begin{pmatrix} 1 & i \\ i & 1 \end{pmatrix}, \tag{6.24}$$

Making this substitution in equation (6.23),

$$\partial_t \vec{D} = \gamma'(\alpha + \mathbf{D}^{-1}\mathbf{J}\mathbf{D})(C\,\partial_x^2 + H_{\text{app}})\vec{D},$$

where,

$$\mathbf{D}^{-1}\mathbf{J}\mathbf{D} = \begin{pmatrix} -i & 0 \\ 0 & i \end{pmatrix}.$$

Then, if $\vec{D} = (d_+,\, d_-)$, we have

$$\partial_t d_\pm = \gamma'(\alpha \mp i)(C\,\partial_x^2 + H_{\text{app}})d_\pm. \tag{6.25}$$

For now, we again consider the case of infinite pinning in the hard layers and try to find a solution with the same spatial dependency used in Eq. (6.14). In particular, we take $d_\pm(x,t) = T_\pm(t)\,\sin(x\,\pi/L)$, where $T_\pm(t)$ contain the time dependence of the solution. We then get to:

$$\partial_t d_\pm = \omega(-\alpha \pm i)d_\pm, \tag{6.26}$$

and $\omega = \gamma'(C\,(\pi/L)^2 - H_{\text{app}})$. The solutions of these two independent equations are:

$$d_+(x,t) = d_{+,0}\,e^{-\alpha\omega t + i\omega t}\,\sin\left(\frac{\pi}{L}\,x\right), \qquad d_-(x,t) = i d_{-,0}\,e^{-\alpha\omega t - i\omega t}\,\sin\left(\frac{\pi}{L}\,x\right),$$

and,

$$\vec{R} = \mathbf{D}\vec{D} = \frac{e^{-\alpha\omega t}}{\sqrt{2}} \begin{pmatrix} d_{+,0}\,e^{+i\omega t} + d_{-,0}\,e^{-i\omega t}, \\ -i(d_{+,0}\,e^{+i\omega t} - d_{-,0}\,e^{-i\omega t}) \end{pmatrix} \sin\left(\frac{\pi}{L}\,x\right).$$

Requiring $\vec{R}$ to be real for all the possible values of t one obtains the condition $d_{+,0} = R_0 e^{i\varphi}/\sqrt{2}$ and $d_{-,0} = R_0 e^{-i\varphi}/\sqrt{2}$ for two given real constants R_0 and φ. The solution then becomes:

$$\vec{R}(x,t) = R_0\,\sin\left(\frac{\pi}{L}\,x\right)\,e^{-\alpha\omega t}\,\left(\cos(\omega t + \varphi),\, \sin(\omega t + \varphi)\right), \tag{6.27}$$

which can be integrated in space to obtain the time dependence of the spatially averaged magnetisation:

$$\begin{aligned} \langle M_x(t) \rangle &= M_0\,e^{-\alpha\omega t}\cos(\omega t + \varphi), \\ \langle M_y(t) \rangle &= M_0\,e^{-\alpha\omega t}\sin(\omega t + \varphi). \end{aligned} \tag{6.28}$$

This result confirms that the average magnetisation approaches equilibrium by moving in spiral trajectories, as was assumed in Eqs. (6.11). In particular, comparing the two pairs of equations we notice that:

- in Eqs. (6.11) we chose to have independent amplitudes ΔM_x and ΔM_y for the x and y oscillations. The fits led to quite different values for $M_{x,0}$ and $M_{y,0}$, meaning that the spirals are compressed more along one direction rather than the other. On the other hand, the theoretical trajectories from Eqs. (6.28) do not exhibit such a compression. This discrepancy between theory and simulations is likely to be due to omitting the shape anisotropy (i.e. the demagnetising field) in the theoretical description. Indeed, in the simulation the demagnetising field tries to keep the magnetisation in the plane of the film by compressing the trajectories in the out of plane direction. In the theoretical description, the demagnetising field is not taken into account and hence such a compression is not observed.
- the spirals of Eqs. (6.28) are centered around the point (0, 0), while for the simulated trajectories we found nonzero values of $M_{x,0}$ and $M_{y,0}$. This is not surprising, since the applied field in the simulations is not perfectly aligned along the z direction (remember the deviation introduced with Eq. (6.10)).

Eq. (6.28) contains however other interesting results. First, it confirms that, below the bending field, the frequency can be written as $\omega = \gamma'(H_{\mathrm{b}} - H_{\mathrm{app}})$, where $H_{\mathrm{b}} = C\left(\frac{\pi}{L}\right)^2$. This is not a new result: it was already derived in the previous section using a simpler model. There is however a new important result: we see from Eq. (6.28) that the parameter λ introduced in Eqs. (6.11) (as λ_x and λ_y) is related to the frequency ω by the following formula:

$$\lambda = \alpha\omega. \tag{6.29}$$

We check the correctness of this relation by plotting the values of λ_x obtained by the fits of Fig. 6.10 together with the values ω_x multiplied by α. If Eq. (6.29) is correct, then the two curves should lie one over the other. This is what we did in Fig. 6.12.

We conclude the section pointing out that the theoretical results which we have obtained are meaningful only when $H_{\mathrm{app}} < H_{\mathrm{b}}$. For greater values of the applied field, λ becomes non-positive with the consequence that the magnetisation does not approach the configuration $\hat{M}_0 = \hat{z}$ as $t \to +\infty$. In these cases we can only conclude that the magnetisation leaves the configuration $\hat{M}_0 = \hat{z}$ to approach another different equilibrium configuration.

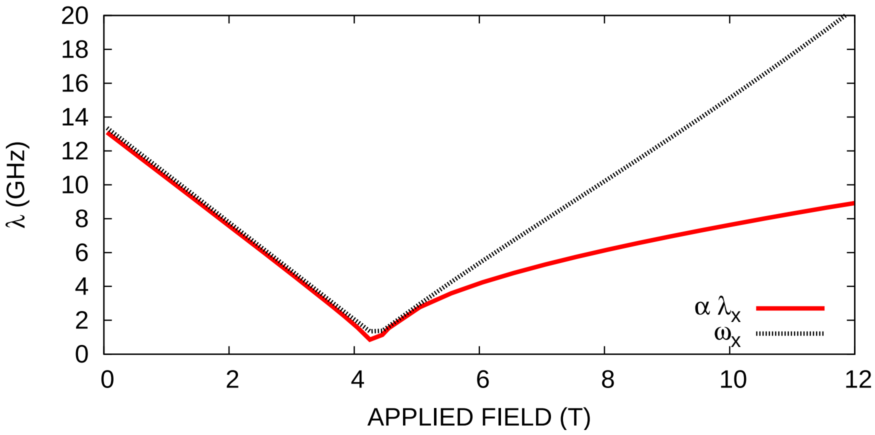

Figure 6.12: λ_x and $\alpha\omega_x$ are plotted in the same graph in order to check the relation $\lambda = \alpha\omega$ derived in the text. The two curves match rather well for values of the applied field below the bending field, as predicted by Eq. (6.29). The graph uses the same data as in Fig. 6.10.

6.4.4 Spin transfer torque contributions

In the previous sections we have studied the dynamics in a three layer exchange spring system. We have seen that the soft magnetisation exhibits an enhanced sensitivity near the bending field. In particular, the same small increment of applied field leads to oscillations whose amplitude is maximum when the applied field is close to the bending field, as shown in Fig. 6.10. We anticipated at the beginning of Sec. 6.3, that such a behaviour may be desirable when studying spin transfer torque effects. Indeed, greater amplitude for the same external stimulus means also weaker external stimulus to get to the same amplitude. In other words, enhanced magnetisation reaction may allow us to use lower current densities to obtain the same effect on the magnetisation dynamics. Such a characteristic is particularly important, since one major difficulty in building spin transfer torque devices lies on the excessive current density which is often required to obtain significant effects.

In this section we include spin transfer torque effects in the linearised model that we have presented previously in the chapter. In particular we linearise Eq. (3.13), the Landau-Lifshitz equation with the inclusion of the Zhang-Li terms. The system is the three layer exchange spring system which we have considered in the previous sections, with the difference that a current is now assumed to flow in the out of plane direction. We treat the trilayer as if it were made of just one material and assume that the electron and spin transport properties are homogeneous throughout all the three layers. This assumption relies on the fact that the iron sublattices of YFe_2 and

DyFe$_2$ have almost identical structure and lattice constant and that the yttrium and dysprosium sublattices are not playing any role with respect to the electron transport phenomena.

The equation we want to linearise is now Eq. (3.13), which we rewrite as:

$$\partial_t \hat{M} = -\gamma' \hat{M} \times \vec{H}_{\mathrm{P}} - \gamma' \hat{M} \times (\hat{M} \times \vec{H}_{\mathrm{D}}), \tag{6.30}$$

where we have defined the two fields $\vec{H}_{\mathrm{P}}$ and $\vec{H}_{\mathrm{D}}$ as:

$$\begin{aligned} \vec{H}_{\mathrm{P}} &= \vec{H} + \frac{\overline{a} v'}{\gamma'} \partial_x \hat{M}, \\ \vec{H}_{\mathrm{D}} &= \alpha \vec{H} + \frac{a v'}{\gamma'} \partial_x \hat{M}. \end{aligned}$$

A straightforward generalisation of equation (6.21) is then:

$$\partial_t \vec{R} = \gamma' \left(\vec{H}_{\mathrm{D}} + \mathbf{J} \vec{H}_{\mathrm{P}} \right), \tag{6.31}$$

and:

$$\begin{aligned} \vec{H}_{\mathrm{P}} &= C\, \partial_x^2 \vec{R} + \frac{\overline{a} v'}{\gamma'} \partial_x \vec{R} + H_{\mathrm{app}} \vec{R}, \\ \vec{H}_{\mathrm{D}} &= \alpha C\, \partial_x^2 \vec{R} + \frac{a v'}{\gamma'} \partial_x \vec{R} + \alpha H_{\mathrm{app}} \vec{R}. \end{aligned}$$

The form of equation (6.31) is very similar to the form of equation (6.21) and a similar strategy can be followed to find the solutions. The same transformation $\vec{R} = \mathbf{D}\, \vec{D}$ then leads to an equation similar to (6.25):

$$\partial_t d_\pm = -\left[\gamma' C(-\alpha \pm i) \partial_x^2 + v'(-a \pm i\, \overline{a}) \partial_x + \gamma' H_{\mathrm{app}}(-\alpha \pm i) \right] d_\pm. \tag{6.32}$$

Defining $\gamma' C(-\alpha \pm i) = c_\pm$, $(-a \pm i\, \overline{a}) = 2 b_\pm\, c_\pm\, (1+\alpha^2)$ (consequently $b_\pm = (\xi \pm i)/2\gamma C$) and $U(x) = -H_{\mathrm{app}}(x)/C$, this equation becomes:

$$\partial_t d_\pm = c_\pm \left(-\partial_x^2 - 2 b_\pm v\, \partial_x + U \right) d_\pm.$$

We conclude that d_+ and d_- obey two equations with the same form, but different coefficients. We therefore have only to study the following equation:

$$\partial_t d(x,t) = c\, \mathbf{S}\, d(x,t), \text{ where } \mathbf{S} = -\partial_x^2 - 2bv\, \partial_x + U(x). \tag{6.33}$$

This equation if formally very similar to the Schrödinger equation. Actually, when $j = 0$, Eq. (6.33) becomes identical to the Schrödinger equation, with just one difference. While in the Schrödinger equation c is $-i/\hbar$, a pure complex number, in Eq. (6.33)

c is $\gamma' C(-\alpha \pm i)$ and has non-vanishing real and complex parts. As a consequence, while the Schrödinger equation gives rise to a time evolution which preserves energy, Eq. (6.33) leads to dissipation of energy, unless the real part of c, Re $c = -\gamma' C\alpha$ and hence the damping, α, is zero! We will return on this point in the next section.

The similarities which Eq. (6.33) has with the Schrödinger equation suggest that we may be able to use a formalism analogous to the one of quantum mechanics in order to deal with it: its solutions may be easily found once the eigenfunctions of the operator $\mathbf{S}$ are known. Unfortunately, when $j \neq 0$, this operator is not Hermitian and therefore its eigenvalues are not guaranteed to be real numbers. Moreover the term $2bv\,\partial_x$ is not real and consequently the eigenfunctions of $\mathbf{S}$ cannot be chosen to be real functions of space. Fortunately the problem of finding the eigenvalues/eigenfunctions of the operator $\mathbf{S}$ can be trivially related to the problem of finding the eigenvalues/eigenfunctions of an Hermitian operator $\mathbf{S}_0$:

Theorem. *$s_0(x)$ is an eigenfunction of the operator $\mathbf{S}_0 = -\partial_x^2 + U(x)$, with eigenvalue σ_0, if and only if $s(x) = e^{-bv\,x}\, s_0(x)$ is eigenfunction of $\mathbf{S} = \mathbf{S}_0 - 2bv\,\partial_x$ with eigenvalue $\sigma = \sigma_0 + (bv)^2$.*

Proof. First, we calculate $\partial_x s(x)$ and $\partial_x^2 s(x)$ for an arbitrary (well behaved) function $s_0(x)$ and $s(x) = e^{-bv\,x}\, s_0(x)$,

$$\begin{aligned} \partial_x s(x) &= e^{-bv\,x} \left(\partial_x s_0(x) - bv s_0(x)\right), \\ \partial_x^2 s(x) &= e^{-bv\,x} \left(\partial_x^2 s_0(x) - 2bv \partial_x s_0(x) + (bv)^2 s_0(x)\right), \end{aligned}$$

which are used to calculate $\mathbf{S}\, s(x)$,

$$\begin{aligned} \mathbf{S}\, s(x) &= e^{-bv\,x} \left(-\partial_x^2 + (bv)^2 + U(x)\right) s_0(x) \\ &= e^{-bv\,x} \left(\mathbf{S}_0 + (bv)^2\right) s_0(x). \end{aligned} \tag{6.34}$$

We now deal with the forward implication and assume $s_0(x)$ is an eigenfunction of $\mathbf{S}_0$ with eigenvalue σ_0. Eq. (6.34) then becomes:

$$\begin{aligned} \mathbf{S}\, s(x) &= e^{-bv\,x} \left(\sigma_0 + (bv)^2\right) s_0(x) \\ &= \left(\sigma_0 + (bv)^2\right) s(x), \end{aligned}$$

which proves that $s(x)$ is eigenfunction of $\mathbf{S}$ with eigenvalue $\sigma = \sigma_0 + (bv)^2$. We now deal with the backward implication and assume that $s(x)$ is eigenfunction of $\mathbf{S}$ with eigenvalue σ. We can then substitute the left hand side of Eq. (6.34) with $\sigma\, s(x) = \sigma\, e^{-bv\,x}\, s_0(x)$, obtaining:

$$\sigma\, e^{-bv\,x}\, s_0(x) = e^{-bv\,x} \left(\mathbf{S}_0 + (bv)^2\right) s_0(x).$$

Simplifying the exponential and rearranging the terms, we get $\mathbf{S}_0\, s_0(x) = \sigma_0\, s_0(x)$. $\square$

This result simplifies considerably the problem of finding eigenvalues of $\mathbf{S}$, since it states that they are in a one-to-one correspondence with the eigenvalues of $\mathbf{S}_0$, which is an Hermitian operator.

6.4.5 The energy in the linearised model

The parallelism between the formalism of quantum mechanics and the one we are developing here is striking. One is tempted to think to $\mathbf{S}$ as the reduced[3] Hamiltonian of the system and to calculate the reduced energy as $\langle \vec{D} \mid \mathbf{S} \mid \vec{D}\rangle$. This obviously would not make sense, since $\mathbf{S}$ is not Hermitian, but what about $\mathbf{S}_0$? In this section we try to understand better the meaning of these operators and their relationship with the total energy of the system.

The total energy of the system, when there is no current travelling through it, is:

$$E[\hat{M}] = \mu_0 M_{\text{sat}} \int_{-\infty}^{+\infty} \mathrm{d}x \left[\frac{C}{2} (\partial_x \hat{M})^2 - \hat{M} \cdot \vec{H}_{\text{app}} \right].$$

In our case $\vec{H}_{\text{app}} = -H_{\text{app}}(x)\, \hat{z}$. Moreover $\hat{M}^2 = 1$ and hence $\partial_x \hat{M}^2 = 2\hat{M} \cdot \partial_x \hat{M} = 0$. A further differentiation leads to: $0 = \partial_x(\hat{M} \cdot \partial_x \hat{M}) = (\partial_x \hat{M})^2 + \hat{M} \cdot \partial_x^2 \hat{M}$. We then can write:

$$E[\hat{M}] = \mu_0 M_{\text{sat}} \int_{-\infty}^{+\infty} \mathrm{d}x \left[-\frac{C}{2} \hat{M} \cdot \partial_x^2 \hat{M} + H_{\text{app}}(x)\, (\hat{M} \cdot \hat{z}) \right].$$

Now we remember that $\vec{R}$ was defined such that $\hat{M} = \hat{M}_0 + \vec{R}$, where $\hat{M}_0 = \hat{z}$ is the equilibrium configuration for the magnetisation. In particular from $1 = \hat{M}^2 = (\hat{z} + \vec{R})^2$, we get $\hat{z} \cdot \vec{R} = -\vec{R}^2/2$ and we can write:

$$E[\vec{R}] = \text{const.} + \mu_0 M_{\text{sat}} \int_{-\infty}^{+\infty} \mathrm{d}x \left[-\frac{C}{2} \hat{M} \cdot \partial_x^2 \vec{R} - H_{\text{app}}(x)\, \frac{\vec{R}^2}{2} \right].$$

Since the energy is defined up to a constant, we omit the (infinite) constant in what follows. We now replace $-H_{\text{app}}(x) = C\, U(x)$, coherently with the previous definition of U. We also notice that $\hat{M} \cdot \partial_x^2 \vec{R} = (\hat{z} + \vec{R}) \cdot \partial_x^2 \vec{R}$, where $\hat{z} \cdot \partial_x^2 \vec{R} = \partial_x^2 (\hat{z} \cdot \vec{R}) = -\partial_x^2 \vec{R}^2/2$, which gives zero contribution, if we assume $\vec{R}^2 \to 0$ and $\partial_x \vec{R}^2 \to 0$ for $x \to \pm\infty$. We then obtain:

$$E[\vec{R}] = \mu_0 M_{\text{sat}} \frac{C}{2} \int_{-\infty}^{+\infty} \mathrm{d}x \left[-\vec{R} \cdot \partial_x^2 \vec{R} + U(x)\, \vec{R}^2 \right],$$

---

[3] If $\mathbf{H}\psi(x) = \left(-\frac{\hbar^2}{2m} \partial_x^2 + V(x) \right) \psi(x) = E\psi(x)$ is the time-independent Schrödinger equation of a one dimensional particle of mass m and $A = \hbar^2/2m$, we call $\mathbf{H}/A$, $U(x) \equiv V(x)/A$ and $\varepsilon = E/A$ reduced Hamiltonian, reduced potential and reduced energy respectively.

which can be expressed as:

$$E[\vec{R}] = \mu_0 M_{\mathrm{sat}} \frac{C}{2} \int_{-\infty}^{+\infty} \mathrm{d}x\, \vec{R} \cdot \mathbf{S}_0 \vec{R} \equiv \mu_0 M_{\mathrm{sat}} \frac{C}{2} \langle \vec{R} \mid \mathbf{S}_0 \mid \vec{R} \rangle.$$

The notation on the right hand side is the so-called bra-ket notation and is here used as a short-hand for the integral appearing in the same equation. We now notice that the operator $\mathbf{S}_0$ commutes with the matrix $\mathbf{D}$ defined in Eq. (6.24) ($\mathbf{S}_0$ acts in the same way over all the components of the vector it is applied to). We then have $\mathbf{S}_0 = \mathbf{D}\mathbf{S}_0\mathbf{D}^{-1}$, and:

$$E[\vec{R}] = \mu_0 M_{\mathrm{sat}} \frac{C}{2} \langle \vec{R} \mid \mathbf{D}\mathbf{S}_0\mathbf{D}^{-1} \mid \vec{R} \rangle = \mu_0 M_{\mathrm{sat}} \frac{C}{2} \langle \vec{D} \mid \mathbf{S}_0 \mid \vec{D} \rangle.$$

From this expression it is now easy to prove that, as anticipated in the previous section, if c in Eq. (6.33) has a non-vanishing real part, then the energy is not preserved in time but rather decreases. In our particular case, since $\mathrm{Re}\, c = -\gamma' C \alpha$, this means that to a non zero damping constant α corresponds a dynamics where the energy decreases with time. Taking the time derivative of $E[\vec{R}]$ and considering that $\mathbf{S}_0$ does not depend explicitly on time, we get:

$$\frac{\mathrm{d}E[\vec{R}]}{\mathrm{d}t} = \mu_0 M_{\mathrm{sat}} \frac{C}{2} \left(\frac{\partial \langle \vec{D} \mid}{\partial t} \mathbf{S}_0 \mid \vec{D} \rangle + \langle \vec{D} \mid \mathbf{S}_0 \frac{\partial \mid \vec{D} \rangle}{\partial t} \right).$$

We can now use Eq. (6.33) and obtain:

$$\frac{\mathrm{d}E[\vec{R}]}{\mathrm{d}t} = -\gamma' \mu_0 M_{\mathrm{sat}} C^2 \alpha \, \langle \vec{D} \mid \mathbf{S}_0^2 \mid \vec{D} \rangle.$$

The right hand side of this equation is non-positive, meaning that the energy will decrease (or stay constant) in time. When $\alpha = 0$, the energy is conserved in time. Note that C cannot be zero, since we have previously assumed $C \neq 0$, when defining the potential $U = -H_{\mathrm{app}}/C$. We point out that this result holds only for $j = 0$. When $j \neq 0$, the term $2bv\,\partial_x$ gives an extra contribution to the energy which can lead to an increase or decrease of energy depending on the particular magnetisation configuration and on the intensity of the applied current density.

6.4.6 The solutions including the spin-transfer-torque effects

We are now ready to obtain a solution of (6.31). We first have to find $d_\pm$, which are the solutions of the two equations

$$\partial_t d_\pm = c_\pm \mathbf{S}_\pm \, d_\pm, \quad \text{where } \mathbf{S}_\pm = \mathbf{S}_0 - 2b_\pm v\, \partial_x. \qquad (6.35)$$

We proceed as follows: given an eigenfunction $s_0(x)$ of $\mathbf{S}_0$ with eigenvalue σ_0, we define the following two functions

$$s_\pm(x) = e^{-b_\pm v\,x} s_0(x).$$

Since $\mathbf{S}_0$ is a purely real operator, we can choose the eigenfunction $s_0(x)$ to be real for every value x, similarly to what is usually done for one dimensional problems in quantum mechanics. We know that $\mathbf{S}_\pm\, s_\pm(x) = \sigma_\pm\, s_\pm(x)$, where $\sigma_\pm = \sigma_0 + (b_\pm v)^2$. Consequently the two functions

$$\begin{aligned} d_+(x,t) &= d_{+,0}\, e^{c_+\sigma_+\,t} s_+(x) = d_{+,0}\, e^{f_+(x,t)} s_0(x), \\ d_-(x,t) &= i\, d_{-,0}\, e^{c_-\sigma_-\,t} s_-(x) = i\, d_{-,0}\, e^{f_-(x,t)} s_0(x), \end{aligned}$$

are solutions of (6.35) and,

$$\begin{aligned} f_\pm(x,\, t) &= c_\pm \sigma_\pm\, t - b_\pm v\, x = c_\pm \left[\sigma_0 + (b_\pm v)^2\right]\, t - b_\pm v\, x \\ &= \gamma' C(-\alpha \pm i) \left[\sigma_0 + \left(\tfrac{(\xi \pm i)\, v}{2\gamma C}\right)^2\right]\, t - \tfrac{(\xi\pm i)\, v}{2\gamma C}\, x \\ &= (-\lambda \pm i\omega)\, t + (\kappa \pm ik)\, x, \end{aligned}$$

where,

$$\begin{aligned} \lambda &= \gamma' C\alpha \left[\sigma_0 + \left(\tfrac{v}{2\gamma C}\right)^2 \left(\xi^2 - 1 + \tfrac{2\xi}{\alpha}\right)\right] = \lambda_0 + \tfrac{\alpha (v')^2}{4\gamma' C}\left(\xi^2 - 1 + \tfrac{2\xi}{\alpha}\right), \\ \omega &= \gamma' C \left[\sigma_0 + \left(\tfrac{v}{2\gamma C}\right)^2 \left(\xi^2 - 1 - 2\alpha\xi\right)\right] = \omega_0 + \tfrac{(v')^2}{4\gamma' C}\left(\xi^2 - 1 - 2\alpha\xi\right), \\ \kappa &= -\tfrac{\xi v}{2\gamma C}, \\ k &= -\tfrac{v}{2\gamma C}, \end{aligned} \tag{6.36}$$

where $\lambda_0 = \gamma' C\alpha\sigma_0$ and $\omega_0 = \gamma' C\sigma_0$ are the zero current values for λ and ω and depend on the particular shape of the applied field $H_{\text{app}}(x)$, which indeed determines the eigenvalue σ_0. We now apply the transformation $\vec{R} = \mathbf{D}\,\vec{D}$, to obtain:

$$\vec{R}(x,t) = \frac{s_0(x) e^{\kappa x}\, e^{-\lambda t}}{\sqrt{2}} \begin{pmatrix} d_{+,0}\, e^{+i(\omega t + kx)} + d_{-,0}\, e^{-i(\omega t + kx)}, \\ -i\left(d_{+,0}\, e^{+i(\omega t + kx)} - d_{-,0}\, e^{-i(\omega t + kx)}\right) \end{pmatrix}.$$

Requiring $\vec{R}$ to be real for all the possible values of t one obtains the condition $d_{+,0} = R_0 e^{i\psi}/\sqrt{2}$ and $d_{-,0} = R_0 e^{-i\psi}/\sqrt{2}$ for two given real constants R_0 and ψ. The solution then becomes:

$$\vec{R}(x,t) = R_0\, s_0(x) e^{\kappa x}\, e^{-\lambda t} \left(\cos\left(\omega t + kx + \psi\right), \sin\left(\omega t + kx + \psi\right)\right). \tag{6.37}$$

We can now integrate this equation in space, to obtain the average magnetisation as a function of time. In order to do that, we write down the averages $\langle M_x(t)\rangle$ and $\langle M_y(t)\rangle$

as:

$$\langle M_x(t)\rangle = \mathrm{Re}\, I(t),$$
$$\langle M_y(t)\rangle = \mathrm{Im}\, I(t),$$

where:

$$I(t) = R_0 \int_0^L s_0(x)\, e^{\kappa x}\, e^{-\lambda t}\, e^{i(\omega t + kx + \psi)} \mathrm{d}x = R_0\, e^{-\lambda t}\, e^{i\omega t}\, I_0,$$

where $I_0 = I(t = 0)$ is a constant which depends on the particular shape of the eigenfunction s_0. We take $I_0 = Fe^{i\varphi}$, where F and φ are two unknown constants. We then get to:

$$I(t) = R_0 F\, e^{-\lambda t} e^{i\,(\omega t + \varphi)},$$

from which we deduce:

$$\begin{aligned}\langle M_x(t)\rangle &= M_0\, e^{-\lambda t} \cos(\omega t + \varphi),\\ \langle M_y(t)\rangle &= M_0\, e^{-\lambda t} \sin(\omega t + \varphi).\end{aligned} \tag{6.38}$$

Surprisingly, we conclude that the spin polarised current does not change the shape of the average magnetisation trajectory, which has indeed the same spiral form which we got in Eq. (6.28). The polarised current, however, leads to corrections to the precession frequency ω and to the damping parameter λ, as shown in Eq. (6.36). In particular, from this equation we can get to a generalisation of Eq. (6.29):

$$\lambda = \alpha\omega + \frac{\xi v^2}{2\gamma C}. \tag{6.39}$$

Note that this equation and Eqs. (6.38) are extremely general, since we have not made any particular assumption on the shape of the eigenfunction s_0 and hence on the particular form of the applied field $H_{\mathrm{app}}(x)$. These results should hold for any reasonable choice of $H_{\mathrm{app}}(x)$, as long as the state where the magnetisation is uniformly aligned along the $\hat{z}$ direction is an equilibrium configuration.

6.4.7 Discussion and validation

In the previous section we found that the average soft magnetisation of an exchange spring approaches equilibrium by moving in spiral trajectories, even when an electric current flows orthogonal to the layers. The current, however, changes the precession frequency ω as well as the damping rate λ. Interestingly, the variation of the frequency $\Delta\omega$ and of damping rate $\Delta\lambda$ are found not to depend on the applied field H_{app} and the geometry of the system (thickness of the soft layer). In particular, from Eqs. (6.36),

$$\Delta\lambda = \lambda - \lambda_0 = \frac{\alpha(v')^2}{4\gamma' C}\left(\xi^2 - 1 + \frac{2\xi}{\alpha}\right) \approx \frac{(v')^2}{4\gamma' C}\left(2\xi - \alpha\right), \tag{6.40}$$

$$\Delta\omega = \omega - \omega_0 = \frac{(v')^2}{4\gamma' C}\left(\xi^2 - 1 - 2\alpha\xi\right) \approx -\frac{(v')^2}{4\gamma' C}. \tag{6.41}$$

Assuming the values $\alpha = 0.02$, $\xi = 0.01$, $M_{\text{Fe}} = 0.55 \times 10^6\,\text{A/m}$, $A = 1.46 \times 10^{-11}\,\text{J/m}$ and a polarised current $Pj = X \times 10^{12}\,\text{A/m}^2$, one gets $v = X^2 \times 105.5\,\text{m/s}$ and:

$$\begin{aligned}\Delta\lambda &= X^2 \times 594\,\text{s}^{-1},\\ \Delta\omega &= -X^2 \times 0.0473\,\text{GHz}.\end{aligned}$$

We see that even for the case $X = 1$, which corresponds to quite a high current density ($Pj = 10^{12}\,\text{A/m}^2$), the spin transfer torque effects on the frequency and on the damping rate are rather weak. In particular, for the DyFe_2-YFe_2 trilayer simulated in Sec. 6.3, it is difficult to identify any current-induced effects on ω and λ. Indeed, the values we have just calculated for $\Delta\omega$ and $\Delta\lambda$ are respectively three and seven orders of magnitude smaller than the typical values shown in the graphs of Fig. 6.10. We conclude that, in this kind of exchange spring, the effects of the applied electric current are not relevant as we expected. In particular, if, on the one hand, the magnetisation reaction to external stimuli is amplified near the bending field, on the other, the magnetisation is there nearly homogeneous leading to weak spin transfer torque effects.

This conclusion is still the result of a purely theoretical analysis. It is then desirable to prove and validate it numerically. In order to do that, we repeat the simulations of Sec. 6.3 with the inclusion of the spin transfer torque as modeled by Eq. (3.13). The procedure employed is identical to the one used in Sec. 6.3 to obtain ω and λ as functions of the applied field. The only difference is that the dynamical relaxation to the equilibrium is done in the presence of an applied current. In this way we can obtain graphs analogous to the ones of Fig. 6.10, but with the inclusion of spin transfer torque effects.

By carrying out the micromagnetic simulations for a current density $Pj = 10^{12}\,\text{A/m}^2$ we found that — as predicted by Eqs. (6.40, 6.41) — the current induced effects are so weak that the graphs for ω and λ look identical to the ones of Fig. 6.10. For this reasons we do not show them. We rather repeat the simulations for a higher current density $Pj = 10^{13}\,\text{A/m}^2$ (corresponding to $X = 10$), so that we get amplified current-induced effects and we can then perform a better validation of the theory. Note that, since our main objective here is the validation of the theory, we chose a value $\xi = 0.05$ which is higher than the one which is typically used $\xi = 0.01$ (notice that we do not have any experimental estimate of ξ for YFe_2). This choice gives higher values for $\Delta\lambda$ and thus facilitates the comparison between theory and simulations. The results of the simulations are shown in Fig. 6.13, where ω and λ are plotted as functions of the applied field. Note that also the zero-current results from Fig. 6.10 are included to

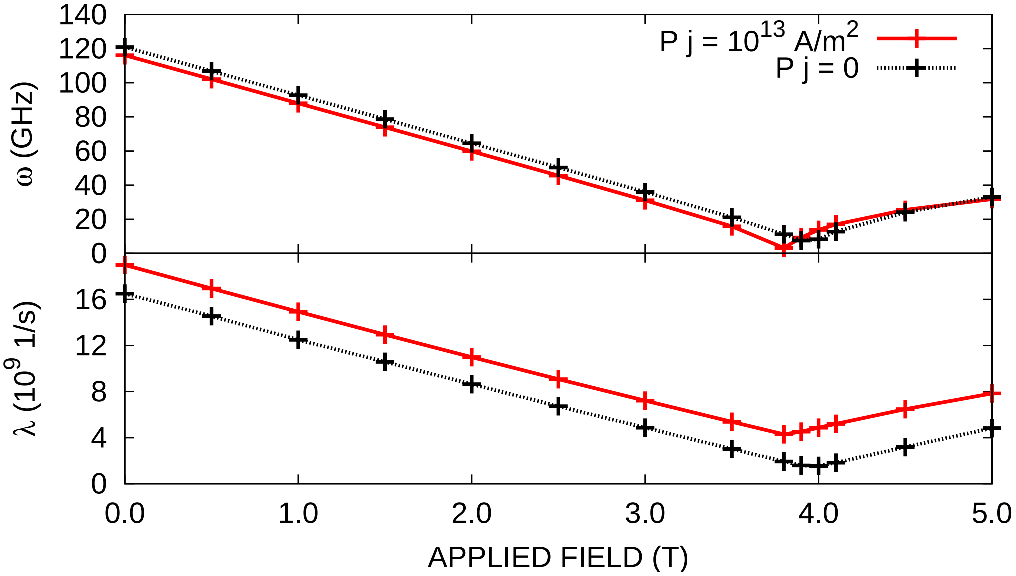

Figure 6.13: The frequency and damping rate which characterise the near-equilibrium dynamics of the magnetisation in a $DyFe_2$-YFe_2-$DyFe_2$ exchange spring system are plotted as functions of the applied field. The red curves are obtained in the presence of a current flowing orthogonal to the layers. The dashed black curves are the same as in Fig. 6.10 and are shown just to allow a better visual assessment of the effects of the current.

allow a better evaluation of the changes induced by the application of the current. Fig. 6.13 shows that — in agreement with the theoretical prediction — the current induces a translation of the frequencies and of the damping rates by fixed amounts $\Delta\omega$ and $\Delta\lambda$, respectively.

For the frequencies, we subtract the solid red curve and the dashed black curve to obtain the separation between the two. We then fit the resulting values with a constant function $\Delta\omega(H_{\text{app}}) = \text{const}$, for $H_{\text{app}} < 3.5\,\text{T}$ and get $\Delta\omega|_{\text{fit}} = (-4.83 \pm 0.06)\,\text{GHz}$. We get good agreement with the theoretical value, $\Delta\omega = -4.73\,\text{GHz}$, calculated from Eq. (6.41): the difference is around 2.1 %. Similarly, for the damping rates, we get $\Delta\lambda|_{\text{fit}} = (2.386 \pm 0.019) \times 10^9\,\text{s}^{-1}$ while the theoretical result is $\Delta\lambda = 2.367 \times 10^9\,\text{s}^{-1}$. The difference between the two is 0.8 %.

Note that, since $\Delta\omega$ and $\Delta\lambda$ do not depend on the geometry of the system, one may choose a system with thicker soft layer. In a system where $L = 100\,\text{nm}$, for example, the bending field is reduced by a factor 100, according to Eq. (6.6), and the corresponding frequencies and damping rates are then reduced by the same factor, as deduced from Eq. (6.15) and Eq. (6.29), but the values of $\Delta\omega$ and $\Delta\lambda$ are unchanged. In such a system, a current density of $Pj = 10^{12}\,\mathrm{A/m^2}$ should then lead to a significant *relative* change of frequencies and damping rates.

We end the section by pointing out that the results we have obtained so far consider only the case of constant applied current (DC). It may be argued that a pulsed current (AC) is likely to lead to greater effects (maybe through the mechanism described in Ref. [85]). In this thesis, however, we won't study spin transfer effects for pulsed currents. We rather focus on different exchange spring systems (see Ch. 7), which — we think — are more promising than the $\mathrm{DyFe_2}$-$\mathrm{YFe_2}$-$\mathrm{DyFe_2}$ trilayer film considered so far.

6.4.8 Infinite pinning field

In the theoretical analysis we have conducted so far, we haven't yet made any assumptions on the particular shape of the applied field $H_{\mathrm{app}}(x)$. We have been able anyway to characterise the spin transfer torque effects, which are indeed independent of $H_{\mathrm{app}}(x)$. In the remaining part of the chapter we will try to determine the effects of the shape of $H_{\mathrm{app}}(x)$. When choosing $H_{\mathrm{app}}(x)$, we also determine the potential $U(x)$ and hence the operator $\mathbf{S}_0$. As a consequence, also the ground state $s_0(x)$ and the corresponding eigenvalue σ_0 are determined. This allows to determine the actual dynamics of the magnetisation as well as the exact value of the bending field.

In this section we assume that:

$$H_{\mathrm{app}}(x) = \begin{cases} H_0 & \text{for} |x| < L/2 \\ -\infty & \text{for} |x| \geq L/2 \end{cases} , \tag{6.42}$$

where H_0 is the intensity of magnetic field, which is applied along the direction $-\hat{z}$. The function $U(x) = -H_{\mathrm{app}}(x)/C$ has the following form:

$$U(x) = \begin{cases} -H_0/C & \text{for} |x| < L/2 \\ +\infty & \text{for} |x| \geq L/2 \end{cases} . \tag{6.43}$$

Then the operator $\mathbf{S}_0$ is formally identical to the reduced Hamiltonian of a one dimensional quantum particle in an infinitely deep square potential well. This problem has well known solutions. One finds [86] that the system has an entirely discrete spectrum and the eigenvalues are,

$$\sigma_n = -\frac{H_0}{C} + \left(\frac{\pi}{L} n\right)^2 , \qquad n = 1, 2, \ldots$$

In particular, for the ground state,

$$\sigma_1 = \frac{H_{\mathrm{b}} - H_0}{C},$$

where $H_{\mathrm{b}} = C\left(\frac{\pi}{L}\right)^2$ is defined as before. Then we can calculate explicitly the parameters (6.36):

$$\begin{array}{rcl} \lambda & = & \alpha\gamma'\left[H_{\mathrm{b}} - H_0 + \frac{v^2}{4\gamma'^2 C}\left(\xi^2 - 1 + \frac{2\xi}{\alpha}\right)\right], \\ \omega & = & \gamma'\left[H_{\mathrm{b}} - H_0 + \frac{v^2}{4\gamma'^2 C}\left(\xi^2 - 1 - 2\alpha\xi\right)\right]. \end{array} \tag{6.44}$$

The solution (6.37) requires $\lambda \geq 0$ in order to converge for $t \to +\infty$. We can find then a requirement over the field:

$$H_0 \leq H'_{\mathrm{b}} = H_{\mathrm{b}} + \frac{v^2}{4\gamma^2 C}\left(\xi^2 - 1 + \frac{2\xi}{\alpha}\right).$$

H'_{b} is the bending field, when the current is applied (in contrast with H_{b}, which is the zero-current bending field). When $H_0 = H'_{\mathrm{b}}$,

$$\omega = -\frac{\xi}{2\gamma C}\left(\alpha + \frac{1}{\alpha}\right)v^2.$$

6.4.9 Finite pinning field

A more realistic situation with respect to the one considered in the previous section is finite pinning in the hard layers:

$$H_{\mathrm{app}}(x) = \begin{cases} H_0 & \text{for} |x| < L/2 \\ H_0 - H_{\mathrm{P}} & \text{for} |x| \geq L/2 \end{cases}, \tag{6.45}$$

where H_0 is the intensity of the applied magnetic field, while H_{P} is the “pinning” field. We assume $H_{\mathrm{P}} > H_0 > 0$. The corresponding potential $U(x)$ is:

$$U(x) = \begin{cases} -H_0/C & \text{for} |x| < L/2 \\ (H_{\mathrm{P}} - H_0)/C & \text{for} |x| \geq L/2 \end{cases}. \tag{6.46}$$

The quantum mechanical analogue is now a one-dimensional particle in a finite square well. The energy spectrum of this system is divided in different regions:

- $-H_0/C < \sigma < (H_{\mathrm{P}} - H_0)/C$, for which a discrete spectrum is obtained (bound states);
- $\sigma > (H_{\mathrm{P}} - H_0)/C$, for which a continuous and degenerate spectrum is obtained (with reflection and transmission of waves);

The ground state σ_1 is in the discrete spectrum, whose eigenvalues σ_n can be determined graphically [86] as the intersections between the function $f(\xi) = 2\sin^{-1}\xi$ and the linear functions $y_n(\xi) = \pi n - L\sqrt{H_{\mathrm{P}}}\,\xi$, where ξ lies between 0 and 1 and is expressed in terms

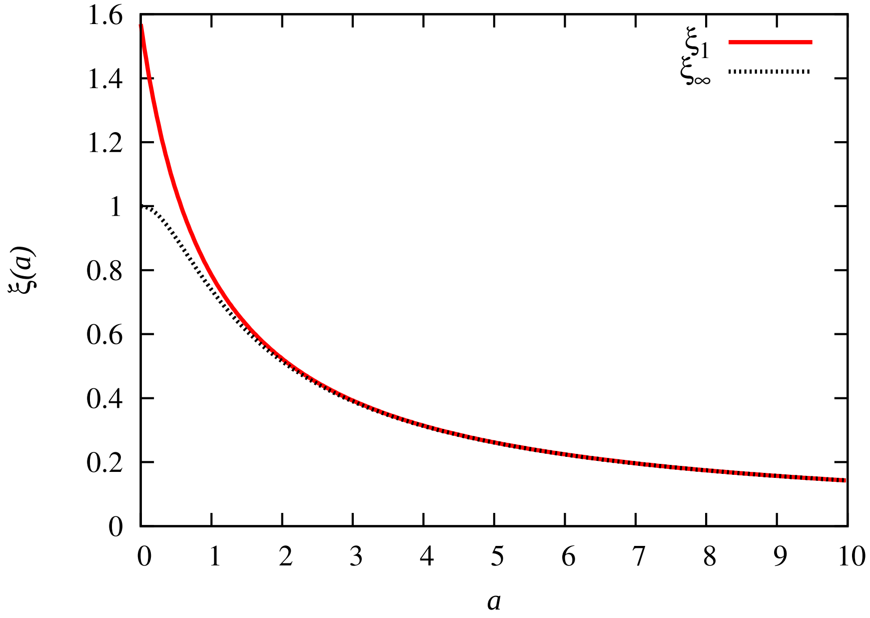

Figure 6.14: Plot of ξ_∞ and ξ_1 as functions of a. $\xi_\infty(a)$ is the smallest positive zero of the function $y(\xi) = \cos(a\xi) - \xi$, while ξ_1 is an approximation of ξ_∞ obtained using just one Newton iteration (Eq. (6.47)). The Newton method converges very quickly: ξ_2 would not be distinguishable from ξ_∞, if it were included in the plot. $a = L\sqrt{\frac{H_\mathrm{P}}{4C}} = \frac{\pi}{2}\sqrt{\frac{H_\mathrm{P}}{H_\mathrm{b}^\infty}}$ represents the hardness of the pinning in the hard layers. If $a \gg 1$ the field required in order to switch the hard layers (H_P) is much higher than the one needed to develop an exchange spring (H_b^∞).

of σ as: $\xi = \sqrt{\frac{C\sigma + H_0}{H_\mathrm{P}}}$. For the ground state ($n = 1$) the problem reduces to finding the smallest positive zero of the function $y(\xi) = \cos(a\xi) - \xi$, where $a = L\sqrt{\frac{H_\mathrm{P}}{4C}}$. This can be done approximatively with the Newton method:

$$\xi_{i+1} = \xi_i - \frac{y(\xi_i)}{y'(\xi_i)} = \frac{a\xi_i \sin a\xi_i + \cos a\xi_i}{a \sin a\xi_i + 1}. \tag{6.47}$$

As a first point we choose $\xi_0 = \frac{\pi}{2a}$ and obtain:

$$\xi_1 = \frac{\pi}{2}\frac{1}{1+a}. \tag{6.48}$$

For large values of a (large pinning) this is already a good approximation, as can be seen in Fig. 6.14. The corresponding value for σ is then:

$$\sigma_1 = \frac{H_\mathrm{P}}{C}\left(\frac{\pi}{2+2a}\right)^2 - \frac{H_0}{C} = \frac{H_\mathrm{b} - H_0}{C},$$

where we have re-defined the bending field as:

$$H_{\mathrm{b}} = H_{\mathrm{P}} \left(\frac{\pi}{2+2a} \right)^2 = C \left(\frac{\pi}{\sqrt{4C/H_{\mathrm{P}}} + L} \right)^2 .$$

The equations for λ and ω are again (6.44). Moreover one sees immediately that in the limit of infinite pinning:

$$H_{\mathrm{P}} \to +\infty, \quad H_{\mathrm{b}} \to H_{\mathrm{b}}^{\infty} = C \left(\frac{\pi}{L} \right)^2 .$$

The finite-pinning bending field can be expressed as:

$$H_{\mathrm{b}} = H_{\mathrm{b}}^{\infty} \left(1 + \frac{2}{L} \sqrt{\frac{C}{H_{\mathrm{P}}}} \right)^{-2} . \tag{6.49}$$

This equation expresses the bending field as a function of the pinning field H_{P}. However, since the pinning is usually due to a magnetic anisotropy in the hard layers, it would be more convenient to relate H_{b} to the anisotropy constants K_1, K_2, $\ldots$, rather than to the more abstract quantity H_{P}. In the next section we prove that this can be done, since, near the bending field, an uniaxial or cubic anisotropy can be well approximated by introducing a pinning field.

6.4.10 Bending field for DyFe_2-YFe_2 multilayers

In the analytical characterisations of exchange spring that we have introduced in the previous sections the pinning of the magnetisation in the hard layers has been modeled by a pinning field H_{P}. Using a constant field H_{P} is certainly a simple way to take the pinning effects into account, but, on the other hand, it may look somewhat artificial and unjustified. In the computer simulations of Sec. 6.3, for example, the pinning in the DyFe_2 hard layers has a more complex origin: it is the result of the combined action of a cubic anisotropy and an antiferromagnetic exchange coupling. The cubic anisotropy holds the Dy moments along an easy axis direction, while the antiferromagnetic coupling holds the Fe moments antiparallel to the Dy moments. Even if the physics in such a system is rather complex, it can be well approximated by the simple single field model that we have studied in the previous sections. Indeed, we now show that, under appropriate assumptions, the physics of the Dy magnetisation and the Fe-Dy antiferromagnetic coupling can be taken into account only through an effective pinning field H_{P} acting on $\vec{M}_{\mathrm{Fe}}$. We begin by writing down the energy density inside the DyFe_2 hard layers:

$$u[\vec{M}_{\mathrm{Fe}}, \vec{M}_{\mathrm{Dy}}] = -\mu_0 \, \vec{M}_{\mathrm{Dy}} \cdot \vec{H} + \varepsilon(\vec{M}_{\mathrm{Dy}}) + J \, \vec{M}_{\mathrm{Fe}} \cdot \vec{M}_{\mathrm{Dy}} - \mu_0 \, \vec{M}_{\mathrm{Fe}} \cdot \vec{H} + A \, (\partial_x \vec{m}_{\mathrm{Fe}})^2 . \tag{6.50}$$

Here $\varepsilon(\vec{M}_{\rm Dy})$ is the energy density for the cubic anisotropy acting on the Dy moments, while $J\,\vec{M}_{\rm Fe}\cdot\vec{M}_{\rm Dy}$ represents the antiferromagnetic exchange coupling. Our goal is to show that, if one is concerned with the Fe moments only, this expression can be reasonably approximated by the pinning field model, whose energy density is,

$$u'[\vec{M}_{\rm Fe}] = -\mu_0\,\vec{M}_{\rm Fe}\cdot(\vec{H}-\vec{H}_P) + A\,(\partial_x\vec{m}_{\rm Fe})^2, \tag{6.51}$$

where $\vec{H} = -\hat{z}\,H$ is the applied field and $\vec{H}_P = \hat{z}\,H_{\rm P}$. is a constant pinning field.

Notice that while equation Eq. (6.51) contains both $\vec{M}_{\rm Fe}$ and $\vec{M}_{\rm Dy}$, Eq. (6.51) contains only $\vec{M}_{\rm Fe}$. We conclude that to reduce the former equation to the latter, we must necessarily reduce the number of degrees of freedom of the system and, in particular, we must remove the freedom on the choice of $\vec{M}_{\rm Dy}$.

The approximation we employ for such a reduction is the following. For a given $\vec{M}_{\rm Fe}$ we calculate the value of $\vec{M}_{\rm Dy}$ which minimises the energy (6.50). Such an expression for $\vec{M}_{\rm Dy}$ is then substituted inside (6.50) to obtain an expression which depends only on $\vec{M}_{\rm Fe}$. Such an approach will lead to an energy density accurate only near the equilibrium or, to be more precise, near any magnetisation configuration which minimises the energy with respect to $\vec{M}_{\rm Dy}$. Fortunately, this is the case we are considering in our analytical model, which is indeed based on a linearisation of the Landau-Lifshitz equation around a static equilibrium configuration. We then can start with the procedure we have just sketched and find the value of $\vec{M}_{\rm Dy}$ which makes $u[\vec{M}_{\rm Fe}, \vec{M}_{\rm Dy}]$ minimum for a given fixed $\vec{M}_{\rm Fe}$. We choose a reference frame such that $\vec{H}$ lies along the negative z axis and $\vec{M}_{\rm Fe}$ lies in the xz plane, as shown in Fig. 6.15. θ and ϕ are spherical coordinates for $\vec{M}_{\rm Dy}$ with respect to the polar axis $-z$, while α is the angle between $\vec{M}_{\rm Fe}$ and the z axis. In terms of these quantities, the vectors $\vec{M}_{\rm Fe}$ and $\vec{M}_{\rm Dy}$ can be expressed as:

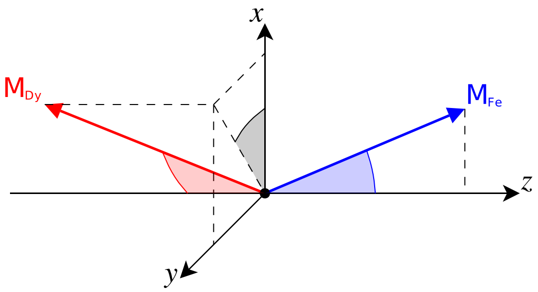

Figure 6.15: The reference frame chosen in the text to write down the energy density in the hard layers.

$$\vec{M}_{\rm Dy} = M_{\rm Dy}\,(\sin\theta\,\cos\phi,\,\sin\theta\,\sin\phi,\,\cos\theta), \qquad \vec{M}_{\rm Fe} = M_{\rm Fe}\,(\sin\alpha,\,0,\,\cos\alpha).$$

By substituting these expressions into Eq. (6.50), we get to:

$$u = -\mu_0 M_{\text{Dy}} H\, \cos\theta + \varepsilon(\theta,\, \phi) + J M_{\text{Dy}} M_{\text{Fe}} (\sin\theta\, \cos\phi\, \sin\alpha - \cos\theta\, \cos\alpha) + \tilde{u}[\vec{M}_{\text{Fe}}],$$

where $\tilde{u}[\vec{M}_{\text{Fe}}]$ contains all the terms of Eq. (6.50) which do not depend on $\vec{M}_{\text{Dy}}$. It can be shown (see Appx C) that, when the angle θ between $\vec{M}_{\text{Dy}}$ and the easy axis is small, the cubic anisotropy energy can be approximated as $\epsilon(\theta,\, \phi) \approx K_1\, \theta^2$, where K_1 is the same coefficient which appears in (2.10). The requirement $\partial_\phi u = 0$, then leads to $-J M_{\text{Dy}} M_{\text{Fe}} \sin\theta\, \sin\phi\, \sin\alpha = 0$ and hence to $\sin\phi = 0$ and $\cos\phi = \pm 1$. We then can rewrite the energy as:

$$u = -\mu_0 M_{\text{Dy}} H\, \cos\theta + K_1\, \theta^2 - J M_{\text{Dy}} M_{\text{Fe}} \cos(\theta \pm \alpha) + \tilde{u}[\vec{M}_{\text{Fe}}].$$

For small angles θ and α,

$$u = \frac{1}{2} \mu_0 M_{\text{Dy}} H\, \theta^2 + K_1\, \theta^2 + \frac{1}{2} J M_{\text{Dy}} M_{\text{Fe}} (\theta \pm \alpha)^2 + \tilde{u}[\vec{M}_{\text{Fe}}], \qquad (6.52)$$

which is accurate up to the third order in θ. The condition $\partial_\theta u = 0$ can now be written as,

$$0 = \mu_0 M_{\text{Dy}} H\, \theta + 2K_1 \theta + J M_{\text{Dy}} M_{\text{Fe}} (\theta \pm \alpha).$$

from which θ can be found as a function of α:

$$\theta = \mp \frac{\alpha}{1+B}, \qquad \text{where}\, B = \frac{\mu_0 M_{\text{Dy}} H + 2K_1}{J M_{\text{Dy}} M_{\text{Fe}}} \approx \frac{2K_1}{J M_{\text{Dy}} M_{\text{Fe}}},$$

where we have assumed $2K_1 \gg \mu_0 M_{\text{Dy}} H$. We can now remove any dependency on θ in Eq. (6.52):

$$\begin{aligned} u &= \left[\mu_0 M_{\text{Dy}} H + 2K_1 + J M_{\text{Dy}} M_{\text{Fe}} B^2\right] \frac{\alpha^2}{2\,(1+B)^2} + \tilde{u}[\vec{M}_{\text{Fe}}], \\ &= \frac{J M_{\text{Dy}} M_{\text{Fe}}}{1 + B^{-1}} \frac{\alpha^2}{2} + \tilde{u}[\vec{M}_{\text{Fe}}], \qquad (6.53) \end{aligned}$$

This result can now be compared against the simple pinning field model of Eq. (6.51), which for small angles α, becomes:

$$u'[\vec{M}_{\text{Fe}}] = \text{const.} + \mu_0 M_{\text{Fe}} H_{\text{P}}\, \frac{\alpha^2}{2} + \tilde{u}[\vec{M}_{\text{Fe}}]. \qquad (6.54)$$

Eq. (6.53) reduces to Eq. (6.54) (except for an additive constant) when,

$$\mu_0 M_{\text{Fe}} H_{\text{P}} = \frac{J M_{\text{Dy}} M_{\text{Fe}}}{1 + B^{-1}} \Longrightarrow H_{\text{P}} = \frac{1}{\mu_0 M_{\text{Fe}} \left(\frac{1}{2K_1} + \frac{1}{J M_{\text{Fe}} M_{\text{Dy}}} \right)}.$$

This expression for H_P behaves as one would expect: when one of the two interactions becomes infinitely strong it "disappears", leaving only the other interaction. However, when both interactions become infinitely strong, H_P becomes infinite, as it should! An analogy could be made with the compressibility of two connected springs: when one of the two springs is incompressible then the compressibility of the whole system is given by the compressibility of the other spring, while, when both springs are incompressible, also the whole system becomes incompressible. We can finally insert the expression of H_P into Eq. (6.49), obtaining:

$$H_\mathrm{b} = H_\mathrm{b}^\infty \left(1 + \frac{2}{L}\sqrt{2A\left(\frac{1}{2K_1} + \frac{1}{JM_\mathrm{Fe}M_\mathrm{Dy}}\right)}\right)^{-2}. \tag{6.55}$$

We note that we may rewrite the bending field of a finite-pinning exchange spring system starting from the infinite pinning formula (6.6) and replacing:

$$L \to L + 2\sqrt{2A\left(\frac{1}{2K_1} + \frac{1}{JM_\mathrm{Fe}M_\mathrm{Dy}}\right)}. \tag{6.56}$$

The expression above may give a rough idea about the extent to which the exchange spring penetrates inside the hard layers. An interesting feature can be noticed: the penetration depth does not depend on L, the thickness of the soft layer.

To validate Eq. (6.55) we consider again the system presented in Sec. 6.3. From the simulation we extrapolated a value for the bending field $H_\mathrm{b}|_\mathrm{sim} = (3.947 \pm 0.024)\,\mathrm{T}$ (see caption of Fig. 6.8). Eq. (6.55) gives $H_\mathrm{b}|_\mathrm{theory} = 3.952\,\mathrm{T}$. The theoretical value differs by less than 0.13 % from the value which was deduced numerically. The agreement is really quite good, but it consists of just one single comparison between two numbers. It may then be a mere coincidence! To make sure this is not the case, we redo the simulations of Sec. 6.3 changing some parameters just to have a second opportunity to validate the theory. We change the cubic anisotropy constant from $K_1 = 33.9 \times 10^6\,\mathrm{J/m^3}$ to $K_1 = 20.0 \times 10^6\,\mathrm{J/m^3}$ and the antiferromagnetic exchange coupling from $J = 2 \times 10^{-4}\,\mathrm{N/A^2}$ to $J = 10^{-4}\,\mathrm{N/A^2}$. All the others parameters are left unchanged, while the simulations are repeated following the same procedure used in Sec. 6.3. We get $H_\mathrm{b}|_\mathrm{theory} = (3.643 \pm 0.018)\,\mathrm{T}$ while Eq. (6.55) gives $H_\mathrm{b}|_\mathrm{theory} = 3.625\,\mathrm{T}$. The deviation between the two is less than 0.5 %, confirming that Eq. (6.55) provides a quite accurate estimate of the bending field, especially if compared with the rigid pinning formula of Eq. (6.6), which overestimates the bending field by ∼ 30 %.

6.5 Summary

In this chapter we studied both the static and the dynamic properties of trilayer exchange spring systems, focusing in particular on a $DyFe_2/YFe_2/DyFe_2$ trilayer system. We used computer simulations and introduced analytical models in order to investigate and understand the magnetisation dynamics near the bending field and found that the average magnetisation in the soft layer approaches equilibrium moving in spiral trajectories with frequency and damping which become minima for values of the applied field near to the bending field. We concluded that the magnetisation reacts in an enhanced way near the bending field and discussed the importance of this characteristic for maximising spin transfer torque effects. The effects of spin polarised currents were then taken into account first in an analytical model and later in computer simulations. We found that, below the bending field, the application of a current changes the frequency and the damping of the oscillations, but does not change the shape of the trajectories of the average magnetisation. Unfortunately a high current is required in order to obtain significant effects and this was attributed to the fact that below the bending field the configuration of the magnetisation is almost uniform and thus gives rise to a weak spin transfer torque. We concluded the chapter presenting an accurate calculation of the bending field, which takes into account the strength of the cubic anisotropy, the strength of the Fe-Dy antiferromagnetic coupling and the penetration of the exchange spring inside the hard layers. Throughout all the chapter we found good agreement between the results from the simulations and from the analytical models.

Chapter 7

Spin-polarised currents in exchange spring nanopillars

7.1 Introduction

In the previous chapter we investigated exchange spring systems and focused on the dynamics near the bending field, in the hope of finding relevant response to an applied electric current. We found that if, on the one hand, the magnetisation exhibits enhanced response to external stimuli near the bending field, on the other, in such an applied field regime the magnetisation is almost uniform, leading to minimal spin transfer torque. We concluded that such a particular choice of exchange spring system was not the most appropriate in order to investigate and maximise spin transfer torque effects. Nevertheless, exchange spring systems have a remarkable feature: the interplay between the strong anisotropy of the hard materials and the soft-hard exchange coupling, can give rise to artificial domain walls whose shape and length can be controlled in two ways: at the engineering phase, by selecting suitable geometry and material composition, and later in the laboratory, with the application of an external field (a domain wall is developed when the applied field exceeds the bending field).

In this chapter we give an example of how this feature can be exploited in order to build a system where the spin transfer torque effects are enhanced and play an important role. We first explain the idea which guided us to the design of the exchange spring nanopillar which is investigated in this chapter: find a system whose ground state is degenerate (i.e. whose energy is minimum for a whole continuous trajectory of magnetisation configurations).

The results presented in this chapter have been published in the Journal of Applied

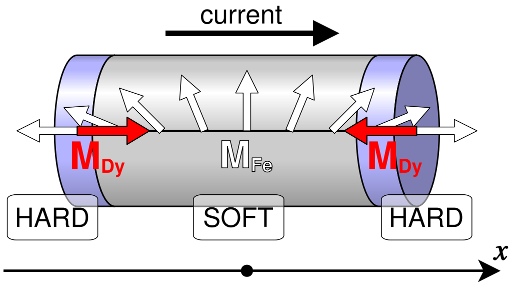

Figure 7.1: A sketch of the nanopillar which is discussed in the text (not to scale). Dysprosium moments (white arrows) pin the iron moments (black arrows) at the borders of the soft layer.

Physics [55].

7.2 The system

Consider a system whose ground state energy is degenerate: it has infinitely many different equilibrium configurations, which all have the same minimal energy and form a continuous curve in the phase space. This system can be “dragged” through this curve, changing its configuration from one equilibrium state to another and this can be achieved “easily”, because there is no energy barrier between them. In such a system, an electric current may find a very favourable situation to fully manifest its effects.

The idea is very simple, but can serve as a guideline to develop micromagnetic systems where spin-transfer-torque effects are maximised. In this chapter we discuss a possible example of such a system. We study a trilayer exchange spring system in the form of a cylindrical nanopillar, where a central magnetically soft layer is sandwiched between two magnetically hard layers, as shown in Fig. 7.1. The system materials are chosen in the following way: YFe_2 for the soft layer and $DyFe_2$ for the two hard layers. This choice allows us to study the system with a model similar to the one used in Ch. 6. Regarding the geometry, the diameter of the cylindrical nanopillar is 10 nm, while the thicknesses of the hard and soft layers are 5 and 40 nm, respectively.

As seen in the previous chapter, Yttrium has negligible magnetic moment and only two species of atoms contribute to the magnetisation of the system: the first one, iron (Fe), is present in all the three layers, the second one, dysprosium (Dy), is present only in the two hard layers. Neighboring iron moments are exchange coupled, throughout all the hard and soft layers and across the hard-soft interfaces. This coupling favours the alignment of the magnetisation of iron throughout the entire nanopillar. This alignment is however broken, because the magnetisation of iron in the two hard layers is pinned along opposite directions, as shown in Fig. 7.1. We remind the reader, that the pinning of the iron moments is the result of the joint actions of two strong interactions: the cubic anisotropy of DyFe_2, which pins the dysprosium moments along an easy axis direction, and the anti-ferromagnetic coupling between Dy and Fe, which transmits this pinning to the iron moments of the hard layers.

Among all the interactions which we take into account, the cubic anisotropy of DyFe_2 is the only one which is not symmetric under rotations around the axis of the nanopillar. However in the case we are considering, where there is no applied field and the soft layer is relatively thick, the dysprosium moments keep their direction well aligned with the one they initially have and the degeneracy of the ground state is well preserved, as we will see from the results of the computer simulations. This means that configurations which differ by a rotation around the x axis have almost the same energy. Then if the applied current wants to rotate the whole magnetisation around the x axis, nothing will oppose to its action, since this is a constant-energy trajectory.

7.3 The model

Since the density of iron atoms and their position in the lattice structure is the same for DyFe_2 and YFe_2 (they both crystallise in Laves phase structures), we use a single magnetisation vector $\vec{M}_{\mathrm{Fe}}$ to describe the magnetic configuration of iron in all the three layers. The configuration of dysprosium is modeled by another magnetisation field $\vec{M}_{\mathrm{Dy}}$ which is defined over the hard layers only. The model is similar to the one-dimensional model used in Ch. 6, extended to three dimensions (the stray field is calculated using the hybrid FEM/BEM method [30, 29]). We also consider the same temperature (100 K) and the same material parameters: the moment densities of iron (in both DyFe_2 and YFe_2) and dysprosium are $\|\vec{M}_{\mathrm{Fe}}\| = 0.55 \times 10^6$ A/m and $\|\vec{M}_{\mathrm{Dy}}\| = 1.73 \times 10^6$ A/m, respectively; the easy axes for the anisotropy are $\hat{u}_1 = (0, 1, 1)/\sqrt{2}$, $\hat{u}_2 = (0, -1, 1)/\sqrt{2}$ and $\hat{u}_3 = (1, 0, 0)$, and the coefficients are $K_1 = 33.9 \times 10^6\ \mathrm{J/m^3}$, $K_2 = -16.2 \times 10^6\ \mathrm{J/m^3}$, $K_3 = 16.4 \times 10^6\ \mathrm{J/m^3}$. The effects of the electric current are modelled using Eq. (3.13), the Zhang-Li correction to the Landau-Lifshitz-Gilbert equation. Similarly to Ch. 6, we assume that only the iron moments interact with the spin of the conduction electrons: the magnetic electrons in the 4f orbitals of dysprosium are strongly localised at the ion core and their interaction with the conduction electrons should be negligible. In the simulation the damping parameter is chosen to be $\alpha = 0.02$; the current density is assumed to be fully polarised ($P = 1$) and ξ, the ratio between the exchange relaxation time and the spin-flip relaxation time, is taken to be $\xi = 0.01$. The Oersted field and the effects of Joule heating are ignored.

7.4 Results

For the micromagnetic simulations we use *Nmag*, the software package which we have developed in our group [68]. The cylindrical nanopillar is modelled by a three-dimensional unstructured mesh and first order FEM is used to discretise the space. In this case FEM is preferable with respect to finite differences, because it allows a better representation of the cylindrical geometry. Finite differences would introduce artifacts in the discretisation of the rounded surface of the nanopillar.

The initial magnetizations $\vec{M}_{\mathrm{Fe}}$ and $\vec{M}_{\mathrm{Dy}}$ are obtained by letting the system relax to one of its degenerate equilibrium configurations. The system then evolves from this configuration ($t = 0$) up to $t = 10.5\,\mathrm{ns}$. The dynamics of $\langle\vec{M}_{\mathrm{Fe}}\rangle$, the iron magnetisation averaged over all the nanopillar, is studied in Fig. 7.2. For simplicity we identify four points on the time axis: A at 0 ns, B at 3.5 ns, C at 7 ns and D at 10.5 ns. The time axis is then subdivided into three regions AB, BC and CD. The applied current density $\vec{j}$ is uniform and constant in each of these three time intervals. In particular it is directed along the axis of the cylinder: $\vec{j} = j\,\hat{x}$, with $j = 10^{11}\,\mathrm{A/m^2}$ in AB, $j = 0$ in BC and $j = -10^{11}\,\mathrm{A/m^2}$ in CD. We remind the reader that the applied field is always zero, throughout all the simulation.

The graph in Fig. 7.2 shows the behaviour of the components of $\langle\vec{M}_{\mathrm{Fe}}\rangle$: in region AB the current produces a precession of the whole magnetisation of the system around the x axis. This precession is accompanied by a movement — and consequent compression — of the artificial domain wall in the direction of the electron flow (negative x direction), which reflects in an increase of the x component of $\langle\vec{M}_{\mathrm{Fe}}\rangle$. Such an effect may be explained with a current-induced motion of the artificial domain wall. Current-induced motion is a well known effect for domain walls in nanowires: it has been observed experimentally and has been proved analytically [18, 20, 21].

In the time interval AB the current pumps energy into the system, which is stored in the compression of the domain-wall. In the time interval BC the current is switched off and this energy is gradually released: the domain-wall decompresses, restoring the

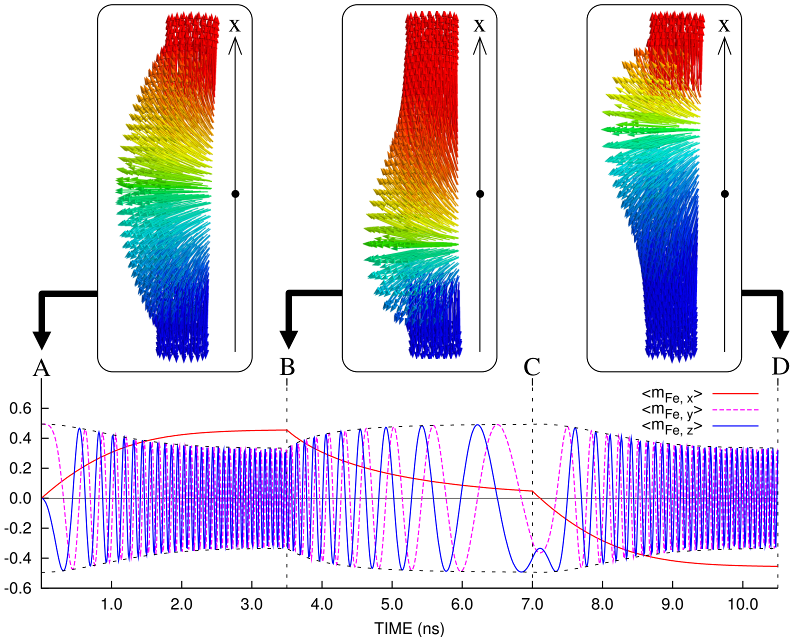

Figure 7.2: The evolution in time of the three components of $\langle \vec{m}_{\mathrm{Fe}} \rangle = \langle \vec{M}_{\mathrm{Fe}} / \|\vec{M}_{\mathrm{Fe}}\| \rangle$, the normalised magnetisation of iron averaged over all the nanopillar. The three boxes above the graph show the configuration of $\vec{M}_{\mathrm{Fe}}$ at $t = 0$, $t = 3.5\,\mathrm{ns}$ and $t = 10.5\,\mathrm{ns}$.

configuration it had at time $t = 0$. Finally, during the time interval CD the system behaves in a way which is symmetrical to the one observed in AB: $\langle M_{\mathrm{Fe},x} \rangle$ rotates in the opposite direction and the wall is compressed in the positive x direction, leading to negative values for $\langle M_{\mathrm{Fe},x} \rangle$.

Expressing $\langle \vec{M}_{\mathrm{Fe}} \rangle$ in spherical coordinates with x chosen as the polar axis, we obtained the precession angle $\phi(t)$ of $\langle \vec{M}_{\mathrm{Fe}} \rangle$ around the x axis as a function of time t. We computed the time derivative $\omega(t) = \phi'(t)$ to obtain the precession frequency as a function of time. The result is shown in Fig. 7.3. The sign of $\omega(t)$ depends on the sense of rotation around the x axis. This graph shows that the applied current $j = \pm 10^{11}\,\mathrm{A/m^2}$, produces a precession motion with frequency around 14 GHz, in the microwave frequency range. The frequency seems to be related to the compression of the domain wall: it increases rapidly when $\langle M_{\mathrm{Fe},x} \rangle$ increases and stabilises when also $\langle M_{\mathrm{Fe},x} \rangle$ does.

The accuracy of the discretisation of space has been verified by increasing the number of mesh elements (from 4129 to 19251), obtaining differences in the precession frequency at 3.5 ns lower than 1.2 %.

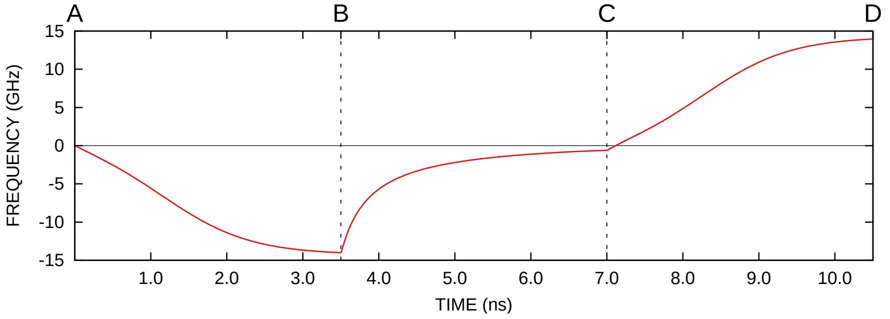

Figure 7.3: The time dependence of the frequency ω for the precession of $\langle \vec{M}_{\mathrm{Fe}} \rangle$ around the x axis. The sign of ω is related to the sense of rotation.

7.5 Discussion

The physics we studied in this work has not been reported — to our best knowledge — in previous published works. While the current-driven motion of domain wall has been intensively studied in recent publications [18, 87, 20], the compression and concurrent precession has not been reported nor predicted previously. The system we presented may be interesting for applications as a nano-sized microwave generator which can operate without external applied field and can be driven by a direct current. Deeper investigations are, however, needed in order to better understand the physics of the system and to assess the importance of the assumptions we made to get to these results. In particular, the model we presented does not take into account some effects which complicate the physics of real systems. The imperfections of the geometry and the impurities in the materials can break the cylindrical symmetry. The effect of such imperfections is difficult to predict.

The size of the sample was chosen to speed up the simulation. However we expect a similar precessional dynamics in nanopillars with greater radii. Also the materials could have been chosen differently and the $DyFe_2$ anisotropy could have been well approximated by an infinite pinning on the iron moments, resulting in a simplification of the model. However this approximation would have removed the only source of symmetry breaking, besides the irregularity of the unstructured mesh. To conclude we remark that a symmetry breaking could be introduced on purpose to obtain bistable systems, where the current may be used to switch the magnetisation between two states.

7.6 Summary

In this chapter we studied the current driven dynamics of the magnetisation in a cylindrical exchange spring nanopillar made of one soft layer sandwitched between two hard layers. We assumed that the magnetisation in the two hard layers points along opposite directions with the consequence that a domain wall is developed inside the soft layer. We found that a current applied along the nanopillar axis induces the domain wall to compress along the direction of the electron flow and — at the same time — it induces the domain wall to precess around the axis of the nanopillar. When a direct current (DC) is applied, the system reaches a stationary equilibrium, where the magnetisation rotates with constant frequency and where the amount of energy pumped in by the electric current is totally dissipated by the damping effects. The system may thus be exploited to obtain a microwave generator capable of operating without any external applied field and with emission frequency controlled by a DC.

Chapter 8

Electric current flowing through a constrained domain wall

8.1 Introduction

The interaction between electric currents and domain walls in ferromagnetic nanowires has been the subject of intensive study in recent years. Experiments have shown that a spin polarised current can produce a domain wall movement in the direction of the electron flow [88, 18, 87, 20]. This effect has been investigated analytically and numerically [89, 23, 90]. In the previous chapter we studied the case where a domain wall occurs inside a ferromagnetic nanopillar as a consequence of the pinning of the magnetisation at the nanopillar ends. The situation is similar to the one which occurs for a domain wall in a nanowire, with an important difference: the domain wall is pinned and cannot translate freely along the nanopillar. For such a system one may expect a compression of the domain wall, rather than a translation. We have seen that micromagnetic simulations confirm this expectation and show that the applied current produces a compression of the domain wall in the direction of the electron flow. More surprisingly the system reaches a stationary equilibrium characterised by a rotation of the compressed domain wall around the nanopillar axis with frequency which is constant in time and lies within the microwave frequency range. This behaviour is not found for domain walls in nanowires and suggests novel technological applications: such a system may be used to obtain microwaves emission from a DC electric current without the need for an external magnetic field.

In this chapter, we study how the rotation frequency depends on the applied current density and on the nanopillar length. We first present the results of three dimen-

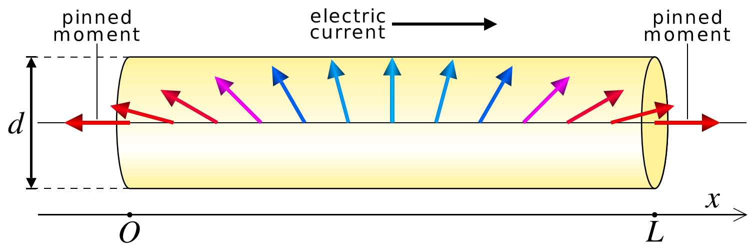

Figure 8.1: A sketch of the system. The arrows on the cylinder axis represent the magnetisation, pinned in opposite directions at the nanopillar ends.

sional and one dimensional micromagnetic simulations. We then introduce an analytical model and find two current regimes: the low current regime, where the frequency depends linearly on the current density, and the high current regime, where the dependence becomes quadratic. We derive approximate formulae for the frequency in these two regimes and find good agreement with the results from the simulations. The analytical model supports the numerical results and gives more insight on the physics of the system. Parts of this chapter have been published in Physical Review B [56].

8.2 The system

The system under investigation is a ferromagnetic nanopillar in the shape of a cylinder, as shown in Fig. 8.1. The magnetic moments at the right and left faces of the cylinder are assumed to be pinned, pointing to the right at the right face and to the left at the left face. As a consequence, a domain wall is developed. The system may thus approximate the situation we considered in Ch. 7, where a nanopillar made of a magnetically soft material was sandwiched between two magnetically hard layers and the pinning was provided by the exchange coupling at the soft-hard interfaces. In this context however we do not make any assumptions on the origin of the pinning, which can be achieved in other ways. One example is given in Fig. 8.2, which shows a ferromagnetic body, made by two regions connected through a small constriction: a domain wall is developed in the constriction, when the wider regions are magnetised in opposite directions [91, 92].

In this work we study how the constrained domain wall reacts to a uniform and constant electric current flowing along the axis of the nanopillar. Both the simulations and the analytical investigations we present are based on a micromagnetic model, where the interaction between the spins of the conduction electrons and the magnetisation is

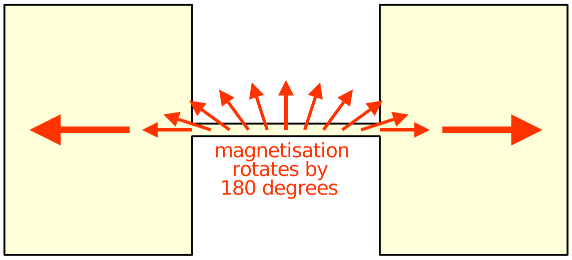

Figure 8.2: A constrained domain wall can develop inside a ferromagnetic body as a consequence of its geometry. Here two square films are magnetised in opposite directions. As a consequence, the magnetisation inside the channel which connects the two bodies is forced to twist by 180 degrees, thus developing an “artificial” domain wall [91, 92].

taken into account using the Zhang and Li correction [23] to the Landau-Lifshitz-Gilbert equation, which we presented and discussed in Ch. 3. The dynamics of the system then follows Eq. (3.12), where the effective field $\vec{H}$ receives two main contributions: one from the exchange interaction, the other from the magnetostatic interaction. The exchange interaction tries to keep neighboring moments aligned. The exchange field is $\vec{H}_{\mathrm{exch}} = C\,\partial_x^2\vec{m}$, where $C = \frac{2A}{\mu_0 M_{\mathrm{sat}}}$, A is the exchange coupling constant of the material and $\partial_x^2 \equiv \frac{\partial^2}{\partial x^2}$. The magnetostatic interaction mainly tries to align $\vec{M}$ with the axis of the nanopillar (when its length is much greater than its radius) thus reducing the magnetic surface charges.

The model does neither include the effects of Joule heating nor the effects of the Oersted field. We discuss these assumptions in Sec. 8.6.

8.3 Three dimensional micromagnetic simulations

For the micromagnetic simulations we use *Nmag* [68], the finite element method (FEM) micromagnetic simulation package which we developed. The cylindrical nanopillar is modelled by a three dimensional unstructured mesh and first order FEM is used to discretise the space. The time evolution of the magnetisation is calculated using equation (3.13), except for the sites which lie on the left and right faces of the nanopillar. For these sites we assume $\partial_t\vec{m} = 0$, which corresponds to infinitely strong pinning on the magnetisation. The magnetostatic field is calculated using the hybrid FEM/BEM method [30, 29]. We use material parameters of permalloy: $M_{\mathrm{sat}} = 0.8 \times 10^6\,\mathrm{A/m}$, $A = 1.3 \times 10^{-11}\,\mathrm{A/m}$ and $\xi = 0.01$. The damping constant is chosen to be $\alpha = 0.02$.

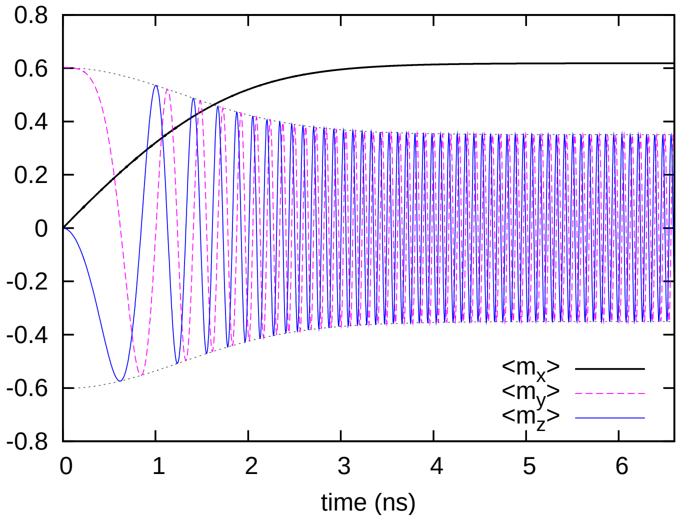

Figure 8.3: The evolution of the components of the average normalised magnetisation $\langle \vec{m} \rangle = \left\langle \vec{M} \right\rangle / M_{\mathrm{sat}}$ as a function of time. The nanopillar length is $L = 40\,\mathrm{nm}$.

This value was estimated for permalloy in a previous work[93]. The applied magnetic field is zero, for all the simulations presented in this chapter.

We first consider a nanopillar with length $L = 40\,\mathrm{nm}$ and diameter $d = 20\,\mathrm{nm}$ and prepare a simulation with the aim of verifying that the system we are considering in this study can give results similar to those obtained in Ch. 7 for the trilayer exchange spring nanopillar. The simulation starts from an initial magnetisation configuration, which is obtained by preliminarily relaxing the system with $j_{\mathrm{P}} = 0$ and is shown in Fig. 8.4-a. A polarised current with density $j_{\mathrm{P}} = Pj = 10^{11}\,\mathrm{A/m}^2$ is then applied at time $t = 0$ along the positive x direction, meaning that the conduction electrons flow in the opposite direction. The procedure is similar to the one employed in Ch. 7.

The simulation shows that the domain wall compresses along the direction of the electron flow. In Fig. 8.3 the components of the normalised spatially averaged magnetisation $\langle \vec{m} \rangle = \left\langle \vec{M} \right\rangle / M_{\mathrm{sat}}$ are plotted as functions of time up to 6.6 ns. The x component of $\langle \vec{m} \rangle$ is initially zero, reflecting the symmetry of the initial configuration (Fig. 8.4-a) for inversions $x \to -x$. The current gradually pumps energy into the system and compresses the domain wall against the left face of the nanopillar (Fig. 8.4-b). In the opposite side of the nanopillar the magnetisation aligns along the positive x axis, resulting in an increase of $\langle m_x \rangle$. The compression is accompanied by a rotation of the whole domain wall around the axis of the nanopillar, as can be seen clearly by looking at behaviour of the y and z components of $\langle \vec{m} \rangle$ in Fig. 8.3. To obtain the rotation

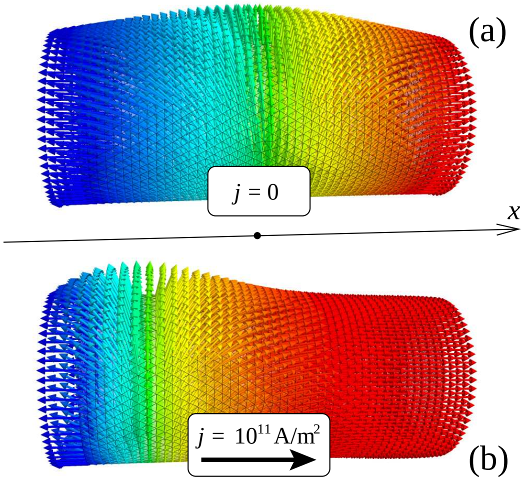

Figure 8.4: The magnetisation configuration for the simulation of Fig. 8.3 is shown at $t = 0\,\text{ns}$ (a) and $t = 6.6\,\text{ns}$ (b).

frequency we express $\langle\vec{m}\rangle$ in spherical coordinates where x is chosen as the polar axis. The frequency is then calculated numerically as $\nu = |\partial_t\phi|/2\pi$, where ϕ is the azimuth angle. In the case we are considering here, where the current points in the direction of the positive x axis, the sign of $\partial_t\phi$ is negative and indicates a left-handed rotation around the same axis (or equivalently a right-handed rotation around the negative x axis, which is actually the compression direction). The rotation frequency is initially zero and increases monotonically towards a maximum asymptotical value ν_f, as shown in Fig. 8.5.

To determine ν_f we let the simulation proceed up to the point where the variation in time of the frequency becomes lower than a given threshold. In particular we stop the simulation when $\Delta\nu/\Delta t$ becomes lower than 0.01 GHz/ns. The variation $\Delta\nu/\Delta t$ is calculated with $\Delta t = 100\,\text{ps}$. The simulation then proceeds up to $t_\text{f} = 6.6\,\text{ns}$ and the asymptotical frequency is found to be $\nu_\text{f} \approx \nu(t = t_\text{f}) = 11.3\,\text{GHz}$ (at $11\,\text{ns}$ the frequency is only 0.004 GHz higher, which corresponds to an increase of $0.04\,\%$).

The asymptotical dynamics is characterised by a rotation around the x axis, without deformation of the domain wall. In such a state, the total energy of the system is constant in time and hence the energy dissipated by the damping term must be exactly balanced by the energy pumped in by the applied current. The results obtained so far confirm that, even if the system we are considering in this chapter is simpler than the exchange spring nanopillar investigated in Ch. 7, it shares most of its physics.

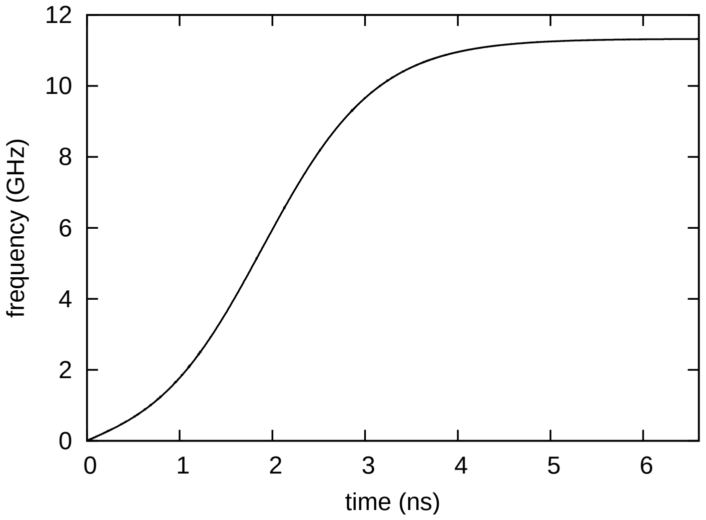

Figure 8.5: The time dependence of the frequency for the rotation of the domain wall around the x axis for a three dimensional micromagnetic simulation of a nanopillar with $L = 40\,\text{nm}$.

Further simulations are performed to find the exact dependence of the frequency on the polarised current density j_P and on the length of the nanopillar L. A different mesh is considered for each different value of L. All the meshes are obtained meshing cylinders with diameter $d = 20\,\text{nm}$ and are generated such that their simplices have edge length lower than 2.6 nm (on average their edges are around 1.2 nm long).

The graph in Fig. 8.6 shows the asymptotic frequency ν_f obtained repeating the simulation for $j_\text{P} = 1, 2, 4, \ldots, 18, 20 \times 10^{10}\,\text{A/m}^2$ and for $L = 20, 25, \ldots, 45\,\text{nm}$. The figure shows that while the frequency changes considerably with the current density j_P, there are small differences between the curves obtained for different nanopillar lengths L. In particular the curves for different values of L overlap, showing that this parameter has different effects for different current regimes: for currents around $10^{10}\,\text{A/m}^2$, the highest rotation frequency is reached by the shortest nanopillar, while for currents around $2 \times 10^{11}\,\text{A/m}^2$ the highest frequency is reached by the longest nanopillar.

8.4 One dimensional micromagnetic simulations

We repeat the simulations discussed in Sec. 8.3 for a simplified model, where the nanopillar is represented by a one dimensional magnetic string. Such a study has a two-fold purpose: on the one hand, it provides data for a comparison with the three-dimensional model, which allows to better understand the effects of the nanopillar shape

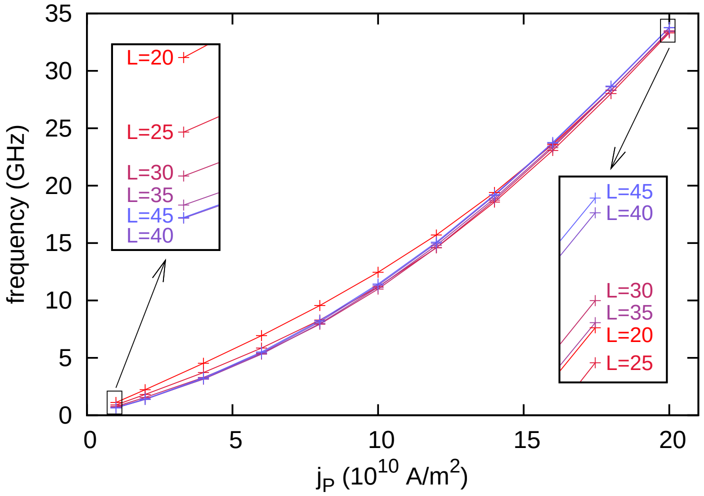

Figure 8.6: The frequency as a function of j_{P} for different nanopillar lengths L, as obtained from three dimensional micromagnetic simulations.

and size. On the other hand, it gives insight on the limitations of one dimensional models, such as the one presented in Sec. 8.5.

For the one dimensional simulations we use the same material parameters and the same procedure as in Sec. 8.3. The three dimensional meshes are, however, replaced by one dimensional meshes with 0.5 nm spacing between neighboring nodes. This one dimensional model neglects the inhomogeneities of the magnetisation in the plane orthogonal to the nanopillar axis and — more importantly — it neglects the contribution of the magnetostatic field.

The results of the simulations are shown in Fig. 8.7. We study the system for $L = 20, 25 \ldots, 60\,\mathrm{nm}$ and for the same values of j_{P} as in Sec. 8.3. The curves for different nanopillar lengths are more clearly spaced with respect to the three dimensional case and show that to a longer nanopillar corresponds a lower rotation frequency. This result is reasonable for such a one dimensional system, where the width of the domain wall is just L: to a smoother change of the magnetisation corresponds a reduced spin transfer torque effect. In the three dimensional system, things are different. The magnetostatic field pulls the magnetisation along the axis of the nanopillar to reduce the magnetic charges at the surface. This is an additional pinning effect which keeps the width of the domain wall from growing for larger values of L. In other words, in the three dimensional system the domain wall width does not depend on L, if L is large enough. Then the frequency does not depend on L either.

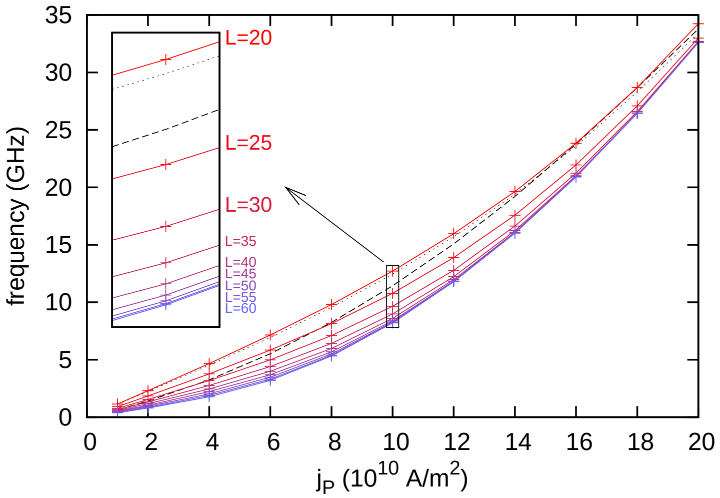

Figure 8.7: The frequency as a function of j_{P} for different nanopillar lengths L, as obtained from one dimensional micromagnetic simulations. The dotted and dashed curves show the results obtained for the three dimensional system (Fig. 8.6) in the case $L = 20$ and $L = 45$, respectively.

In fig. 8.7 we see that the frequencies for $L = 20\,\mathrm{nm}$ obtained in the one dimensional model are close to the ones obtained in the full three dimensional model. This seems to suggest that the magnetostatic effects become less important in shorter nanopillars.

8.5 The analytical model

We investigate the system with a one-dimensional analytical micromagnetic model. The purpose of such a study is to support the micromagnetic simulations and to give a better understanding of the physics of the system. The model does not include the magnetostatic field and assumes it does not qualitatively affect the physics of the system. We begin by writing equation (3.13) in spherical coordinates:

$$\begin{cases} \partial_{\tau'}\theta = 2\cos\theta\,\partial_u\theta\,\partial_u\phi + \sin\theta\,\partial_u^2\phi + \\ \quad + \alpha\,\left[\partial_u^2\theta - \sin\theta\cos\theta\,(\partial_u\phi)^2\right] + \\ \quad + V a\,\partial_u\theta + V\overline{a}\sin\theta\,\partial_u\phi & (8.1\mathrm{a}) \\ \partial_{\tau'}\phi\,\sin\theta = \alpha\,\left[2\cos\theta\,\partial_u\theta\,\partial_u\phi + \sin\theta\,\partial_u^2\phi\right] \\ \quad - \partial_u^2\theta + \sin\theta\cos\theta\,(\partial_u\phi)^2 - \\ \quad - V\overline{a}\,\partial_u\theta + V a\sin\theta\,\partial_u\phi & (8.1\mathrm{b}) \end{cases}$$

Only dimensionless quantities appear in this equations: $u = \frac{x}{L}$, $\tau' = \frac{\gamma' C}{L^2}\,t$, $V = \frac{L}{\gamma C}\,v$. We want the magnetisation to point to the left at the left boundary and to the right at the right boundary:

$$\theta(u=0) = \pi, \qquad \theta(u=1) = 0, \tag{8.2}$$

which are boundary conditions for our system of differential equations. When the current is zero, $V = 0$, the equilibrium (such that $0 = \partial_{\tau'}\theta = \partial_{\tau'}\phi$) is obtained for:

$$\theta(u) = \pi(1-u), \qquad \phi(u) = \text{const}, \tag{8.3}$$

as can be seen with a substitution in (8.1). For $V > 0$, computer simulations show that the system approaches a stationary equilibrium where the whole magnetisation rotates with constant frequency around the axis of the nanopillar. We then investigate the case where there is no further compression of the domain wall, while it could still rotate with constant angular velocity around the x-axis:

$$\partial_{\tau'}\theta = 0, \qquad \partial_{\tau'}\phi = \Omega' = \text{const}. \tag{8.4}$$

The rotation frequency can be obtained from Ω' through the relation $\nu_{\mathrm{f}} = \frac{\gamma' C}{2\pi\, L^2}\,|\Omega'|$.

As a first try to find such a solution we assume $\partial_u\phi = 0$ and find the corresponding compression profile from Eq. (8.1a):

$$\alpha\,\partial_u^2\theta + V a\,\partial_u\theta = 0.$$

Solving this equation we get:

$$\partial_u\phi = 0, \qquad \theta(u) = \pi\,\frac{e^{\lambda(1-u)} - 1}{e^{\lambda} - 1},$$

where $\lambda = \frac{Va}{\alpha}$. However this is not a solution of (8.1), as can be easily verified with a substitution in the second equation of this system:

$$-\partial_u^2\theta - V\bar{a}\,\partial_u\theta \neq \Omega'\,\sin\theta.$$

We conclude that $\partial_u\phi$ cannot be neglected. It is then important to understand the role of $\partial_u\phi$, the torsion of the domain wall produced as an effect of the flow of the electric current.

We point out that the rotation is a consequence of the compression of the domain wall and — in this sense — can be thought to be an indirect effect of the spin transfer torque. This can be seen clearly by considering the zero-current equilibrium configuration (8.3) and looking at the derivatives of θ and ϕ with respect to the reduced time τ', when a current density is immediately applied (this is the situation which occurs at $t = 0$ in the simulations). Eq. (8.1a) becomes $\partial_{\tau'}\theta = -V a\pi$, which suggests that a compression of the domain wall is going to take place. Eq. (8.1b) becomes $\sin\theta\,\partial_{\tau'}\phi = V\overline{a}\pi$. We have found a direct contribution to the rotation of the domain wall. This contribution however is suppressed by the factor $V\overline{a} \sim -5\times10^{-4}$, which is rather small for the materials and the range of current densities we are interested in ($j = 10^{11}\,\mathrm{A/m^2}$, $V \sim 5\times10^{-2}$). We conclude that the domain wall initially compresses without significant rotation and torsion. The compression however leads to non vanishing values for the term $\partial_u^2\theta$ and this in turn requires non vanishing values for $\sin\theta\,\partial_{\tau'}\phi$, as can be seen by looking at (8.1b). In summary, the compression of the domain wall (i.e. $\partial_u^2\theta \neq 0$) produces a torsion and rotation of the domain wall (i.e. $\sin\theta\,\partial_{\tau'}\phi \neq 0$).

We now proceed by rearranging (8.1) and imposing (8.4):

$$\begin{cases} -\Omega\,\sin\theta = \partial_u^2\theta - \sin\theta\cos\theta\,(\partial_u\phi)^2 \\ \qquad\qquad + V\xi\,\partial_u\theta - V\sin\theta\,\partial_u\phi & \text{(8.5a)} \\ \alpha\Omega\,\sin\theta = 2\cos\theta\,\partial_u\theta\,\partial_u\phi + \sin\theta\,\partial_u^2\phi \\ \qquad\qquad + V\,\partial_u\theta + V\xi\sin\theta\,\partial_u\phi & \text{(8.5b)} \end{cases}$$

We have here introduced $\Omega = \Omega'/(1+\alpha^2)$. We note that, at the boundaries of the nanopillar ($u = 0,\,1$), Eq. (8.5b) gives:

$$\theta = \pi,\,0 \longrightarrow \partial_u\theta\left(\partial_u\phi \mp \frac{V}{2}\right) = 0.$$

$\partial_u\theta$ cannot be zero at the boundaries, at least for small currents, for which we expect the solution to be close to the zero current solution (8.3). We then conclude:

$$\partial_u\phi|_{u=0} = +\frac{V}{2}, \qquad \partial_u\phi|_{u=1} = -\frac{V}{2}.$$

This result suggests that $\partial_u\phi$ should be of the same order of V. This is an assumption we make, which enables us to proceed with important approximations. Indeed, for the material and the geometry we are dealing with, and a current density around $j \sim 10^{11}\,\mathrm{A/m^2}$, we have $V \sim 0.05$. Therefore the assumption $\partial_u\phi \sim V$ implies that the typical torsion of the domain wall is, in general, rather small $\Delta\phi \approx V \approx 3^\circ$. It implies also that the second and fourth terms on the right hand side of (8.5a) are of order $V^2 \approx 2.5\times10^{-3}$. On the other hand (8.3) suggests that $\partial_u\theta \sim -\pi$ and we expect $\partial_u^2\theta$ to be of the same order of magnitude, when the domain wall is compressed. We may then neglect terms of order V^2 and terms of order ξV, since typically $\xi \sim 10^{-2}$.

Then the system (8.5) reduces to:

$$\begin{cases} -\Omega\,\sin\theta = \partial_u^2\theta & (8.6a) \\ \alpha\Omega\,\sin\theta = 2\cos\theta\,\partial_u\theta\,\partial_u\phi + \sin\theta\,\partial_u^2\phi + V\,\partial_u\theta & (8.6b) \end{cases}$$

We immediately note that all the terms containing ξ have disappeared from the system: we are neglecting the non adiabatic effects of the spin transfer torque interaction.

Eq. (8.6a) is the pendulum equation. It could be used together with the boundary conditions (8.2) to obtain $\theta(u)$, once Ω is known. However determining Ω is not easy. We can find a constraint on Ω and θ from the second equation (8.6b), by multiplying both of its sides by $\sin\theta$,

$$\alpha\Omega\,\sin^2\theta = \partial_u[\sin^2\theta\,\partial_u\phi] - V\,\partial_u\cos\theta. \tag{8.7}$$

This equation can be integrated:

$$\int_0^1 \sin^2\theta\,\mathrm{d}u = -\frac{2V}{\alpha\Omega}. \tag{8.8}$$

$\theta(u)$ can now be found by searching for the solutions of the pendulum equation (8.6a) which also satisfy (8.2) and (8.8). Our main goal, however, is to find $\Omega(V)$, rather than finding $\theta(u)$ and $\phi(u)$. To do this, we multiply both sides of (8.6a) by $\partial_u\theta$:

$$\Omega\,\partial_u\cos\theta = \frac{1}{2}\partial_u\left(\partial_u\theta\right)^2,$$

which can be integrated, obtaining:

$$\Omega\,\cos\theta + I = \frac{1}{2}\left(\partial_u\theta\right)^2,$$

where I is a positive (take $\theta = \pi/2$) integration constant. This equation gives an expression for $\partial_u\theta$:

$$\partial_u\theta = -\sqrt{2(I + \Omega\,\cos\theta)}. \tag{8.9}$$

The sign in front of the square root was chosen in order to satisfy the boundary conditions (8.2). We can now change variable of integration in (8.8), obtaining:

$$\int_0^\pi \frac{\sin^2\theta\,\mathrm{d}\theta}{\sqrt{2(I + \Omega\,\cos\theta)}} = -\frac{2V}{\alpha\Omega}. \tag{8.10}$$

A second integral equation can be derived integrating the identity $\mathrm{d}\theta/\partial_u\theta = \mathrm{d}u$ and using the boundary conditions (8.2):

$$\int_0^\pi \frac{\mathrm{d}\theta}{\sqrt{2(I + \Omega\,\cos\theta)}} = 1. \tag{8.11}$$

I and Ω can then be found by solving the following system of equations:

$$\begin{cases} f_1\left(\frac{\Omega}{I}\right) = -\frac{2V}{\alpha\Omega}\sqrt{I} \\ f_2\left(\frac{\Omega}{I}\right) = \sqrt{I} \end{cases} \tag{8.12}$$

where the two functions f_1 and f_2 are defined in the following way:

$$f_1(x) = \int_0^{\pi} \frac{\sin^2\theta\,\mathrm{d}\theta}{\sqrt{2(1 + x\,\cos\theta)}},$$
$$f_2(x) = \int_0^{\pi} \frac{\mathrm{d}\theta}{\sqrt{2(1 + x\,\cos\theta)}},$$

and x has to be such that $|x| < 1$ in order for f_2 to exist. The system (8.12) is difficult to solve in general. Here we consider two limiting cases:

- $|\frac{\Omega}{I}| \gtrsim 0$. Since $f_1(0) = \frac{\pi}{2\sqrt{2}}$ and $f_2(0) = \frac{\pi}{\sqrt{2}}$, we get $I = \frac{\pi^2}{2}$ and $\Omega \approx -\frac{4V}{\alpha}$. The condition $|\frac{\Omega}{I}| \gtrsim 0$, becomes then $|\frac{V}{\alpha}| \ll \frac{\pi^2}{8}$;
- $|\frac{\Omega}{I}| \lesssim 1$. Since $f_1(1) = \frac{4}{3}$, $\Omega \approx -\frac{3}{2}\frac{V}{\alpha}\sqrt{I}$. Considering that $|I| \approx |\Omega|$, we finally get $\Omega \approx -\left(\frac{3}{2}\frac{V}{\alpha}\right)^2$. Moreover when $x \to 1$, $f_2(x) \to +\infty$. We then conclude that $|I| \approx |\Omega| \gg 1$ and hence $|\frac{V}{\alpha}| \gg 1$.

These results are summarised below:

$$\Omega = \begin{cases} -\frac{4V}{\alpha} & \text{for } \left|\frac{V}{\alpha}\right| \ll 1 \\ -\left(\frac{3}{2}\frac{V}{\alpha}\right)^2 & \text{for } \left|\frac{V}{\alpha}\right| \gg 1 \end{cases} \tag{8.13}$$

The frequency can be deduced easily from the formula $\nu_\mathrm{f} = \frac{\gamma' C}{2\pi\,L^2}\,|\Omega'| = \frac{\gamma C}{2\pi\,L^2}\,|\Omega|$:

$$\nu_\mathrm{f} = \begin{cases} \frac{2}{\pi}\frac{v}{\alpha L} & \text{for } \left|\frac{Lv}{\alpha\gamma C}\right| \ll 1 \\ \frac{1}{2\pi\,\gamma C}\left(\frac{3}{2}\frac{v}{\alpha}\right)^2 & \text{for } \left|\frac{Lv}{\alpha\gamma C}\right| \gg 1 \end{cases} \tag{8.14}$$

Let's now define j_0 such that $V/\alpha = j_\mathrm{P}/j_0$. Then the low current condition $|\frac{V}{\alpha}| \ll 1$ becomes $|j_\mathrm{P}| \ll j_0$ and similarly the high current condition becomes $|j_\mathrm{P}| \gg j_0$ and,

$$j_0 = \frac{2e\gamma}{\mu_0\mu_B}\,\frac{\alpha\,A}{L} \tag{8.15}$$

Which shows, in particular, that the critical current which distinguishes between the low current regime and the high current regime depends on the nanopillar length L.

We note that in the low current regime the frequency does not depend on the strength of the exchange interaction $C = 2A/\mu_0 M_\mathrm{sat}$. It depends on the length of the domain wall L and on the magnitude of the applied current v. On the other hand,

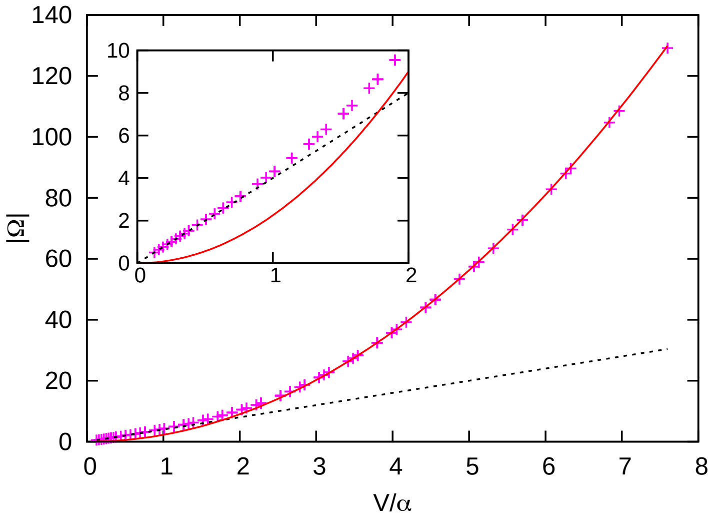

Figure 8.8: Comparison between the numerical values for $|\Omega(V)|$ obtained from the one dimensional micromagnetic simulations (crosses) and the low current (dotted line) and high current (solid line) analytical solutions.

in the high current regime, the frequency does not depend on L anymore. It depends however on the strength of the exchange coupling C and depends quadratically on v.

Fig. 8.8 shows the validation of the analytic expressions for $\Omega(V)$ against the results of the one dimensional micromagnetic simulations of Fig. 8.7. The graph contains all the data shown in Fig. 8.7 plotted in terms of the reduced quantities V and Ω. Consequently all the points obtained for different values of L and j_{P} lie in a single curve. The graph shows good agreement between theory and simulations, thus supporting the approximations which were made to get to the final formulas.

We make a final remark on the different dependence of the frequency on the applied current in the two regimes. There are two reasons why an increase of the current may lead to an increased asymptotic frequency. Firstly, the two terms through which the spin-transfer torque enters Eq. (3.12) share the prefactor $v \propto j$: double the current, double the spin-transfer torque terms and double the effect. The second way the current may increase the frequency is by reducing the domain wall width. A reduced domain wall width corresponds to an increased value of $\partial_x \vec{M}$, which appears in both the spin-transfer torque terms. In the linear regime, only the first effect occurs. Indeed, from (8.9) we see that $\partial_u \theta = -\sqrt{2I}\sqrt{1 + \frac{\Omega}{I}\cos\theta}$, where $\frac{\Omega}{I} \approx 0$ and $I = \frac{\pi^2}{2}$. We then get, $\partial_u \theta \approx -\pi$, which means that, in the low current regime, the domain wall shape does not change too much with respect to the zero current configuration (8.3). On the other hand, in the high current regime, $\frac{\Omega}{I} \approx -1$ and $\partial_u \theta = -\frac{3V}{\alpha} \sin \frac{\theta}{2}$. $\partial_u \theta$ depends on j, through V. This analysis suggests that the low/high current regimes correspond respectively to low/high domain wall deformation.

8.6 Discussion

We discussed the role of the nanopillar shape in Ch. 7: due to the cylindrical shape of the nanopillar, a rotation of the whole magnetisation around the nanopillar axis does not require to overcome any energy barriers. This feature is extremely important for the dynamic process we have studied here, because it allows the current to gradually transfer energy to the system and store it by compressing the domain wall. An important question to answer is then: how much does the shape of the nanopillar affect the dynamics of such systems? We have cross performed simulations for nanopillars with a square section and found very similar results: for a nanopillar with length $L = 40\,\mathrm{nm}$ and square section $20 \times 20\,\mathrm{nm}$ we chose $j = 10^{10}\,\mathrm{A/m^2}$ and found a frequency $\nu_\mathrm{f} \approx 0.61\,\mathrm{GHz}$, while for the corresponding cylindrical nanopillar $\nu_\mathrm{f} = 0.64\,\mathrm{GHz}$.

Equations (8.13) and (8.14) show that the rotation frequency can be expressed as a function of V/α and ultimately as a function of j_P/α. This means that for a value of α larger by a factor two, a current density larger by a factor two is required in order to obtain the same frequency. This consideration indicates that low damping constant is a desirable feature, when choosing a material for a concrete realisation of the system proposed in this chapter. We have chosen permalloy, because, besides being a particularly soft magnetic material, it has been intensively studied in spin transport experiments in recent years and values between 0.01 and 0.02 have been estimated[93, 94, 21] for its damping constant α. We point out that our choice, $\alpha = 0.02$, is conservative: the value $\alpha = 0.01$ would lead to considerably enhanced current effects and — in the quadratic regime — would lead to quadrupled frequency.

The electric currents required in spin transfer torque experimental studies are often high enough to produce considerable Joule heating and Oersted field. These effects should however be expected to become less and less important as the system is scaled down. Indeed, smaller systems are able to dissipate heat more efficiently than big systems, since reduced size corresponds to increased surface/volume ratio. Similarly, the Oersted field is reduced in smaller nanowires, being proportional to the total current flowing throughout the sample. On the other hand, the spin transfer torque does not depend on the system size, provided the current density remains constant. These considerations suggest that the nanopillar we presented in this chapter should be even less affected than the larger nanowires studied in other works[20, 18, 21], where Oersted field and Joule heating were found to be negligible or unable to limit the effects of spin transfer torque. Besides these empirical arguments, we can obtain an estimate of the Oersted field, using a simple model, where the nanowire is approximated with an infinitely long cylinder with radius R and is traversed by a uniform current density j. In this simple picture, the Oersted field circulates around the nanopillar axis and has maximum intensity $B_{\mathrm{max}} = \mu_0 R j/2$, which is reached on the surface of the nanopillar. Considering the extreme case $j_{\mathrm{P}} = 2\times 10^{11}\,\mathrm{A/m^2}$ and $P = 0.4$, we get $j = 5\times 10^{11}\,\mathrm{A/m^2}$ and $B_{\mathrm{max}} = 0.00314\,\mathrm{T}$. This field does not act against the rotation of the whole magnetisation around the nanopillar axis, since it is invariant for such transformations. Moreover its intensity is so small that we cannot really expect any relevant deformations of the artificial domain wall created by the pinning (the demagnetising field is two orders of magnitude bigger and still produces only moderate profile adjustments). We conclude that neglecting the Oersted field is an appropriate approximation.

8.7 Summary

We used micromagnetic simulations to study the spin transfer torque effects that occur in a nanopillar when the magnetisation is pinned at its ends. We showed that the dynamics of such a system is characterised by a stationary precession of the whole magnetisation of the system around its axis. We presented both three dimensional and one dimensional computations, and studied the asymptotical precession frequency ν_{f} as a function of the polarised current and of the nanopillar length. We derived an analytical model which provides further insight into the physics of the system and shows that there are two current regimes, where the system exhibits different dependencies on the applied current. We found good agreement between the results of the simulations and the theory.

Chapter 9

Summary and outlook

9.1 Summary

The research on magnetism is facing a new era, characterised by an unprecedented interest in the interplay between magnetism and other types of physics. Researchers in the field are facing new challenges when studying phenomena such as the effect of a spin polarised current or a light pulse on the magnetisation dynamics, and computer simulations can prove invaluable to help the understanding of experimental results or to assist in the research and optimisation of new devices. Numerical investigations of such effects require new powerful and flexible simulation tools, which can go beyond pure micromagnetics and can perform real multiphysics simulations.

For this thesis we devoted considerable effort in developing *Nmag*, a flexible finite element method micromagnetic simulation package which was used for our own computer simulations and has also been made available — as open source — to the magnetism community. We used *Nmag* to investigate the micromagnetic systems which are of interest to our group in Southampton, publishing our findings in specialised journals [54, 55, 56].

In particular, in Ch. 6 we developed a new model for studying $DyFe_2$-YFe_2 multilayered exchange spring systems, which uses two distinct fields to represent the magnetisation of iron and dysprosium. This is certainly an improvement over previous computational approaches [95], where the magnetisation in the $DyFe_2$ layers is modeled by a single vector field, assuming rigid antiparallelism between the moments of the two species. The two fields model was used to investigate a trilayer $DyFe_2$-YFe_2-$DyFe_2$ exchange spring system, showing that the average magnetisation moves in spiral trajectories near equilibrium. We found that, for such a precessional motion, the damping parameter and frequency both reach their minimum values when the applied field gets close to the bending field, while the amplitude of the spiralling orbits reaches its maximum value. Such an observation motivated further investigations on the effects of an electric current travelling in the out of plane direction in the very same trilayer system. If on the one hand, we found that the magnetisation is particularly reactive to external stimuli near the bending field, on the other, the spin transfer torque effects are rather weak in such a situation, because the magnetisation is almost uniform. We linearised the Landau-Lifshitz-Gilbert equation and derived analytical models for the system which we studied numerically. This theoretical work was used to validate and improve our understanding of the numerical results. We derived a new expression for the bending field which takes into account the penetration of the exchange spring inside the hard layers and gives estimates which agree nicely with the numerical values.

In Ch. 7 we showed that, despite the results obtained in the previous chapter, relevant spin transfer torque effects may be observed in a trilayer exchange spring system, when the geometry and the materials are chosen appropriately. We studied again a trilayer exchange spring system, but with two differences with respect to the system investigated in Ch. 6. The geometry is the first difference: we studied a cylindrical nanopillar, rather than a thin film. The second difference lies in the configuration of the magnetisation. We assumed the two hard layers to be magnetised in opposite directions, forcing the magnetisation to rotate by 180 degrees inside the soft layer, thus developing what we called "artificial" domain wall. We studied how an electric current (with density around $j = 10^{11}\,\mathrm{A/m^2}$), flowing along the axis of the cylindrical nanopillar, interacts with the magnetisation and found interesting results: the domain wall compresses along the direction of the electron flow reaching a stationary equilibrium where the magnetic moments rotate coherently with constant frequency around the nanopillar axis.

In Ch. 8 we performed computer simulations in order to assess how the asymptotic precession frequency depends on the the current density and on the nanopillar length. We studied a system similar to the one presented in the previous chapter, with one difference: the cylindrical nanopillar was made of just one single material and the action of the hard layers was reproduced by assuming infinite pinning on the magnetisation at the two opposite faces of the cylinder. Using infinite pinning (which corresponds to keeping the magnetisation constant), we reproduced qualitatively all the results obtained for the trilayer nanopillar, thus clarifying that the role of the hard layers is just to pin the magnetisation along opposite directions at the soft-hard interfaces. We also presented a one dimensional analytical model, much simpler than the numerical model, but still able to capture the essence of the physics of the system and able to reproduce most of its features. The analytical model shows that the precession of the magnetisation is an effect of the compression. It gives a mathematical formula that, together with the numerical results, helps to understand how the parameters for geometry and materials balance to determine the asymptotical frequency of the magnetisation precession.

9.2 Conclusion and outlook

In conclusion, we developed *Nmag*, a software package which we used to produce all the numerical results presented in our thesis. We used *Nmag* to carry out multiphysics simulations. In Ch. 6 we performed simulation of $DyFe_2$-YFe_2 exchange spring system, where the micromagnetic model was extended to allow a two-field representation of the magnetisation in the hard layers. In Ch. 7 and 8 we extended the micromagnetic model with the spin transfer torque effects to study a novel and interesting effect. While current driven domain wall motion in nanowires has been widely reported and studied in recent publications, the compression and rotation of a domain wall constrained in a cylindrical nanopillar is indeed — to our best knowledge — a new effect, which was presented and understood for the first time in this thesis and the derived publications. We hope to be able to see soon these effects in experimental samples.

There are some open problems which may be the natural continuation of the work presented in this thesis. We list them below:

- carry out further studies on the system presented in Ch. 7 and 8 and understand if the same mechanism could be exploited to obtain a bistable system which can be switched from one status to the other by the application of an electric current. One possible idea to achieve this is shown in Fig. 9.1.

- work on other multiphysics extensions to *Nmag*. It would be useful — in particular — to include Joule heat generation and diffusion, since one of the main concerns when studying current-driven magnetisation dynamics is the magnitude of the current density and the heating which may be connected to it. Another useful multiphysics extension would be the calculation of the Oersted field, relevant — in particular — when assessing the importance of spin transfer torque effects.

- in Ch. 6 we found that a continuous current has weak effects on the dynamics

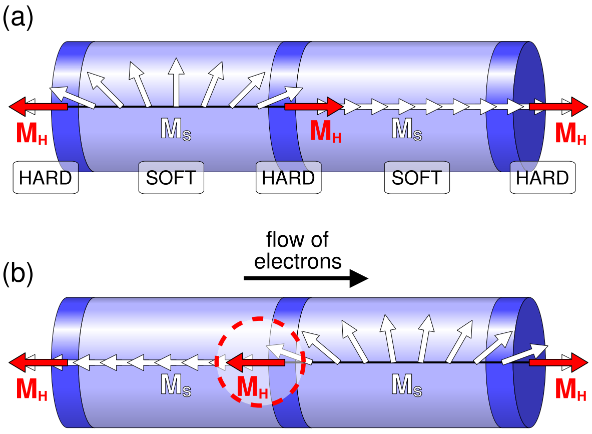

Figure 9.1: Sketch of a hard/soft/hard/soft/hard exchange spring system. This picture shows how the mechanism which was used in Ch. 7 and 8 to generate microwaves may be used in order to switch a hard magnetic layer. The electric current pushes the domain wall from the soft layer on the left (a) into the soft layer on the right (b), thus switching the central hard layer.

of the considered trilayer exchange spring system. The magnetisation dynamics may be different for a pulsed current. We may get a noticeable amplification of the effects near the resonance frequency, with a mechanism analogous to the one described in Fig. 1 of Ref. [85]. Further studies may then be carried out in order to assess the importance of such an effect.

Appendix A

The choice of units for the LLG equation

In this appendix we show how to choose units in such a way that all the parameters which describe a typical micromagnetic physical system have numerical values around one. This approach is useful during debugging, since it makes it simple to read and understand the numerical values involved in the simulation. Most importantly, this is the choice of units which has been made for *Nmag*, the software package which has been used to produce the results in this thesis.

In the following table we present some typical numerical values[1] used in the LL equation.[2]

free space permeability	μ_0	$=$	$(4\pi/10)\cdot 10^{-6}$	$\mathrm{N/A^2}$
saturation magnetisation	M_{sat}	$\approx$	$0.8\cdot 10^{6}$	A/m
damping factor	α	$\approx$	0.5 or[3] 0.02	
gyromagn. ratio	γ'	$\approx$	$0.2\cdot 10^{6}$	m/As
exchange stiffness constant	A	$\approx$	$13\cdot 10^{-12}$	J/m

Provided that we express times in picoseconds (1 ps $= 10^{-12}$ s) and lengths in nanometers (1 nm $= 10^{-9}$ m), we can omit the factors $10^{\cdots}$ and use $\mu_0 = 4\pi/10$, $M = 0.8$, etc inside the LL equation. We can verify it in the following way: let us use typewriter font to denote the values used inside the program. For example: $H = \mathtt{H}\cdot 10^6\mathrm{A/m}$, where $\mathtt{H}$

---

[1] The values of M_{sat} and A are relative to permalloy.

[2] The exchange length l_{ex} is calculated as $l_{\text{ex}} = \sqrt{\frac{2A}{\mu_0 M^2}}$, for permalloy $l_{\text{ex}} = 5.686\,\text{nm}$.

[3] The more realistic value is 0.02, but the value 0.5 is often used to speed up the convergence of the simulations where the dynamics of the system is not being investigated.

could be imagined as the variable used to store the effective magnetic field. If inside the program we write `H` $= 0.5$, we mean that the actual field will be $H = 0.5 \cdot 10^6 \mathrm{A/m} = 500000\,\mathrm{A/m}$. This means that inside the program we should multiply by the factor 10^6 before using the value stored inside `H`. However our choice is such that these factors cancel out and therefore such a multiplication is not needed. We use:

$$\begin{array}{rcll} \text{time} & t & = & \mathtt{t} \cdot 10^{-12}\,\mathrm{s} \\ \text{space} & r & = & \mathtt{r} \cdot 10^{-9}\,\mathrm{m} \\ \text{magnetic fields} & H & = & \mathtt{H} \cdot 10^{6}\,\mathrm{A/m} \\ \text{gyromagn. ratio} & \gamma' & = & \mathtt{gamma} \cdot 10^{6}\,\mathrm{m/As} \\ \text{exchange stiffness constant} & A & = & \mathtt{A} \cdot 10^{-12}\,\mathrm{J/m} \end{array}$$

We consider the LL equation for the normalised vector $\vec{m}$ (which is consequently non-dimensional).

$$\partial_t \vec{m} = -\gamma' \left[\vec{m} \times \vec{H} + \alpha\, \vec{m} \times \left(\vec{m} \times \vec{H} \right) \right]$$

After the substitutions:

$$\begin{array}{rcl} \partial_{(\mathtt{t} \cdot 10^{-12}\,\mathrm{s})} \vec{m} & = & -(\mathtt{gamma} \cdot 10^{6}\,\mathrm{m/As})[\vec{m} \times (\mathtt{H} \cdot 10^{6} \mathrm{A/m}) + \ldots \\ & & \ldots + \alpha\, \vec{m} \times \left(\vec{m} \times (\mathtt{H} \cdot 10^{6}\,\mathrm{A/m}) \right)] \end{array}$$

We see easily that the factors cancel out. This means that we do not need to change our program and adapt it to the new units. We simply should give numbers as shown inside the above tables. A similar check can easily be done for the expression of the effective field:

$$\vec{H} = \frac{2A}{\mu_0 M} \nabla^2 \vec{m}(\vec{r}) + \vec{H}_{\mathrm{a}} + \vec{H}_{\mathrm{d}},$$

where $\vec{H}_{\mathrm{a}}$ is the applied field and $\vec{H}_{\mathrm{d}}$ is the demagnetising field, which is obtained solving the Poisson equation:

$$\nabla^2 \phi = \nabla \cdot \vec{M},$$

where $\vec{H}_{\mathrm{d}} = -\nabla \phi$.

Appendix B

Solution of the LLG equation for constant applied field

The LL equation can be solved analytically when the effective field is constant in time. In this appendix we derive such an analytical solution following the paper published by Jiang *et al.* [96, 43]. Assuming constant applied field is evidently a restrictive hypothesis in micromagnetics, but nevertheless it is worth to consider it: firstly because analytical solutions are always useful for testing purposes or for getting a better understanding of the underlying physics and secondly because this particular analytical solution has been used several times in semi-analytical models, as discussed in Ch. 4.

Derivation

The idea underlying the method is to decompose the LL equation into two components: the one parallel to the applied field, $\vec{H}$, and the one orthogonal to it. We will see that if $\vec{H}$ is constant in time, this separation leads to an exact analytical solution. Consider the well known identity for triple vector products:

$$\vec{A} \times (\vec{B} \times \vec{C}) = (\vec{A} \cdot \vec{C})\vec{B} - (\vec{A} \cdot \vec{B})\vec{C}, \tag{B.1}$$

which holds for any triple of vectors $\vec{A}$, $\vec{B}$ and $\vec{C}$. Let us choose $\vec{A} = \vec{h}$, $\vec{B} = \vec{v}$ and $\vec{C} = \vec{h}$ for a given vector $\vec{v}$. We obtain:

$$\vec{v} = (\vec{v} \cdot \vec{h})\,\vec{h} + \vec{h} \times (\vec{v} \times \vec{h}).$$

Defining:

$$\begin{aligned} \mathbf{P}\vec{v} &= (\vec{v} \cdot \vec{h})\,\vec{h}, && \text{(B.2)} \\ \mathbf{Q}\vec{v} &= \vec{v} - \mathbf{P}\vec{v} = \vec{h} \times (\vec{v} \times \vec{h}), && \text{(B.3)} \end{aligned}$$

we can write:

$$\vec{v} = \mathbf{P}\vec{v} + \mathbf{Q}\vec{v}.$$

P and **Q** are two projectors: **P** projects onto the space of vectors parallel to $\vec{h}$, while **Q** projects onto the space of vectors orthogonal to $\vec{h}$. We apply the projectors **P** and **Q** to both the sides of Eq. (4.1):

$$\begin{aligned} \mathbf{P}\vec{m}' &= -\gamma' H \left[\mathbf{P}(\vec{m}\times\vec{h}) + \alpha\mathbf{P}(\vec{m}\times(\vec{m}\times\vec{h}))\right], && \text{(B.4)} \\ \mathbf{Q}\vec{m}' &= -\gamma' H \left[\mathbf{Q}(\vec{m}\times\vec{h}) + \alpha\mathbf{Q}(\vec{m}\times(\vec{m}\times\vec{h}))\right]. && \text{(B.5)} \end{aligned}$$

From Eq. (B.2) we see that $\mathbf{P}(\vec{m}\times\vec{h}) = 0$. Applying the identity (B.1) for the cross product we obtain: $\vec{m}\times(\vec{m}\times\vec{h}) = \vec{m}(\vec{m}\cdot\vec{h}) - \vec{h}$, which allows us to write:

$$\mathbf{P}(\vec{m}\times(\vec{m}\times\vec{h})) = (\vec{m}\cdot\vec{h})\,\mathbf{P}\vec{m} - \vec{h} = (\vec{m}\cdot\vec{h})^2\,\vec{h} - \vec{h}.$$

Since $(\vec{m}\cdot\vec{h})^2 = \|\mathbf{P}\vec{m}\|^2$, Eq. (B.4) becomes:

$$\mathbf{P}\vec{m}' = \gamma' H\alpha\,(1 - \mathbf{P}\vec{m}\,\cdot\mathbf{P}\vec{m})\,\vec{h}. \tag{B.6}$$

This is the LL equation projected along the direction of $\vec{h}$. Now let's consider the **Q**-projection of the LL equation. As before the cross product is expressed as $\vec{m}\times(\vec{m}\times\vec{h}) = \vec{m}(\vec{m}\cdot\vec{h}) - \vec{h}$. Obviously $\mathbf{Q}\vec{h}$ gives 0, hence:

$$\mathbf{Q}(\vec{m}\times(\vec{m}\times\vec{h})) = (\vec{m}\cdot\vec{h})\,\mathbf{Q}\vec{m}.$$

Finally we consider $\vec{m}\times\vec{h}$. This vector belongs to the plane orthogonal to $\vec{h}$, where **Q** behaves like the identity operator:

$$\mathbf{Q}(\vec{m}\times\vec{h}) = \vec{m}\times\vec{h}. \tag{B.7}$$

However, as we will see later, we need to express this value as a function of $\mathbf{Q}\vec{m}$ in order to handle the projected equation. For this reason we define the following linear operator:

$$\mathbf{J}\vec{v} = (\vec{h}\cdot\vec{v})\,\vec{h} - \vec{v}\times\vec{h}. \tag{B.8}$$

If we now apply **J** to the vector $\mathbf{Q}\vec{m}$[1]:

$$\mathbf{J}(\mathbf{Q}\vec{m}) = \mathbf{J}(\vec{m} - (\vec{h}\cdot\vec{m})\,\vec{h}) = -\vec{m}\times\vec{h}.$$

---

[1] **J** represents a rotation of 90 degrees around the axis parallel to $\vec{h}$. This can be used to derive the same result in a more intuitive fashion.

Using this result into Eq. (B.7), we find:

$$\mathbf{Q}(\vec{m} \times \vec{h}) = -\mathbf{J}(\mathbf{Q}\vec{m}). \tag{B.9}$$

We can finally write the LL equation projected along the plane orthogonal to $\vec{h}$:

$$\mathbf{Q}\vec{m}' = \gamma' H \left(\mathbf{J} - \alpha\,(\vec{m} \cdot \vec{h})\,\mathbf{I}\right) \mathbf{Q}\vec{m}, \tag{B.10}$$

$\mathbf{I}$ is the identity operator.

Suppose now that $\vec{H}$ does not change in time. In this case $\mathbf{P}\vec{m}' = \left(\partial_t \vec{m} \cdot \vec{h}\right) \vec{h} = \partial_t(\vec{m}\cdot\vec{h})\,\vec{h} = (\mathbf{P}\vec{m})'$. In a similar way $\mathbf{Q}\vec{m}' = (\mathbf{Q}\vec{m})'$. If we define the scalar $u = (\mathbf{P}\vec{m})\cdot\vec{h}$ and the vector $\vec{v} = \mathbf{Q}\vec{m}$, the projected Eqs. (B.6) and (B.10) can be rewritten in the following way:

$$\begin{aligned} u' &= \gamma' H \alpha (1 - u^2), \\ \vec{v}' &= \gamma' H \left(\mathbf{J} - \alpha\,(\vec{m} \cdot \vec{h})\,\mathbf{I}\right) \vec{v}. \end{aligned}$$

The first of these two equations is independent of $\vec{v}$ and can be therefore integrated immediately:

$$u(t) = \frac{u_0 \cosh(\alpha\gamma' H\,t) + \sinh(\alpha\gamma' H\,t)}{\cosh(\alpha\gamma' H\,t) + u_0 \sinh(\alpha\gamma' H\,t)},$$

u_0 is the initial value for u: $u(t = 0) = u_0$. This result can be used to integrate the second equation [96, 43]:

$$\vec{v}(t) = \frac{\cos(\gamma' H\,t)\,\mathbf{I} + \sin(\gamma' H\,t)\,\mathbf{J}}{\cosh(\alpha\gamma' H\,t) + u_0 \sinh(\alpha\gamma' H\,t)} \vec{v}_0.$$

$\vec{v}_0$ is the initial value for $\vec{v}$ and defines the initial condition, together with u_0. Remembering how u and $\vec{v}$ were defined, we obtain $\vec{m}(t) = u(t)\,\vec{h} + \vec{v}(t)$. We can express the initial condition using $\vec{m}_0 = m(t = 0)$. This is easily done using Eqs. (B.2) and (B.3). We see that: $u_0 = \vec{m}_0 \cdot \vec{h}$ and $\vec{v}_0 = \vec{h} \times (\vec{m}_0 \times \vec{h})$.

Summary

Since we consider these solutions quite interesting we write them in a different and slightly clearer formulation. First we express the equations as they appear in the original papers [96, 43]. If $\vec{H} = H\,\vec{h}$ is constant in time, then (we omit the space dependence):

$$\vec{m}(t) = a(t)\,\vec{h} + \mathbf{B}(t)\,\left[\vec{h} \times (\vec{m}_0 \times \vec{h})\right],$$

where $\vec{m}_0 = \vec{m}(t=0)$,

$$\begin{aligned}
a(t) &= \frac{(\vec{m}_0 \cdot \vec{h}) \cosh(\gamma' \alpha H\, t) + \sinh(\gamma' \alpha H\, t)}{\cosh(\gamma' \alpha H\, t) + (\vec{m}_0 \cdot \vec{h}) \sinh(\gamma' \alpha H\, t)}, \\
\mathbf{B}(t) &= \frac{\cos(\gamma' H\, t)\, \mathbf{I} + \sin(\gamma' H\, t)\, \mathbf{J}}{\cosh(\gamma' \alpha H\, t) + (\vec{m}_0 \cdot \vec{h}) \sinh(\gamma' \alpha H\, t)}, \\
\gamma' &= \frac{\gamma}{1+\alpha^2},
\end{aligned}$$

and, given any vector $\vec{v}$:

$$\begin{aligned}
\mathbf{I}\vec{v} &= \vec{v}, \\
\mathbf{J}\vec{v} &= (\vec{h} \cdot \vec{v})\, \vec{h} - \vec{v} \times \vec{h}.
\end{aligned}$$

In our particular case:

$$\mathbf{J}\left[\vec{h} \times (\vec{m}_0 \times \vec{h})\right] = \vec{h} \times \vec{m}_0.$$

So we can rewrite the equations in a more convenient form (for computation):

$$\begin{aligned}
\vec{m}(t) &= a(t)\, \vec{h} \\
&+ b(t)\, \vec{h} \times \vec{m}_0 \\
&+ c(t) \left[(\vec{h} \times \vec{m}_0) \times \vec{h}\right], \qquad \text{(B.11)}
\end{aligned}$$

where $\vec{m}_0 = \vec{m}(t=0)$, $\gamma' = \gamma/(1+\alpha^2)$ as before, and:

$$\begin{aligned}
a(t) &= \left[(\vec{m}_0 \cdot \vec{h}) \cosh(\gamma' \alpha\, t) + \sinh(\gamma' \alpha H\, t)\right] / D(t), && \text{(B.12)} \\
b(t) &= \sin(\gamma' H\, t)/D(t), && \text{(B.13)} \\
c(t) &= \cos(\gamma' H\, t)/D(t), && \text{(B.14)} \\
D(t) &= \cosh(\gamma' \alpha H\, t) + (\vec{m}_0 \cdot \vec{h}) \sinh(\gamma' \alpha H\, t). && \text{(B.15)}
\end{aligned}$$

To understand the dynamics better we express this result in spherical coordinates: we take a reference frame with z axis along $\vec{h}$ and y axis along $\vec{m}_0 \times \vec{h}$ (as a consequence the x axis lies along the vector $(\vec{h} \times \vec{m}_0) \times \vec{h}$). In this reference frame the solution can be expressed easily as: $\vec{m}(t) = (c(t) \sin\theta_0,\, b(t) \sin\theta_0,\, a(t))$, where $\sin\theta_0 = \|\vec{h} \times \vec{m}_0\| = \|(\vec{h} \times \vec{m}_0) \times \vec{h}\|$. Note that this vector has unit norm. We can write it using the spherical coordinates $\theta(t)$ and $\phi(t)$ with polar axis along z:

$$\vec{m}(t) = (\sin\theta(t) \cos\phi(t),\, \sin\theta(t) \sin\phi(t),\, \cos\theta(t))$$

Equating these two expressions of $\vec{m}$, we obtain:

$$\begin{aligned}
\phi(t) &= \gamma' H\, t, && \text{(B.16)} \\
\cos\theta(t) &= a(t) = \tanh\left(\gamma' \alpha H\, (t - t_0)\right), && \text{(B.17)} \\
\sin\theta(t) &= \tfrac{\sin\theta_0}{D(t)} = \frac{1}{\cosh\left(\gamma' \alpha H\, (t - t_0)\right)}, && \text{(B.18)}
\end{aligned}$$

$t_0 = \frac{1}{\gamma' \alpha H} \log \frac{\sin\theta_0}{1+\cos\theta_0}$ is the time at which $\vec{m}$ passes through the plane xy.

Discussion

These solutions give interesting hints to understand the dynamics generated by the LL equation. From Eq. (B.16) we see immediately that the vector $\vec{m}$ precesses around the effective field $\vec{h}$ with constant angular velocity. The frequency of this rotation is $\nu = \frac{\gamma' H}{2\pi}$. This means that — as expected — the dynamics is faster for higher effective field.[2]

When there is no damping ($\alpha = 0$) $D(t) = 1$ and from Eq. (B.18), $\sin\theta(t) = \sin\theta_0$: the angle $\theta(t)$ between the vectors $\vec{m}(t)$ and $\vec{h}$ is constant in time. This means that the dynamics is simply a rotation with constant angular velocity around the effective field.

When the damping is nonzero, the vector $\vec{m}(t)$ still precesses around $\vec{h}$ as before, but now it also moves towards $\vec{h}$. This effect is shown clearly by Eq. (B.17). We can also make an estimate of how fast this movement is by finding the time at which the angle between $\vec{m}(t)$ and $\vec{h}$ is equal to a very small angle $\Delta\theta$. From Eq. (B.18) we know that this happens when $\gamma' \alpha H\,(t - t_0) \gg 1$. In this case we can use the approximations $\cosh(\gamma' \alpha H\,(t - t_0)) \approx e^{\gamma' \alpha H\,(t-t_0)}/2$ and $\sin\Delta\theta \approx \Delta\theta$ to rewrite Eq. (B.18) as $\Delta\theta \approx 2\exp(-\gamma' \alpha H\,(t - t_0))$. Solving for t we obtain:

$$t_{\text{switch}} \approx \frac{1}{\gamma' \alpha H} \log\left(\frac{2\sin\theta_0}{\Delta\theta\,(1+\cos\theta_0)}\right).$$

t_{switch} is the time needed for the magnetisation, $\vec{m}$, to get from $\theta = \theta_0$ to $\theta = \Delta\theta$, where θ is the angle between $\vec{m}$ and the constant applied field of magnitude H. Such a switching time is inversely proportional to H and α. The same formula can be inverted to obtain $\Delta\theta \propto e^{-\gamma' \alpha H t}$, which shows that the angle between the magnetisation and the applied field decays exponentially for $t \to +\infty$.

Jiang *et al.* propose to use the analytical formulas for the magnetisation evolution in order to integrate the LL equation. The procedure they suggest is the following: to go from time t_0 to time $t_0 + \Delta t$ they assume that the change of $\vec{H}(t)$ in this time interval is negligible and use Eqs. (B.11–B.15) with $\vec{H}$ replaced by $\vec{H}(t_0)$. For this procedure to work, one must obviously choose Δt in a proper way: Jiang *et al.* suggested to use Δt such that the fastest precessional motion, among all the sites of the mesh, is resolved in a given number N of steps per period [43]. This could be done in this way: let's use the index i to label the physical entities defined at the site i of the mesh. From Eq.

---

[2] This could be argued from the beginning: the substitution $T = \gamma' H\,t$ in Eq. (4.1), shows that the solution of the LL equation must be a function of $\gamma' H\,t$

(B.16) one calculates the time Δt_i required to span an angle $2\pi/N$: $\Delta t_i = 2\pi/\gamma' N H_i$. $\Delta t = \min\{\Delta t_i\}_i$ is then chosen.

Appendix C

Anisotropy near the easy axis

In this appendix we express uniaxial and cubic anisotropy in spherical coordinates, choosing the polar axis aligned along one easy/hard direction. We then expand the anisotropies for small values of θ, the angle between the magnetisation and the easy/hard axis. We start from Eq. (2.9) and (2.10), the expressions of the uniaxial and cubic anisotropy introduced in Ch. 2:

$$\begin{aligned} \varepsilon_{\mathrm{ua}}(m_1) &= -K_1 m_1^2 - K_2 m_1^4, && \text{(C.1)} \\ \varepsilon_{\mathrm{ca}}(m_1,\, m_2,\, m_3) &= K_1(m_1^2 m_2^2 + m_2^2 m_3^2 + m_3^2 m_1^2) + K_2(m_1^2 m_2^2 m_3^2) \\ &\quad + K_3(m_1^4 m_2^4 + m_2^4 m_3^4 + m_3^4 m_1^4). && \text{(C.2)} \end{aligned}$$

m_1, m_2 and m_3 are defined as $m_i = \vec{m} \cdot \hat{x}_i$, where $\hat{x}_i$ are the unit vectors lying along the three orthogonal axes shown in Fig. C.1 and $\hat{x}_1$ is chosen to be one of the easy/hard directions. In terms of θ and ϕ, we can rewrite m_i as:

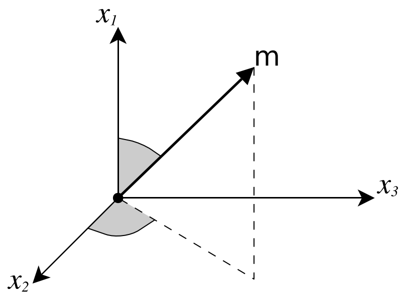

Figure C.1: We express both uniaxial and cubic anisotropy in spherical coordinates, choosing an easy axis as the polar axis, which is here denoted by x_1.

$$\begin{aligned} m_1 &= \cos\theta, \\ m_2 &= \sin\theta\cos\phi, \\ m_3 &= \sin\theta\sin\phi, \end{aligned}$$

which can then be substituted inside (C.1) and (C.2), obtaining:

$$\begin{aligned} \varepsilon_{\text{ua}}(\theta) &= -K_1\cos^2\theta - K_2\cos^4\theta, \\ \varepsilon_{\text{ca}}(\theta,\,\phi) &= K_1(\sin^2\theta\,\cos^2\theta + \sin^4\theta\,\sin^2\phi\,\cos^2\phi) \\ &\quad +K_2\sin^4\theta\,\cos^2\theta\,\cos^2\phi\,\sin^2\phi \\ &\quad +K_3(\sin^8\theta\,\cos^4\phi\,\sin^4\phi + \sin^4\theta\,\cos^4\theta\,(1-2\cos^2\phi\,\sin^2\phi)). \end{aligned}$$

When $\theta \ll 1$, we can approximate these expressions with:

$$\begin{aligned} \varepsilon_{\text{ua}}(\theta) &= \text{const.} + (K_1 + 2K_2)\theta^2 + \mathcal{O}(\theta^4), \\ \varepsilon_{\text{ca}}(\theta,\,\phi) &= K_1\theta^2 + \mathcal{O}(\theta^4). \end{aligned}$$

We conclude that both uniaxial and cubic anisotropy can be approximated by $A\theta^2$, when the magnetisation deviates by a small angle θ from an easy axis direction.

Bibliography

[1] B. Azzerboni, G. Asti, L. Pareti, and M. Ghidini, *Magnetic nanostructures in modern technology.* Springer, 2008.

[2] Seagate, "Seagate ships desktop hard drive with world's highest areal density – 500 GB per disk." `http://www.seagate.com/www/en-us/about/news_room/press_releases/product_press_releases/`, January 5, 2009.

[3] J. C. Slonczewski, "Current–driven excitation of magnetic multilayers," *J. Magn. Magn. Mater.*, vol. 159, pp. L1–L7, 1996.

[4] S. Kaka, M. R. Pufall, W. H. Rippard, T. J. Silva, S. E. Russek, and J. A. Katine, "Mutual phase-locking of microwave spin torque nano-oscillators," *Nature*, vol. 437, pp. 389–392, 2005.

[5] S. Blundell, *Magnetism in Condensed Matter.* Oxford University Press, 1st ed., 2001.

[6] A. Aharoni, *Introduction to the theory of Ferromagnetism.* Oxford Science Publications, 2nd ed., 2000.

[7] M. N. Baibich, J. M. Broto, A. Fert, F. N. van Dau, F. Petroff, P. Etienne, G. Creuzet, A. Friederich, and J. Chazelas, "Giant magnetoresistance of (001)Fe/(001)Cr magnetic superlattices," *Phys. Rev. Lett.*, vol. 61, pp. 2472–2475, 1988.

[8] G. Binash, P. Grünberg, F. Saurenbach, and W. Zinn, "Enhanced magnetoresistance in layered magnetic structures with antiferromagnetic interlayer exchange," *Phys. Rev. B*, vol. 39, p. 4828, 1989.

[9] L. Berger, "Emission of spin waves by a magnetic multilayer transversed by a current," *Phys. Rev. B*, vol. 54, no. 13, pp. 9353–9358, 1996.

[10] M. Tsoi, A. G. M. Jansen, J. Bass, W.-C. Chiang, M. Seck, V. Tsoi, and P. Wyder, "Excitation of a Magnetic Multilayer by an Electric Current," *Phys. Rev. Lett.*, vol. 80, no. 19, pp. 4281–4284, 1998.

[11] The Royal Swedish Academy of Sciences, "The discovery of giant magnetoresistance," October 2007. `http://nobelprize.org/nobel_prizes/physics/-laureates/2007/phyadv07.pdf`.

[12] G. Prinz, "Magnetoelectronics," *Science*, vol. 282, no. 8, pp. 1660–1663, 1998.

[13] R. C. O'Handley, *Modern Magnetic Materials: Principles and Applications.* John Wiley and Sons, Inc., 1999.

[14] L. Berger, "Low-field magnetoresistance and domain drag in ferromagnets," *J. Appl. Phys.*, vol. 49, pp. 2156–2161, 1978.

[15] E. B. Myers, D. C. Ralph, J. A. Katine, R. N. Louie, and R. A. Buhrman, "Current-induced switching of domains in magnetic multilayer devices," *Science*, vol. 285, p. 867, 1999.

[16] J. A. Katine, F. J. Albert, R. A. Buhrman, E. B. Myers, and D. C. Ralph, "Current-driven magnetization reversal and spin-wave excitations in Co/Cu/Co pillars," *Phys. Rev. Lett.*, vol. 84, pp. 3149–3152, 2000.

[17] W. Weber, S. Riesen, and H. C. Siegmann, "Magnetization precession by hot spin injection," *Science*, vol. 291, p. 1015, 2001.

[18] M. Kläui, P.-O. Jubert, R. Allenspach, A. Bischof, J. A. C. Bland, G. Faini, U. Rüdiger, C. A. F. Vaz, L. Vila, and C. Vouille, "Direct observation of domain-wall configurations transformed by spin currents," *Phys. Rev. Lett.*, vol. 95, p. 026601, 2005.

[19] M. Kläui, M. Laufenberg, L. Heyne, U. Rüdiger, C. A. F. Vaz, J. A. C. Bland, L. J. Heyderman, S. Cherifi, A. Locatelli, T. O. Mentes, and L. Aballe, "Current-induced vortex nucleation and annihilation in vortex domain walls," *App. Phys. Lett.*, vol. 88, p. 232507, 2006.

[20] G. Meier, M. Bolte, R. Eiselt, B. Krüger, D.-H. Kim, and P. Fischer, "Direct imaging of stochastic domain-wall motion driven by nano-second current pulses," *Phys. Rev. Lett.*, vol. 98, p. 187202, 2007.

[21] B. Krüger, D. Pfannkuche, M. Bolte, G. Meier, and U. Merkt, "Current-driven domain-wall dynamics in curved ferromagnetic nanowires," *Phys. Rev. B*, vol. 75, p. 054421, 2007.

[22] Z. Li and S. Zhang, "Domain-wall dynamics and spin-wave excitations with spin-transfer torques," *Phys. Rev. Lett.*, vol. 92, no. 20, p. 207203, 2004.

[23] S. Zhang and Z. Li, "Roles of nonequilibrium conduction electrons on the magnetization dynamics of ferromagnets," *Phys. Rev. Lett.*, vol. 93, no. 12, p. 127204, 2004.

[24] A. Thiaville, Y. Nakatani, J. Miltat, and Y. Suzuki, "Micromagnetic understanding of current-driven domain wall motion in patterned nanowires," *Europhys. Lett.*, vol. 69, no. 6, pp. 990–996, 2005.

[25] S. N. Gordeev, J.-M. L. Beaujour, G. J. Bowden, P. A. J. de Groot, B. D. Rainford, R. C. C. Ward, M. R. Wells, and A. G. M. Jansen, "Giant magnetoresistance by exchange springs in $DyFe_2/YFe_2$ superlattices," *Phys. Rev. Lett.*, vol. 87, no. 18, pp. 186808.1–186808.4, 2001.

[26] C. J. García and X. P. Wang, "Spin-polarized currents in ferromagnetic multilayers," *J. Comp. Phys.*, vol. 224, p. 699, 2007.

[27] M. Donahue and D. Porter, "OOMMF user guide for release 1.2a3." `http://math.nist.gov/oommf/doc/userguide12a3/userguide/`.

[28] J. Shewchuk, "What is a good linear finite element? interpolation, conditioning, anisotropy, and quality measures." `http//www.cs.cmu.edu/~jrs/jrspapers.html`.

[29] D. A. Lindholm, "Three-dimensional magnetostatic fields from point-matched integral equations with linearly varying scalar sources," *IEEE Trans. Magn.*, vol. 20, pp. 2025–2032, 1984.

[30] D. R. Fredkin and T. R. Koehler, "Hybrid method for computing demagnetizing fields," *IEEE Trans. Magn.*, vol. 26, pp. 415–417, 1990.

[31] P. H. W. Ridley, *Finite element simulation of the micromagnetic behaviour of nanoelements.* PhD thesis, School of Informatics, University of Wales, Bangor, 2000.

[32] W. Scholz, *Scalable parallel micromagnetic solvers for magnetic nanostructures.* PhD thesis, Fakultät für Naturwissenschaften und Informatik, Technische Universität Wien, 2003.

[33] T. Schrefl, G. Hrkac, S. Bance, D. Suess, O. Ertl, and J. Fidler, "Numerical methods in micromagnetics (Finite Element Method)," *Handbook of magnetism and advanced magnetic materials*, 2007.

[34] J. Schöberl, "Netgen website." `http://www.hpfem.jku.at/netgen`.

[35] C. Geuzaine and J.-F. Remacle, "Gmsh website." `http://www.geuz.org/gmsh/`.

[36] "Fluent: The GAMBIT CFD Preprocessor." `http://www.fluent.com/software/gambit/index.htm`.

[37] M. Donahue and D. Porter, "Object Oriented Micro-Magnetic Framework (OOMMF)." `www.nist.gov`.

[38] S. T. W.H. Press, B.P. Flannery and W. Vetterling, *Numerical recipes: the art of scientific computing.* Cambridge and New York: Cambridge University Press, 2nd ed., 1992.

[39] J. Cartwright and O. Piro, "The dynamics of Runge-Kutta methods," *Int. J. Bifurcation and Chaos*, vol. 2, pp. 427–449, 1992.

[40] M. Najafi, B. Krüger, S. Bohlens, G. Selke, B. Güde, M. Bolte, and D. P. F. Möller, "The micromagnetic modeling and simulation kit M^3S for the simulation of the dynamic response of ferromagnets to electric currents," *GCMS 08: Proceedings of the 2008 Conference on Grand Challenges in Modeling & Simulation*, p. 427, 2008.

[41] B. Krüger. Private communication, 2007.

[42] N. Massoud. Private communication, 2009.

[43] J. Jiang, H. Kaper, and G. Leaf, "Hysteresis in layered spring magnets," *Discrete Contin. Dyn. Syst.*, vol. Ser. B 1, p. 219, 2001.

[44] B. V. de Wiele, F. Olyslager, and L. Dupre, "Fast semianalytical time integration schemes for the Landau-Lifshitz equation," *IEEE Transactions on Magnetics*, vol. 43, no. 6, pp. 2917–2919, 2007.

[45] D. G. Porter and M. J. Donahue, "Precession axis modification to a semianalytical Landau-Lifshitz solution technique," *J. Appl. Phys.*, vol. 103, p. 07D920, 2008.

[46] D. G. Porter and M. J. Donahue, "Exploiting effective field time derivative information to improve accuracy of a norm-preserving Landau-Lifshitz solver," November 2008. Poster at MMM 2008 in Austin (Texas, USA).

[47] P. Brown, A. Collier, K. Grant, A. Hindmarsh, S. Lee, R. Serban, and C. Woodward, "Sundials (SUite of Nonlinear and DIfferential/ALgebraic equation Solvers home page, version 2.4." `https://computation.llnl.gov/casc/sundials/main.html`, 2009.

[48] A. Hindmarsh and R. Serban, "User documentation for CVODE v2.6.0." `https://computation.llnl.gov/casc/sundials/documentation/cv_guide.pdf`, 2009.

[49] D. Suess, V. Tsiantos, T. Schrefl, J. Fidler, W. Scholtz, H. Forster, R. Dittrich, and J. Miles, "Time resolved micromagnetics using a preconditioned time integration method," *J. Magn. Magn. Mater.*, vol. 248, p. 298, 2002.

[50] NIST, "Mumag standard problems," 1998. `http://www.ctcms.nist.gov/~rdm/mumag.org.html`.

[51] T. Fischbacher, M. Franchin, G. Bordignon, and H. Fangohr, "A systematic approach to multiphysics extensions of finite-element based micromagnetic simulations: nmag," *IEEE Transactions on Magnetics*, vol. 43, no. 6, pp. 2896–2898, 2007. online at `http://nmag.soton.ac.uk`.

[52] G. Bordignon, T. Fischbacher, M. Franchin, J. P. Zimmermann, A. Zhukov, P. de Groot, and H. Fangohr, "Analysis of magnetoresistance in arrays of connected nano-rings," *IEEE Transactions on Magnetics*, vol. 43, no. 6, pp. 2881–2883, 2007.

[53] G. Bordignon, T. Fischbacher, M. Franchin, J. P. Zimmermann, P. de Groot, and H. Fangohr, "Numerical studies of demagnetizing effects in triangular ring arrays," *J. Appl. Phys.*, vol. 103, p. 07D932, 2008.

[54] M. Franchin, J. P. Zimmermann, T. Fischbacher, G. Bordignon, P. de Groot, and H. Fangohr, "Micromagnetic modelling of the dynamics of exchange springs in multi-layer systems," *IEEE Transactions on Magnetics*, vol. 43, pp. 2887–2889, 2007.

[55] M. Franchin, G. Bordignon, T. Fischbacher, G. Meier, J. P. Zimmermann, P. de Groot, and H. Fangohr, "Spin-polarized currents in exchange spring systems," *J. Appl. Phys.*, vol. 103, p. 07A504, 2008.

[56] M. Franchin, T. Fischbacher, G. Bordignon, P. de Groot, and H. Fangohr, "Current driven dynamics of domain walls constrained in ferromagnetic nanopillars," *Phys. Rev. B*, vol. 78, p. 054447, 2008.

[57] F. Ott, T. Maurer, G. Chaboussant, Y. Soumare, J.-Y. Piquemal, and G. Viau, "Effects of the shape of elongated magnetic particles on the coercive field," *J. Appl. Phys.*, vol. 105, p. 013915, 2009.

[58] G. D. Chavez-O'Flynn, A. D. Kent, and D. L. Stein, "Micromagnetic study of magnetization reversal in ferromagnetic nanorings," *Phys. Rev. B*, vol. 79, p. 184421, 2009.

[59] W. Scholz, "Magpar: Parallel finite element micromagnetics package." `http://magnet.atp.tuwien.ac.at/scholz/magpar/`.

[60] M. R. Scheinfein, "LLG Micromagnetics Simulator." `http://llgmicro.home.mindspring.com/`.

[61] "Tcl scripting language." `http://www.tcl.tk/`.

[62] M. J. Donahue. Private communication at MMM 2008 in Austin (Texas), 2008.

[63] X. Leroy, D. Doligez, J. Garrigue, D. Rémy, and J. Vouillon, "Objective caml website," 2006. `http://caml.inria.fr`.

[64] "Mpich2." `http://www.mcs.anl.gov/research/projects/mpi/mpich2`.

[65] S. Balay, K. Buschelman, W. D. Gropp, D. Kaushik, M. Knepley, L. C. McInnes, B. F. Smith, and H. Zhang, "PETSc home page." `www.mcs.anl.gov/petsc`, 2001.

[66] G. van Rossum, "Python website," 2003. `http://www.python.org`.

[67] M. Najafi, B. Kruger, S. Bohlens, M. Franchin, H. Fangohr, A. Vanhaverbeke, R. Allenspach, M. Bolte, U. Merkt, D. Pfannkuche, D. P. D. Moller, and G. Meier, "Proposal for a standard problem for micromagnetic simulations including spin-transfer torque," *J. Appl. Phys.*, vol. 105, p. 113914, 2009.

[68] *Nmag — a micromagnetic simulation environment*, 2007. `http://nmag.soton.ac.uk/`.

[69] D. Suess, T. Schref, R. Dittrich, M. Kirschner, F. Dorfbauer, G. Hrkac, and J. Fidler, "Exchange spring recording media for areal densities up to $10\,\mathrm{Tbit/inch}^2$," *J. Magn. Magn. Mater.*, vol. 290-291, p. 551, 2005.

[70] R. Skomski and J. Coey, “Giant energy product in nanostructured two-phase magnets,” *Phys. Rev. B*, vol. 49, no. 5, p. 15812, 1993.

[71] S. Gordeev, J.-M. Beaujour, G. Bowden, B. Rainford, P. de Groot, R. C. C. Ward, M. R. Wells, and A. G. M. Jansen, “Giant magnetoresistance by exchange springs in $DyFe_2$-YFe_2 superlattices,” *Phys. Rev. Lett.*, vol. 87, no. 18, pp. 186808–1, 2001.

[72] M. Sawicki, G. J. Bowden, P. A. J. de Groot, B. D. Rainford, J.-M. L. Beaujour, R. C. C. Ward, and M. R. Wells, “Exchange springs in antiferromagnetically coupled $DyFe_2/YFe_2$ superlattices,” *Phys. Rev. B*, vol. 62, no. 9, pp. 5817–5820, 2000.

[73] E. Goto, N. Hayashi, T. Miyashita, and K. Nakagawa, “Magnetization and Switching Characteristics of Composite Thin Magnetic Films,” *J. Appl. Phys.*, vol. 36, no. 9, pp. 2951–2958, 1965.

[74] T. H. Fay, “The pendulum equation,” *Int. J. Math. Educ. Sci. Technol.*, vol. 33, pp. 505–519, 2002.

[75] “GSL — GNU scientific library.” `http://www.gnu.org/software/gsl/`.

[76] M. Grimsditch, R. Camley, E. E. Fullerton, S. Jiang, S. D. Baderand, and C. H. Sowers, “Exchange-spring systems: Coupling of hard and soft ferromagnets as measured by magnetization and Brillouin light scattering,” *J. Appl. Phys.*, vol. 85, pp. 5901–5904, 1999.

[77] M. J. Bentall, R. A. Cowley, W. J. L. Buyers, Z. Tun, W. Lohstroh, R. C. C. Ward, and M. R. Wells, “Magnetic structures of laves phase superlattices,” *Journal of Physics: Condensed Matter*, vol. 15, pp. 4301–4330, 2003.

[78] K. H. J. Buschow and R. P. van Stapele, “Magnetic properties of some cubic rare-earth-ion compounds of the type RFe_2 and $R_xY_{1-x}Fe_2$,” *J. Appl. Phys.*, vol. 41, no. 10, pp. 4066–4069, 1970.

[79] A. Mougin, C. Dufour, K. Dumesnil, and P. Mangin, “Strain-induced magnetic anisotropy in single-crystal rFe$_2$(110) thin films (r=Dy, Er, Tb, $Dy_{0.7}Tb_{0.3}$, Sm, Y),” *Phys. Rev. B*, vol. 62, no. 14, pp. 9517–9531, 2000.

[80] M. J. Bentall, R. C. C. Ward, E. J. Grier, and M. R. Wells, “Structure of $DyFe_2/YFe_2$ laves phase superlattices grown by molecular beam epitaxy,” *Journal of Physics: Condensed Matter*, vol. 15, pp. 6493–6512, 2003.

[81] J. P. Zimmermann, *Micromagnetic simulations of magnetic exchange spring systems.* PhD thesis, School of Engineering Sciences, University of Southampton, 2007.

[82] K. N. Martin, P. A. J. de Groot, B. D. Rainford, K. Wang, G. J. Bowden, J. P. Zimmermann, and H. Fangohr, "Magnetic anisotropy in the cubic Laves $REFe_2$ intermetallic compounds," *Journal of Physics: Condensed Matter*, vol. 18, pp. 459–478, 2006.

[83] C. Kittel, *Introduction to Solid State Physics.* John Wiley and Sons, Inc., 7th ed., 1996.

[84] V. M. Sokoliv and B. A. Tavger, "Nonuniform magnetization models in the theory of spin-wave resonance in a thin ferromagnetic film," *Radiophysics and Quantum Electronics*, vol. 9, no. 2, pp. 202–204, 1966.

[85] L. Thomas, M. Hayashi, X. J. R. Moriya, C. Rettner, and S. Parkin, "Resonant amplification of magnetic domain-wall motion by a train of current pulses," *Science*, vol. 315, pp. 1553–1556, 2007.

[86] A. Messiah, *Quantum mechanics, two volumes bound as one.* Dover Publications, Inc., Mineola, New York.

[87] M. Hayashi, L. Thomas, Y. B. Bazaliy, C. Rettner, R. Moriya, X. Jiang, and S. S. P. Parkin, "Influence of current on field-driven domain wall motion in permalloy nanowires from time resolved measurements of anisotropic magnetoresistance," *Phys. Rev. Lett.*, vol. 96, p. 197207, 2006.

[88] A. Yamaguchi, T. Ono, S. Nasu, K. Miyake, K. Mibu, and T. Shinjo, "Real-space observation of current-driven domain wall motion in submicron magnetic wires," *Phys. Rev. Lett.*, vol. 92, p. 077205, 2004.

[89] Z. Li and S. Zhang, "Domain-wall dynamics driven by adiabatic spin-transfer torques," *Phys. Rev. B*, vol. 70, p. 024417, 2004.

[90] G. Tatara and H. Kohno, "Theory of current-driven domain wall motion: spin transfer versus momentum transfer," *Phys. Rev. Lett.*, vol. 92, no. 8, p. 086601, 2004.

[91] P. Bruno, "Geometrically constrained magnetic wall," *Phys. Rev. Lett.*, vol. 83, no. 12, pp. 2425–2428, 1999.

[92] H. Fangohr, J. P. Zimmermann, R. P. Boardman, D. C. Gonzalez, and C. H. de Groot, "Numerical investigation of domain walls in constrained geometries," *J. Appl. Phys.*, vol. 103, p. 07D926, 2008.

[93] Y. Nakatani, A. Thiaville, and J. Miltat, "Faster magnetic walls in rough wires," *Nature Mater.*, vol. 2, p. 521, 2003.

[94] J. P. Nibarger, R. Lopusnik, and T. J. Silva, "Damping as a function of pulsed field amplitude and bias field in thin film permalloy," *Appl. Phys. Lett.*, vol. 82, no. 13, p. 2112, 2003.

[95] J. Zimmermann, G. Bordignon, R. Boardman, T. Fischbacher, and H. Fangohr, "Micromagnetic simulations of the magnetic exchange spring system $DyFe_2$-YFe_2," *J. App. Phys.*, vol. 99, p. 08B904, 2006.

[96] M. Grimsditch, G. Leaf, H. Kaper, D. Karpeev, and R. Camley, "Normal modes of spin excitations in magnetic nanoparticles," *Phys. Rev. B*, vol. 69, p. 174428, 2004.